Generalized Modelling of a Space Station and Determination of the Transfer Function

by

Natasha A. Neogi

Submitted to the Department of Aeronautics and Astronautics in
partial fulfillment of the requirements for the degree of

Master of Science

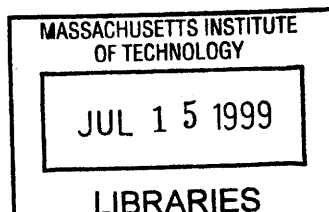at the

MASSACHUSETTS INSTITUTE OF TECHNOLOGY

May 18, 1999

[June 1999]

Author ......

Department of Aeronautics and Astronautics

May 18, 1999

Certified by ....

Dav J. Newman, Associate Professor
Department of Aeronautics and Astronautics
Thesis Supervisor

Accepted by ....

Jaime Peraire
Chairman
Department Graduate Committee

Generalized Modelling of a Space Station and Determination of the Transfer Function

by

Natasha A. Neogi

ABSTRACT

An elementary structural model of a modular space station, such as the Russian Space Station *Mir* or the International Space Station (ISS), was formulated using Euler-Bernoulli beam theory. Based on structural dynamic techniques and modal analysis, a generalized method for deriving a theoretical transfer function between astronaut force inputs and station acceleration outputs is postulated. The validity of this transfer function can then be examined using the experimental force and acceleration data collected from *Mir* from the period of 1996 to 1998.

In order to quantify astronaut-induced disturbances to the microgravity environment onboard a space station during long duration spaceflight, the Enhanced Dynamic Load Sensors (EDLS) Spaceflight experiment measured the forces and moments exerted by astronauts on the Russian Space Station *Mir*. Approximately 95% of all processed astronaut motions possessed a maximum force less that 275 N, a root mean square force less than 60 N and a power spectral density less than 22 Hz. Thus, astronaut motions are not the most stringent of design constraints upon a space station. Coupled with accelerometer data from the Space Acceleration Measurement System (SAMS), forces from crew motions can be temporally correlated with the overall acceleration of the Mir Space Station.

An operator similar to the Fourier transform is developed in order to convert the force and acceleration data from the time domain into the frequency domain. A least-squares approach is used in order to obtain the optimal transfer function between the force and acceleration experimental data. The maximum residue of this transfer function was found at the pole at 0.375 Hz with a magnitude of approximately 7.5×10^{-6}, which is in accord with transient time domain analysis performed previously. Unfortunately, due to a lack of collocation between the EDLS force plate sensors and the SAMS accelerometer heads, a meaningful comparison between the theoretical transfer function and the experimental transfer function could not be conducted.

Acknowledgements

Table of Contents

List of Tables

List of Figures

Nomenclature

Chapter 3

E: Young's Modulus for an Euler-Bernoulli beam

I: Moment of Inertia for Euler-Bernoulli beam

ρ: Density of Euler-Bernoulli beam

A: Cross-sectional area of Euler-Bernoulli beam

$p(x,t))$:   Forcing function

x: Linear variable along the length of the Euler-Bernoulli beam

t: Temporal variable

$v(x,t)$:   Generalized deflection of the elastic line of the beam for any x or t

$V_r(x)$:   Time independent part of the generalized deflection of the beam; the

               mode shape

λ_r: Eigenvalue of bean corresponding to the mode shape $V_r(x)$

$(A, B, C)_i$:   Aribitrary constants of integration in the solution of Euler-Bernoulli equa-

               tion

L: Length of the beam

ω_r: Natural frequency of of the beam corresponding to the mode shape $V_r(x)$

K_r: Non-Dimensionalized mode shape constant corresponding to the mode

               shape $V_r(x)$

A,B,C: Arbitrary amplitude of non-dimensionalized mode shape $V_r(x)$

θ: Phase angle of higher mode shapes $V_r(x)$, r>2

q_i: Discretized generalized displacement co-ordinates

[M]:   Discretized mass matrix

[C]:   Discretized damping matrix

[K]:   Discretized stiffness matrix

{Q}:   Generalized forces

{u}:   Signal/control input (force for EDLS experiment)

{w}:   Exogenous input (noise for EDLS experiment)

$\{\beta_u\}$:   Control input matrix in state space formulation

$\{\beta_w\}$:   Exogeneous input matrix in state space formulation

$[C_{xy}]$:   Output matrix in state space formulation

[D]:   Direct feedthrough term in the state space output formulation

m_r: Modal mass corresponding to r^{th} mode

y: Measurement of output state (displacement for EDLS experiment)

z: Performance of system

ϕ_r: Normalized mode of discrete steady state system

Φ: Normalized modal matrix $\Phi = [\phi_1 \phi_2 ... \phi_{2N}]$

ξ: Normalized modal coordinates

s: Laplace transform variable

Chapter 4

V_j: Vector magnitude

f: Frequency

Δt_i: Discrete time interval

Chapter 5

N: Integer value

ΔT :   Time period

T: Duration of data sample

t_i :   Discretized sampling time variable

u_n :   Discrete sampled input

$\hat{u}$:   Discrete fourier transform of a signal

ω :   Natural frequency of the system

b: Passband filter template

ω_0 :   Frequency at which the passband filter operates

p: Dummy variable of integration used to transform from the time to the frequency domain

λ :   Arbitrary parameter with which to tune passband filter $\hat{b}$

h_i :   Single input/single output linear operator transfer function between input u and output y

$\bar{h}$:   Estimate of transfer function h_i

Chapter 6

G_{yu} :   Transfer function between input u and output y

$T_{uy,r}$:   Residue at the rth pole ω_r for transfer function G_{yu} with no feedthrough term D_{yu}

z_r : r^{th} zero

p_r : r^{th} pole

g_{yu} :   Low frequency or DC gain of G_{yu}

$R_{yu,r}$:   Residue at r^{th} pole λ_r for transfer function G_{yu} with feedthrough term D_{yu}

l: Length of non-collocated beam in migrating zeroes example

Chapter 1

Introduction

1.1 Purpose

With the dawn heralded by the construction of the International Space Station, the main brunt of space research efforts will be faced with transitioning from a largely transient-presence Shuttle-based program to a more permanent-presence Station-based program. The International Space Station is being developed by NASA and international partners as a versatile user platform to allow long term on-orbit investigations of a variety of scientific and technology arenas. In particular, scientific studies are planned within a research class known as microgravity sciences in areas such as biotechnology, combustion, fluid physics and materials sciences. In order to maintain a microgravity environment during Space Station operations, it will be necessary to minimize reaction forces. These mechanical forces will typically occur during reboost, docking, equipment operation and Intravehicular Activities (IVA) such as active operations, robot operation, or passive operation [36]. Hence, an in-depth analysis of the effect of astronaut motion upon the microgravity environment of a space station becomes a crucial issue in the design and construction of any future space station.

1.2 Motivation

The International Space Station (ISS) should be completely assembled shortly after the turn of the century. The functions of the control system for the space station may be broadly divided into attitude control and vibration control. The design of a control system to perform these functions requires accurate dynamic models of the space station along with models for the disturbances and the definition of performance criteria. The presence

of a dense modal spectrum and the evolving nature of the system dynamics presents a challenge to accurately identify appropriate dynamic models. The dynamic behaviour of a full-size structure is greatly influenced by the ground environment and models based on ground tests may have to be validated in flight. Several levels of identification may be performed depending on the parameters to be identified and the amount of time and data available. For instance, separate tests will have to be executed in order to separate the rigid body mode identification from the low frequency mode identification [10].

Understanding vehicle disturbances caused by astronaut activity in a zero-g environment is essential for defining both the control system and the allowable astronaut motions during portions of the mission where pointing accuracies and stability are the governing requirements. Structural flexibility of the spacecraft can be excited by astronaut movements, and interaction with the control system can occur. All of these factors must be considered, and the control system bandwidth, dead zone, and control authority must be carefully selected to meet objectives of the mission and the design.

Many types of manned and unmanned space vehicles or satellites have been shown to be operationally feasible, however, many unsolved problems remain for the increasingly sophisticated and complex configurations of the future. Some concern remains about the nature and effect of disturbance torques external to the control system. The time profile and magnitude of these disturbances are important, particularly when the disturbances are cyclic. Given a torque caused by a forceful astronaut motion, the vehicle or station could possibly deflect, causing errors in acceleration and positioning.

The International Space Station (ISS)
Component View
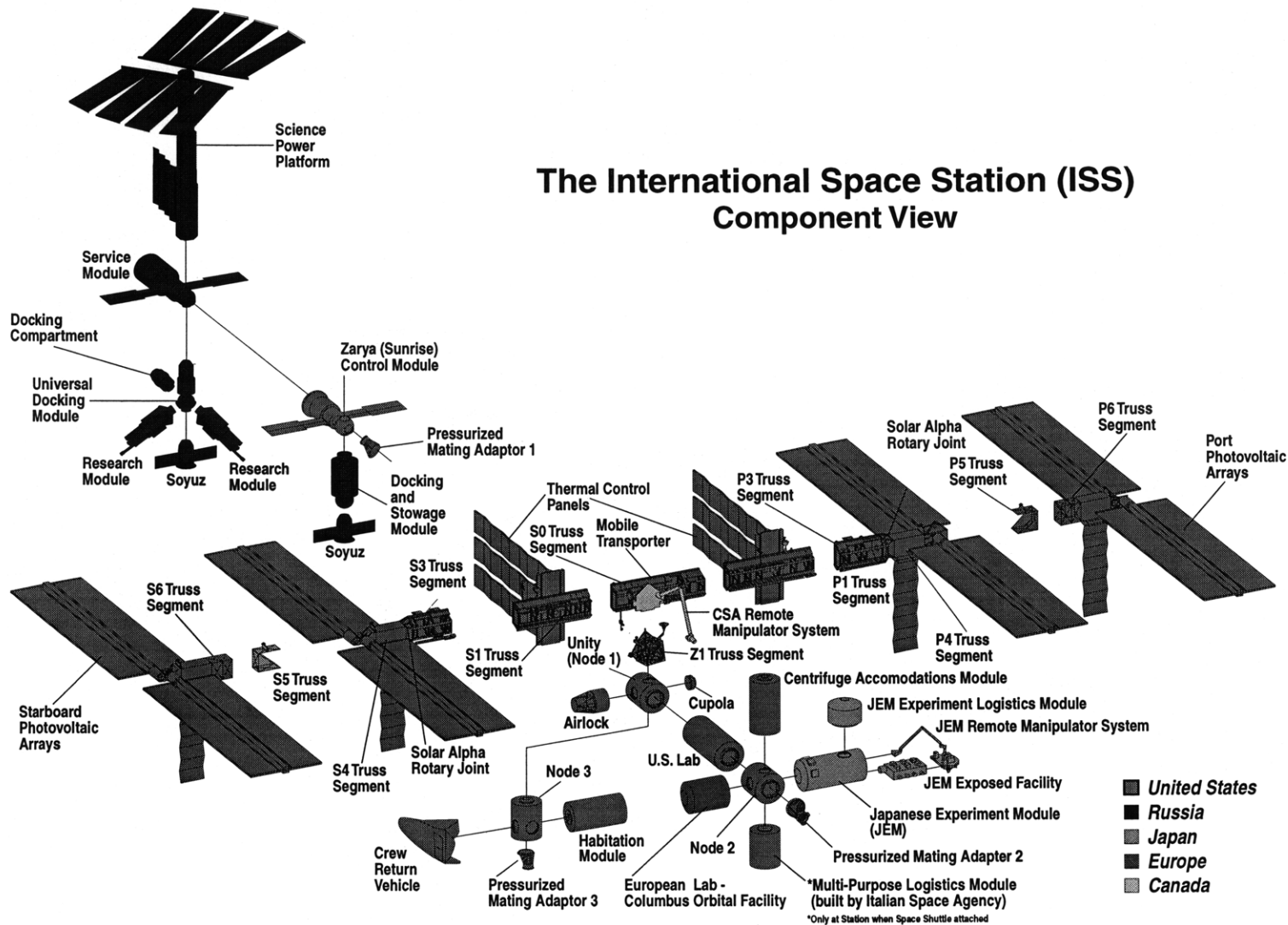
Figure 1.1: International Space Station [41]

13

Science Power Platform

Service Module

Docking Compartment

Universal Docking Module

Research Module

Soyuz

Research Module

Zarya (Sunrise) Control Module

Pressurized Mating Adaptor 1

Soyuz

Docking and Stowage Module

Thermal Control Panels

S0 Truss Segment

Mobile Transporter

P3 Truss Segment

Solar Alpha Rotary Joint

P5 Truss Segment

P6 Truss Segment

Port Photovoltaic Arrays

S3 Truss Segment

S6 Truss Segment

S1 Truss Segment

Unity (Node 1)

Z1 Truss Segment

CSA Remote Manipulator System

P1 Truss Segment

P4 Truss Segment

S5 Truss Segment

Airlock

Cupola

Centrifuge Accomodations Module

JEM Experiment Logistics Module

JEM Remote Manipulator System

Starboard Photovoltaic Arrays

S4 Truss Segment

Solar Alpha Rotary Joint

Node 3

U.S. Lab

Node 2

JEM Exposed Facility

Japanese Experiment Module (JEM)

Pressurized Mating Adapter 2

Crew Return Vehicle

Pressurized Mating Adaptor 3

Habitation Module

European Lab - Columbus Orbital Facility

*Multi-Purpose Logistics Module (built by Italian Space Agency)

*Only at Station when Space Shuttle attached

United States
Russia
Japan
Europe
Canada

Of the many induced torques (solar pressure, magnetic effects, gravity gradient, momentum of onboard equipment, vehicle center-of-gravity shift etc.) that a vehicle may encounter in low earth orbit, the torque caused by astronaut motion is the subject of this dissertation. This torque includes disturbances caused when an astronaut performs maintenance or other activities external to a remotely operated vehicle as well as the obvious disturbances caused by an astronaut residing onboard the vehicle.

Astronaut motion disturbances are divided into two general categories: restrained astronaut activities and translational (or unrestrained) activities. The first is defined as those actions in which the astronaut is prevented from a gross translational movement of the body's center of mass by restraining devices (i.e., handhold or foot restraints). Translational activities are those that do allow the astronaut's center of mass to move about freely in space.

Before one actually designs a space station or other vehicle, one must first determine whether or not astronaut motion is truly a valid design constraint. The particular mission requirements usually decide the issue because the vehicle's pointing accuracy considered in terms of the type or range of astronaut actions involved may well dictate the predominant frequency content of the disturbances. Until the recent experiments performed aboard the Space Shuttle and the Russian Space Station Mir, astronaut motions were generally thought to represent a large disturbance force and torque for any spacecraft, and their frequency content was thought to be much higher than those of such disturbances as gravity gradient or aerodynamics moments [13]. However, further study indicated that forceful astronaut motions may not be frequent occurrences.

1.3 Objectives

The dynamic behavior of a large space structure under the effect of astronaut loads poses a

problem of both interest and complexity. In order to characterize the dynamic behavior of a flexible, multipart space structure under the effect of transient astronaut loads, the prescribed procedure is followed. Firstly, a measurement of "average" or "typical" astronaut forces takes place on board a space station. The Enhanced Dynamic Load Sensors (EDLS) spaceflight experiment was conducted on the Russian Space Station *Mir* from May 1996 to May 1997, with the sensors and data being returned from space in 1998. The EDLS experiment measured astronaut forces for particular and general actions[1]. The force and moment data gathered from the experiment must then be identified with specific actions, thus establishing an estimate of the time the action took place. These specified actions, for which force and moment data exist, must then be correlated with the acceleration of the station. Acceleration data for the Mir station can be obtained from the Space Acceleration Measurement Systems (SAMS) Experiment. Once the acceleration data is matched to its corresponding force data, a transfer function between these two quantities can be found. This transfer function between astronaut motion forces and station acceleration is the ultimate objective of the text, and can be said to be an accurate characterization of the dynamic behavior of a space station under astronaut motion.

Hence, the objectives of this thesis can be summarized as being:

1. To perform a statistical analysis upon the force data acquired from the EDLS experiment.
2. To isolate specific astronaut motions and their time of occurrence precisely.
3. To correlate specified astronaut motions with acceleration data taken from the SAMS experiment.
4. To use the correlated force-acceleration data to derive a force-acceleration transfer function for the Russian Space Station Mir
5. To compare the experimental form of the transfer function to a theoretically derived transfer function.

---

1. NASA provided funding for EDLS as a risk mitigation experiment for the International Space Station (ISS).

1.4 Scope

The following dissertation addresses all of the steps outlined in the procedure necessary to obtain the final objective of elucidating a transfer function between the astronaut motion forces and the acceleration on a space station. This will hopefully allow for the quantification and prediction of the effect of astronaut motions upon the microgravity environment of a generalized space station. A transfer function is the perfect vehicle for codifying the relationship between two state variables for a system, usually an input and an output. It quantifies the effect of a change in an input to the altered output state of the system. The method by which a transfer function is derived can be divided into two methods: an experimental approach and a theoretical approach.

The theoretical aspect of the thesis embraces the concept of modelling. A model of a single module (i.e. Priroda) of a space station (i.e. Mir) is presented, and a simplistic overview of its dynamic behavior under simple astronaut forces is outlined. A more complex model of a generalized space station is then presented, and observations are made dealing with its structural dynamics under a forced loading condition, which can be made to approximate internal astronaut motions. A method for theoretically determining transfer functions, namely the state space approach, will then be explored.

The experimental approach will involve a discussion of the methods to process and analyze the space flight data from the EDLS experiment. A procedure will be outlined by which the SAMS data is interpreted, and a time source is assigned. It will also embrace a discourse on the correlation between the EDLS data and the SAMS data, and the perils inherent therein. Precise motions from the EDLS data will be correlated with the corresponding acceleration data from the SAMS experiment. Hence, the input and output signals for the Russian Space Station Mir force-acceleration transfer function will have been established, with the goal being the prediction of the acceleration of the station due to an

astronaut's motion within the aforesaid station. The results will then be discussed in the context of a microgravity environment, and an attempt will be made to explain the behaviour of the transfer function.

1.5 Outline

This first chapter serves as an introduction to the inherent problem of space station accelerations and the effects of astronaut motions thereupon, providing the motivation for the research carried out. The second chapter provides a literature review on the topics of space stations and their microgravity environments, relevant space flight experiments that measure astronaut force motions, and the modelling of large space structures. The next chapter outlines the concepts of structural modelling, and provides insight into the approach of theoretically modelling transfer functions. Following that, the space flight data from the EDLS experiment is analyzed in the fourth chapter, and a method for correlating motions from the EDLS experiment to accelerations from the SAMS experiment is advanced. The fifth chapter describes the techniques necessary to experimentally determine a transfer function given the force data from the EDLS experiment, and the acceleration data from the SAMS experiment. Finally, a chapter containing a discussion of the transfer function ensues, where theories are posited in order to reconcile the predicted response with the actual behaviour of the structure. The corpus of the text is then completed by a chapter of conclusions and future recommendations.

Chapter 2

Space Stations and the Microgravity Environment

Before addressing the issue of astronaut motions causing disturbances to microgravity environments, a description of the possible astronaut environments is necessary. If the astronaut environment can be described as the structural environment which contains the astronaut, the smallest autonomous self-contained astronaut environment in space can be considered to be the astronaut's space suit. As well, a common environment the astronaut inhabits in space is the Space Shuttle. However, the scope of this thesis deals predominantly with long-term large space structures, therefore the Russian Space Station Mir and the International Space Station are primarily addressed. As well, a definition for a microgravity environment is explored, along with the concept of astronaut disturbances. A brief foray into the previous experiments that dealt with the quantification of astronaut motion is conducted. Finally, an overview of the work to date on the structural modelling of large space structures is presented.

2.1 Background on Mir

Space flight has been present for more than 30 years. Beginning with only brief trips into the upper atmosphere, flights have progressed to astronauts circling the Earth for two weeks and cosmonauts spending over a year in orbit. The Russians have advanced their space program incrementally, continuously modifying previous designs for space stations to create new and improved models, whereby they are able at this point to maintain a long-duration human presence in space. A series of vehicles have been designed and flown, leading up to the current Russian space station, the Mir Complex (Fig. 2.1). Technically,

the Mir base block is only one module of the entire station, which is made up of the Mir and several other modules. Therefore, in this section, Mir is used to describe the 'base block' of the entire complex structure, while in all other sections, it is used to refer to the entire station.

Although the string of Soviet space stations began with the first Salyut station, launched in 1971, the Mir Space Station follows most directly from the Salyut-6 and -7 stations, direct precursors to the current Russian space station. In retrospect, the Soviets called the first five Salyuts the 'first generation' Salyuts, with the 'second generation' including the last two Salyut stations, 6 and 7. Salyut-6 was launched in September of 1977, destined to be a great advancement in Soviet space presence. Utilized from 1977 to 1981, Salyut -6 was outfitted with several large pieces of experimental equipment installed prior to launch. The station was also host to a greater number of experiments brought onboard by a number of Progress and Soyuz vehicles. While the Progress vehicles were automated supply missions, the Soyuz vehicles primarily acted as transfer vehicles, and carried cosmonauts to and from the orbiting Salyut-6. Capabilities of the station allowed new world records to be set for longest stay in space, 6 months, at that time. Launched in April 1982, Salyut-7 offered no great technical advances over Salyut-6. It was never planned to be a permanently occupied station, but the Soviets managed to maintain an eight month uninterrupted presence. Continuous cosmonaut operations onboard Salyut-7 ceased in 1986, and the emphasis of the Soviet space program turned to building the Mir Space Station [43].

The Mir Space Station is generally described as being a "third generation" space station in the Soviet space program, following the two generations of Salyut stations. It is modular in design, allowing several different vehicles to be 'docked' together. As well, it was intended to be a permanent habitat, which can be regarded as a huge first step towards

establishing an ongoing presence in space. The Mir module was launched February 1986, thus making it approximately 13 years of age in 1999. The primary Mir module was launched in an uninhabited state. Its design was largely based on the modules of the second generation Salyut stations, and acts as the core module or 'base block' for the entire Mir Space Station (See Fig 2.1).
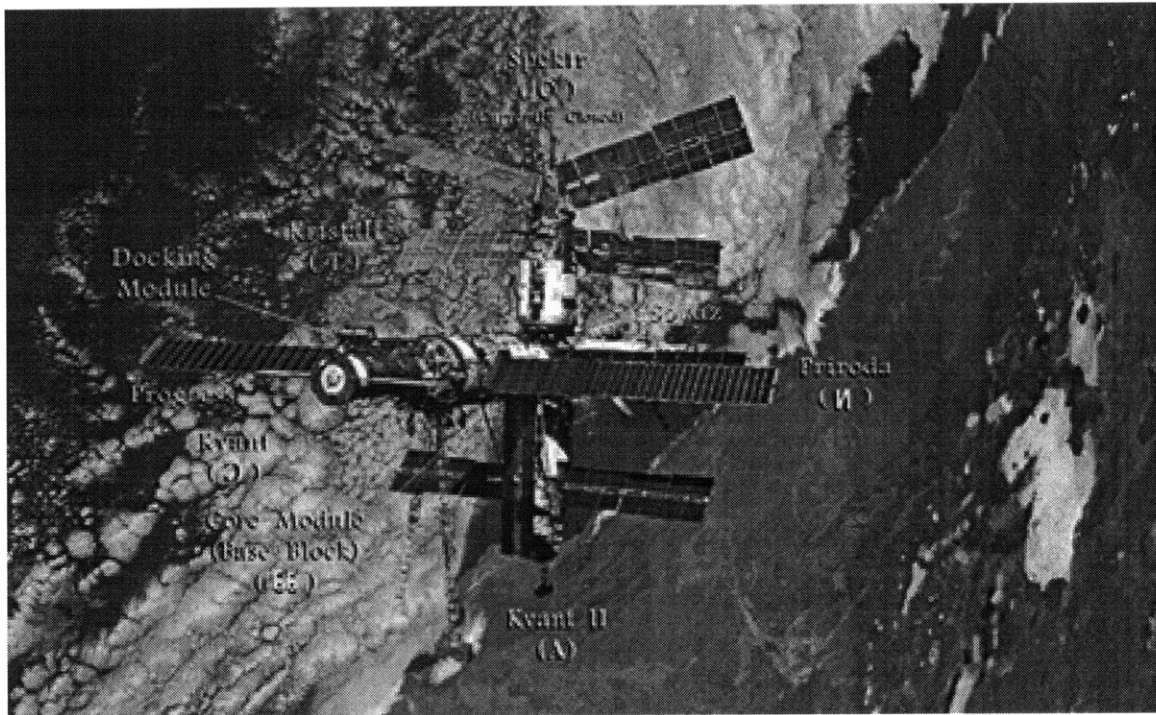
Figure 2.1: Russian Space Station Mir [55]

On March 13 1986, the first mission to Mir was launched with a Soyuz module containing two veteran Salyut cosmonauts. The mission of the astronaut was to dock with and activate the Mir Module. They began by running diagnostic tests of the station, starting experiments and preparing for the arrival of the next module. Launched on March 31, 1987, the Kvant-1 carried a series of international astrophysics experiments. Though the Soviets initially had difficulty docking Kvant-1 with Mir, hard dock was achieved on April 12, 1987. Kvant-2 was the first in a series of specialized modules to be added to Mir, and it dealt with logistical functions (i.e., solar arrays). Launched on November 26, 1989

Kvant-2 was docked to the forward axial port on December 6, then moved to a radial port on December 8 (Fig. 2.2). Kvant-2 possessed an airlock that made Extravehicular Activity (EVA) missions easier to perform. The next module, Kristall, left the ground on June 1, 1990, and restored the symmetry of the station when it was finally attached to Mir.
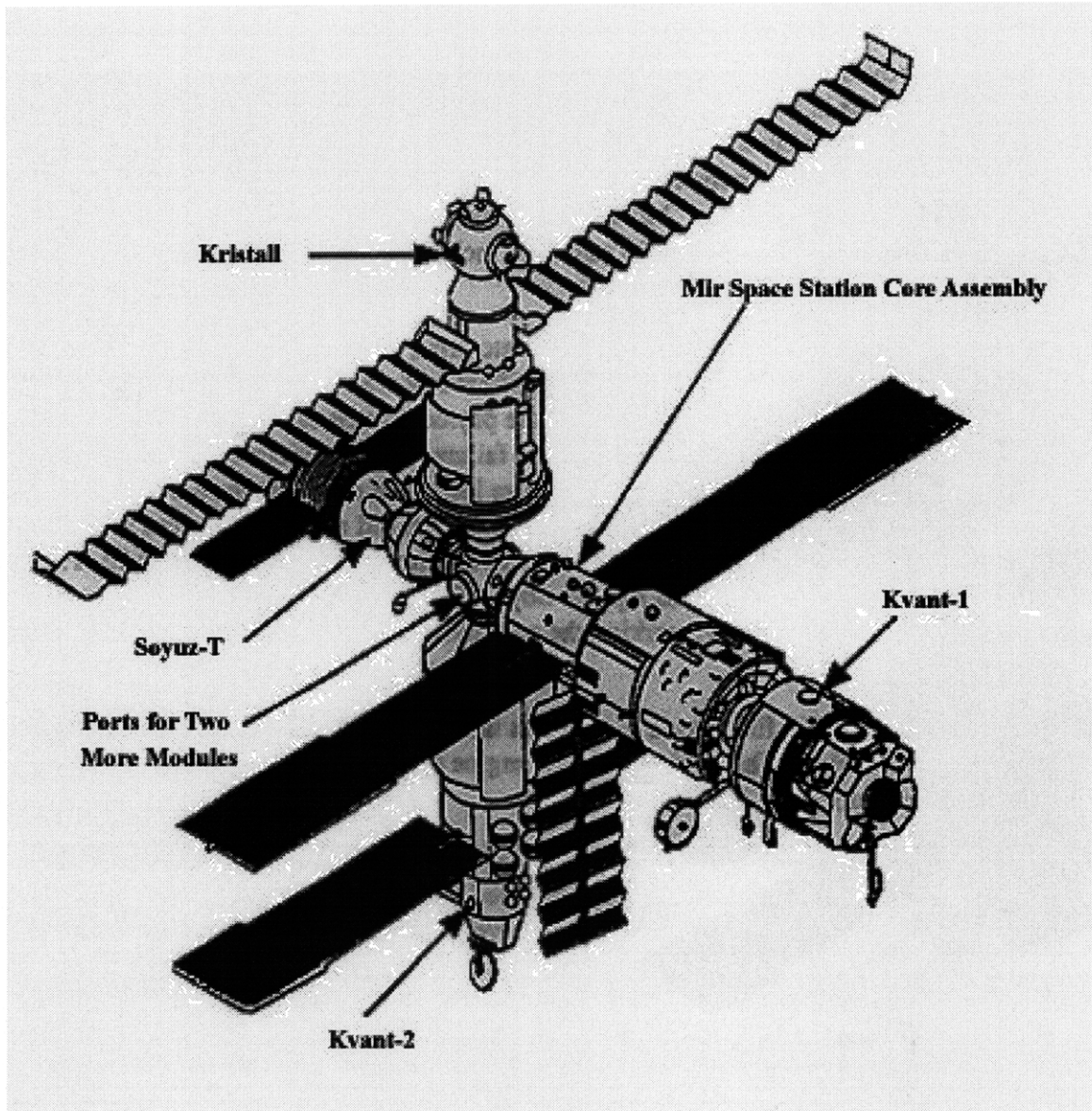
Figure 2.2: Russian Space Station Mir with Kristall Module Attached [43]

In the same set of maneuvers as Kvant-2, Kristall was docked first to the axial port, then to the radial port opposite Kvant-2 on June 11, 1990 (Fig. 2.2). Similarly, the ill-fated

Spektr module, used for geophysical sciences, was launched in May 1995, and a docking

module, used to establish shuttle-Mir docking capabilities was launched shortly thereafter

in November 1995.
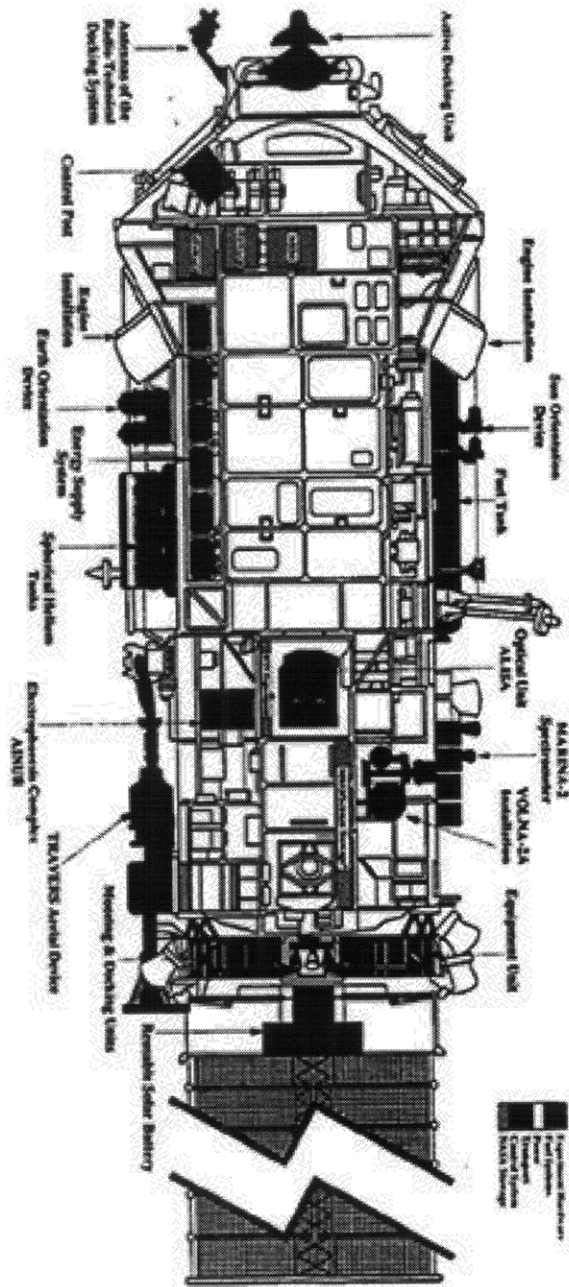
Figure 2.3: Priroda Module [39]

Finally, the last module to be added to the Mir Space Station was the Priroda module

(see Fig 2.3). Priroda, was launched on April 23, 1996 and docked with the Mir Complex

on April 26, 1996. Its primary purpose was to add an Earth remote sensing capability to

Mir. It also carried 1,000 kg of hardware and supplies for several spaceflight experiments, including the Enhanced Dynamic Load Sensor Experiment. The specifications for Priroda are:

Table 2.1: Priroda Module Properties [39]

Length (m)	Mass (kg)	Max. Diameter (m)	Volume (m³)
13	19 700	4.35	66

The Soyuz crafts can most equitably be referred to as a 'taxi to the stars'. The Soyuz vehicles have ferried countless cosmonauts back and forth to various low earth orbit destinations for many years and are primarily for transporting humans to and from space. Evolution of the Soyuz craft has somewhat paralled that of the Soviet space stations, with a solid design being improved upon throughout time. Originally designed for the purpose of going to the moon (after docking with a booster in Earth orbit), the Soyuz was modified to fly cosmonauts to space stations. A fatal accident occurred on Soyuz-11 when cabin pressure was lost and three unsuited astronauts perished. The original Soyuz was designed for only two "suited" cosmonauts, a fact that was remedied with the launch of the 'Soyuz T' in December 1979, which could carry three suited cosmonauts. A final version was introduced, Soyuz TM1, and launched on May 21, 1986. This craft had a new docking system, and when Mir was launched a few months later, it was able to transport cosmonauts to and from the station [43].

The Progress vehicles transport supplies to and from the astronaut environment. On January 20, 1978 the first Progress supply ship was launched in support of Salyut-6.

Progress-1 was the first in a long line of automatic transport vessels that are still supporting the Mir station. A new Progress visits the Mir space station about every month to resupply oxygen and nitrogen, propulsion fuel, food, water, clothing and equipment. The vehicle is then filled with trash, used equipment, and other expendables and burns up upon re-entry to the Earth's atmosphere. In June of 1997, a Progress re-supply vehicle collided with Mir's Spektr module, rendering the module completely unusable [2].
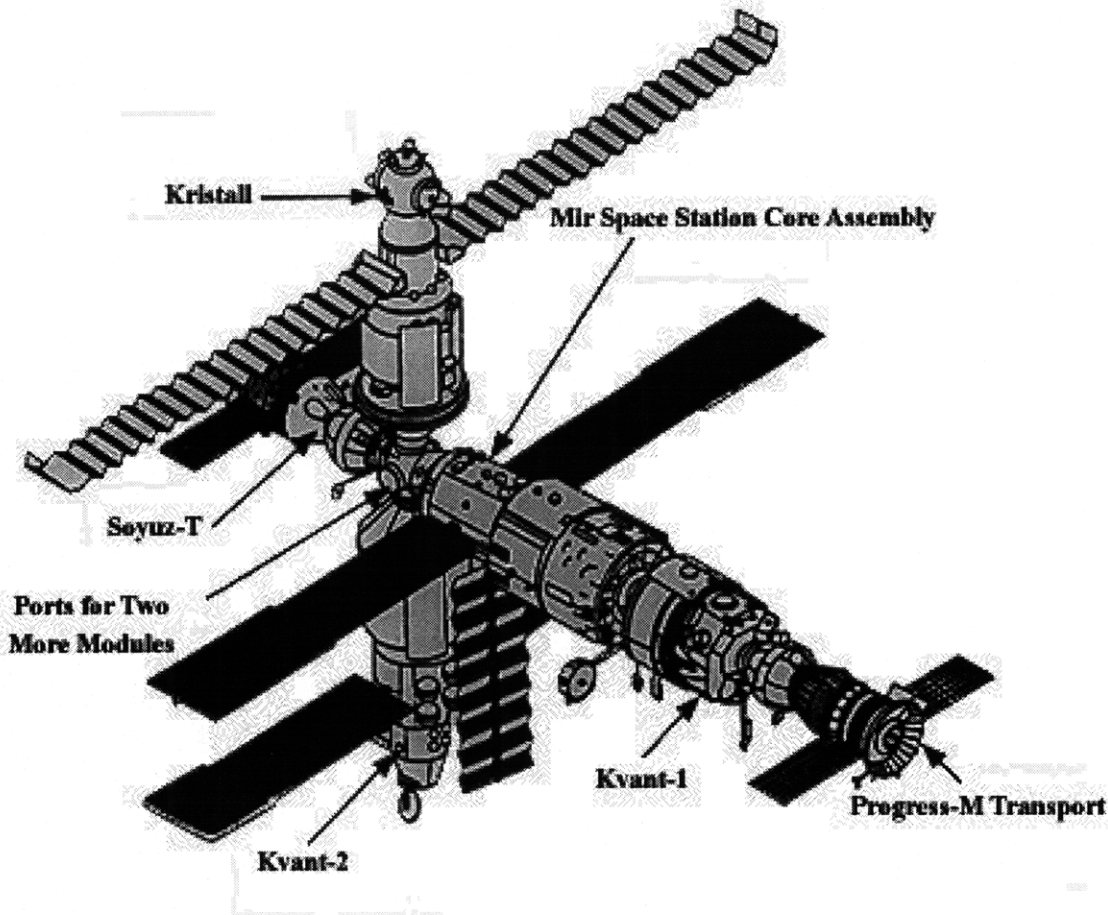
Figure 2.4: Russian Space Station Mir with Progress Module Docked [43]

2.2 International Space Station

America has not exhibited as aggressive a program to establish a permanent presence in space as the Soviets. The first American space station was Skylab, which was, in reality the third stage of a booster of a Saturn V rocket whose fuel storage tanks had been con-

verted into cabins. It was launched into orbit May 14, 1973 and weighed 75 tons, with a main diameter of 6.6 m and a length of 14.7 m. Skylab hosted three crews, each with three astronauts for a total of 171 days. Skylab eventually re-entered the atmosphere on July 11, 1979 and touched down in the Pacific [42].

The Space Transportation System (STS) is the official name for the Space Shuttle program. The Space Shuttle Columbia was launched on April 12, 1981. The space shuttles act as a transportation system, launching satellites and other payloads, as well as performing short duration microgravity experiments [2].

The inception of the concept of a pseudo-permanent space station can be dated to the Presidency of Ronald Regan. In 1988, the project of building an international space station, called "Freedom", had been proposed by the National Aeronautics and Space Administration (NASA) and accepted by the Canadians (Canadian Space Association), Europeans (European Space Association) and Japanese (Japanese Aeronautics and Space Administration), who had all become partners in this joint venture. Due to budgetary constraints and a lack of accomplishment in fabricating hardware[1] over the past years, the ambitious plans for the space station were scaled down in 1993 by the Clinton administration, and it was renamed International Space Station Alpha. Later again, it was reassessed, and this time it became officially the International Space Station (ISS).

For further details about the assembly of the International Space Station, see Appendix A.

2.3 Microgravity Environment

A primary mission of the International Space Station (ISS) is to provide an extremely low acceleration environment to enable a broad class of scientific research that exploits micro-

---

1. The space station was only a paper design during the Entire Bush Administration

gravity conditions. Many experiments performed in space laboratories seek to avoid unwanted effects of gravitational acceleration experienced under Earth[2] gravity conditions.

The microgravity environment of an orbiting body can be described in terms of accelerations grouped into three main categories: quasi-steady, oscillatory, and transient [25]. Quasi-steady accelerations are characterized by a frequency less than 0.01 Hz, for the ISS. This definition uncouples the quasi-steady state environment from the oscillatory environment as the specified frequency level is generally an order of magnitude less than the first structural mode, which is approximately 0.1 Hz for the ISS [6]. The orbiting body is considered to be a rigid body at such low frequencies, and the quasi-steady state microgravity environment is based on rigid-body dynamics and is primarily dependent on the structural configuration of the space station. The quasi-steady acceleration environment of the orbiting station contains four primary sources: orbiter aerodynamic accelerations, gravity gradient accelerations, spacecraft rotational accelerations and random events[3]. They are a function of the distance away from the station center of gravity, station altitude, station attitude and atmospheric conditions of space. However, for the ISS, accelerations induced by vehicle control rate error, and potentially from vent and appendage slew events, also fall with the quasi-steady definition bounds [17].

Oscillatory accelerations are then defined as those accelerations with frequency content above the quasi-steady criteria and below approximately 300 Hz [31]. These accelerations are also those with a characteristic frequency or multiple frequencies and may contain harmonic frequencies. These frequencies may also be variable with time. The ISS laboratory environment in the 0.01-300 Hz frequency range is produced by many simulta-

---

2. Earth gravity or terrestrial gravity is taken as being 1g in nature.
3. Waste dumping or random astronaut motions are examples of random events

neous disturbance sources with varying duty cycles. At any one time, a combination of sinusoidal, transient and random disturbances are present.

Accelerations in the oscillatory frequency range are caused by the on-orbit operations of equipment and astronauts aboard the Space Station during quiescent periods. Mechanical disturbances (i.e., pumps, valves, fans and vents) affect the quality of the microgravity environment. As well, rotating equipment and motor imbalance from solar array and thermal radiator rotations, along with antenna slewing will also affect microgravity performance. Finally, of the utmost interest is the random acceleration occasioned by astronaut activity. Astronaut motions from Intravehicular Activity (IVA), such as pushoffs and landings, may act to degrade the microgravity environment [46].

Transient accelerations are usually short in time duration and are characterized as single events, such as pulses or step changes. Many transient acceleration events cause excitation of structural frequencies, which last far longer than the transient event itself. Accelerations in these three categories: quasi-steady, oscillatory and transient, combine into a complex acceleration environment to which the inhabitants of the space station are exposed [26].
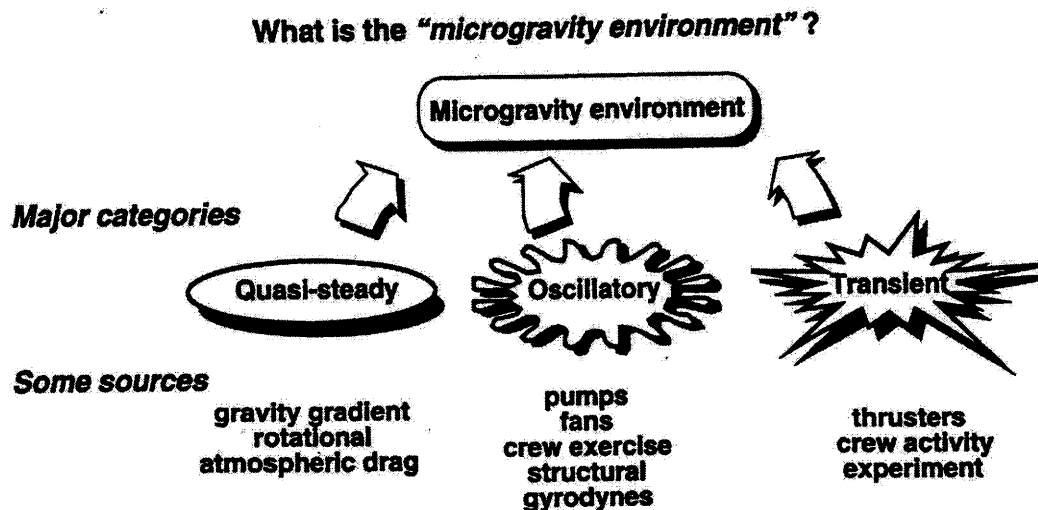
Figure 2.5: Acceleration Categories Summary[26]

Since a primary mission of the ISS is to provide an extremely low acceleration environment, it has been designed to a set of "microgravity requirements". The ISS microgravity requirements stipulate the duration, location and allowable acceleration levels that are associated with the ISS microgravity mode. With regard to duration, the requirement is for the specified acceleration levels to be sustained for at least 180 days per year. These acceleration levels are to be achieved at 50% of the International Standard Payload Rack (ISPR) locations. There are 12 ISPRs in the US Laboratory, 10 ISPRs in the European Attached Pressurized Module (APM) and 10 ISPRs in the Japanese Experiment Module (JEM). The acceleration levels themselves are addressed separately for quasi-steady, structural and vibroacoustic cases [32].
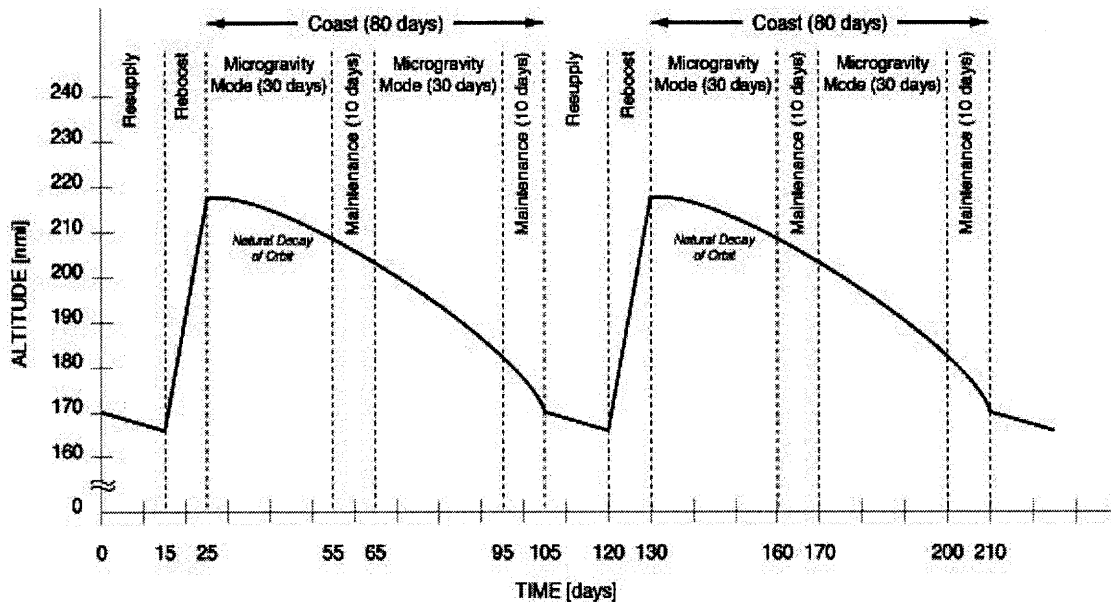
Figure 2.6: Microgravity Cycle for ISS [7]

The performance assessment of the International Space Station microgravity environment encompasses three distinct analytical methods: quasi-steady, structural dynamic and vibroacoustic, and an operational oversight to insure that the quiescent period duration criteria is met. The quasi-steady-state analysis predicts the acceleration environment below

28

0.01 Hz using rigid body flight mechanics simulation techniques. The structural dynamic analysis covers the 0.01 to 50 Hz regime and is characterized by finite element methods and mechanical disturbances. The vibroacoustic analysis accounts for both mechanical and acoustic disturbances via statistical energy analysis techniques between 50 and 300 Hz.

The quasi-steady acceleration requirements are specified in the time domain and limit the instantaneous peak magnitude to 1 microgravity. In addition, the perpendicular component to the orbital average quasi-steady vector must be equal to or less than 0.2 microgravity. This latter criteria implicitly places a "stability" requirement on the structure's quasi-steady performance [7].

In the oscillatory regime, there are two primary requirements. First, the station's induced acceleration environment due to all disturbance sources in any 100 second microgravity mode interval is limited to the one-third octave band root-mean-square acceleration level. This frequency domain "combined" requirement is supplemented by a second requirement in the time domain. The second requirement applies to individual transient sources to offset the effects of the 100 second averaging associated with the combined requirement criteria. Individual transient disturbances are limited to 1000 microgravity at any instant, and 10 microgravity seconds in an 10 second interval on a per axis basis [2].

When in microgravity mode, the ISS inhibits its capabilities to execute translation maneuvers, control attitude propulsively and support EVA and external robotic operations. Microgravity duration, location and quasi-steady acceleration requirements impact flight altitude, vehicle attitude and logistic resupply planning. The vibratory acceleration requirements are equally encompassing. They are responsible for the exclusion of a number of ISS capabilities in microgravity mode and drive Internal Vehicular Activities (IVAs) from maintenance to astronaut operation. To meet the vibratory microgravity criteria, the

ISS employs an Active Rack Isolation System (ARIS) at the microgravity ISPR locations. ARIS isolates the necessary sites, thereby reducing the need to calculate the effect of each and every accelerating mass interacting with the station, and can even act to mitigate the effects of astronaut locomotion to ISPR sites [32].

2.4 Astronaut Motion Disturbance Quantification

Vibrations and transient disturbances from astronaut intravehicular activity (IVA) could corrupt the microgravity environment on board the International Space Station. The magnitude and frequency of disturbances to the microgravity environment observed on the Space Shuttle flights and predicted for the ISS are critical factors in determining mission success. A stable, very low-gravity environment is necessary to assure that material science, earth science, astronomical and life science investigations aboard the International Space Station yield the most accurate data. For the ISS, primary concerns for background acceleration arise from several agents: random astronaut motions, thruster activity and acceleration due to drag and gravity gradient [32]. Materials science experiments specify a minimal disturbance environment, especially in the low frequency range of less than 0.1 Hz [44]. This section is primarily concerned with astronaut motions, and their effects on the microgravity environment.

There are myriads of astronaut activities that induce accelerations and potentially add to the degradation of the ISS microgravity environment. The reasons that they need to be quantified are two-fold [2]:

1. To predict their contribution to the total ISS acceleration environment for payload planning purposes.
2. To assure that the ISS/ARIS sway space is not violated, that is, the microgravity environment in the locations isolated by the ARIS apparati are not affected by astronaut activities.

In order to quantify astronaut induced accelerations, the forces and moments imposed on

the vehicle by the astronaut during their activities are needed. Acceleration measurements are insufficient in and of themselves to function as predictors.

Skylab data [13] exists for translatory and selected body movements, but they are severely limited in scope. The primary focus of these experiments was:

> "expected to lead to an improved criteria for consideration of
> astronaut motion disturbances in manned spacecraft attitude and
> experiment pointing control system design."

The astronaut induced disturbance experiments were performed on mission day 20 of the Skylab-3 mission. It was assumed that the astronaut had become well adapted to the environment. Prescribed body motions were conducted, primarily to reproduce types of activities performed in earlier ground simulators, such as simple arm and leg movements. Simulated console operations were conducted as well, in an exercise that lasted approximately 3 minutes. In almost all cases, the power spectral density peaks for the motions were in the range of 1-2 rad/s. The amplitudes differed greatly, with maximum forces of 400 N and applied torques of 1000 Nm being generated from pushoffs and crouching activities [58].

The Dynamic Load Sensors (DLS) experiment was performed on the STS-62 mission at the behest of the Space Station Freedom manager to address concerns pertaining to the appropriateness of basing the space station structural requirements on the Skylab data. Three multi-degree-of-freedom sensors (a touchpad, a handhold and a foot restraint) were used to measure nominal astronaut loads during the mission. The sensors measured loads at the following heavily travelled areas in order to maximize data collection in the space shuttle middeck: middeck lockers, galley floor and middeck augmentation rack.

DLS RMS Force Motion Histogram

(a)

Frequency below which 95% of the Power is Contained
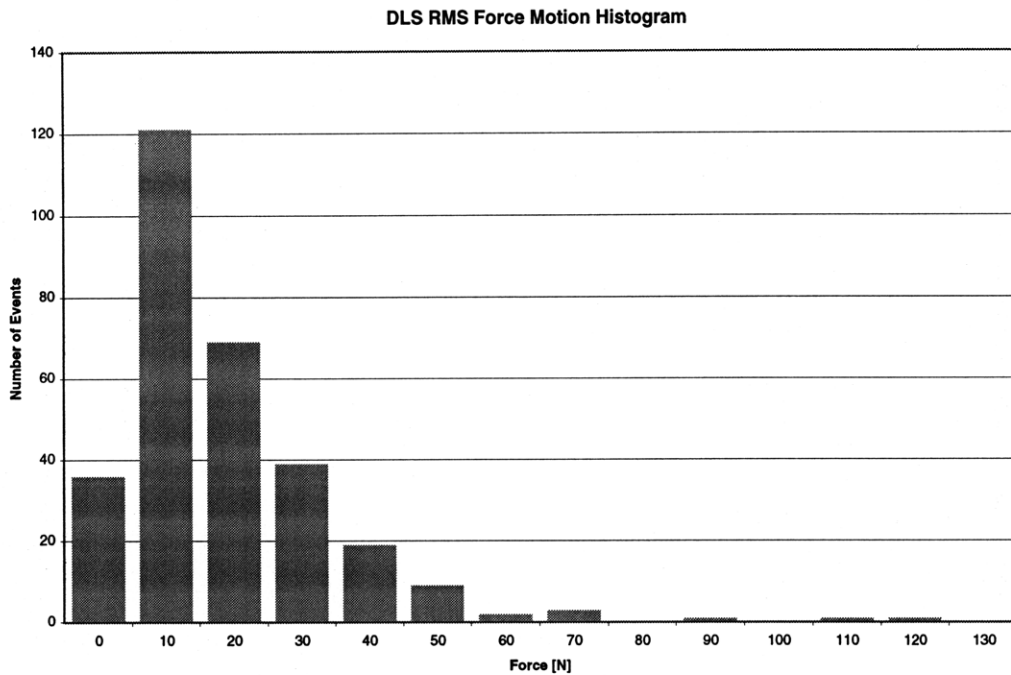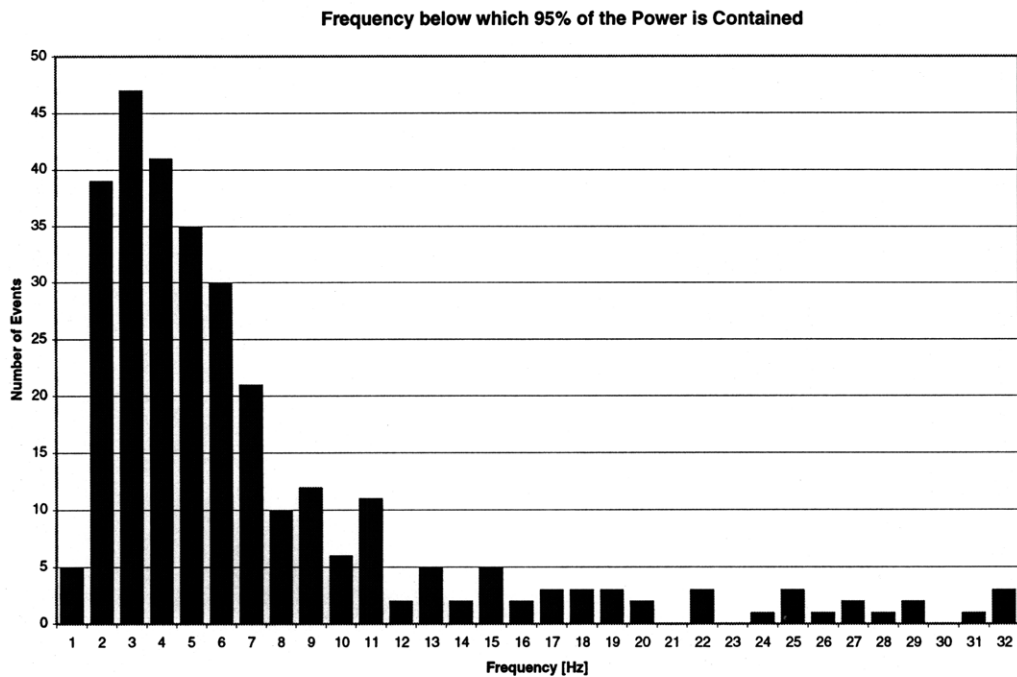
(b)

Figure 2.7: (a) Root-Mean-Square (b) Power Spectral Density Graphs for DLS [2]
DLS data was taken on days 7, 8 and 11 of the 14 day mission. Astronaut-induced disturbances were measured for landings, pushoffs, handhold and foot restraint activities.

Graphs of the root-mean-square (RMS) force and of the power spectral density (PSD) for all the events are presented in Figure 2.7. The data from the power spectral density shows a predominance of frequencies below 6 Hz. An average RMS value of 24 N was noted for all motions, and a maximum force of 466 N was recorded by the foot restraint. However, this maximum force event was anomalous in nature, and occurred because the astronaut in question purposefully attempted to exert the maximum force possible, at the behest of the principal investigators. Detailed frequency analysis showed that events with energy content above 10 Hz were mainly recorded by the foot restraint, which was the most frequently used device [59].

To further study the effects of astronaut motion upon the microgravity environment, the Enhanced Dynamic Load Sensors system was placed aboard the Priroda module of the Russian Space Station Mir. EDLS became operational and recorded data during the NASA-2 and NASA-4 missions, as is fully detailed in Chapter 4. Any differences in the data taken from the DLS sensors and the EDLS sensors, such as the magnitude of force exerted by the astronaut during the execution of a motion, may be due in part to the fact that the astronauts had a far greater timespan in which to adapt their control strategies for performing simple locomotive tasks.

Thus, after three space flight missions to quantify astronaut motion, the positive results would appear to be that the forces and torques measured by the DLS and EDLS NASA-4 experiments are of approximately the same order of magnitude, and they are about an order of magnitude less than that of the Skylab data. However, it is ambiguous whether this data is representative of astronaut motions on a vehicle the size of the ISS. Hence, a theoretical model of the effects of forces on a large space structure should be attempted, in order to gain some insight as to the level of disturbances astronaut motions will cause aboard the ISS.

2.5 Structural Modelling of Space Stations

2.5.1 Analytical Modelling

The space structures of the future will be complex tree-like structures with open and closed loops, rigid and flexible bodies, and will undergo maneuvers where their topology will be transformed. They will also consist of bodies of varying mass, inertia and stiffness properties. This gives rise to large variations in the system frequencies and the solution of their dynamical equations need special techniques. A general model to help study their dynamics is badly needed. A methodology to derive a general dynamics model of complex multibody systems is necessary [16]. This generalized method can be applied to serial-type kinematic chains as well as to complex architectures, namely, one that consists of serial, parallel and tree-type kinematic chains. In this method, the derivation of the unconstrained equations of motion of the multibody system is carried out using a hybrid Newton-Euler (NE) / Euler-Lagrange (EL) formulation. Later, the variational constrained forces of the system are eliminated using the natural orthogonal complement to obtain the constrained dynamical equations. This method has the simplicity of the NE formulation, but it provides a means of eliminating the non-working constraint forces arising in the NE formulations, while avoiding a reliance upon the serial-type structure of the multibody system for recursive calculations. In fact, this latter feature permits the inclusion of kinematic loops and tree architecture in this formulation.

The demands of a mushrooming aerospace industry in the 1960's prompted several researchers to undertake the derivation of the equations of motion of space vehicles, idealized as rigid bodies interconnected through hinges to form a topological tree. Hooker and Margulies [38] studied a system of interconnected rigid bodies in a tree configuration, and used the Newton-Euler formulation to derive dynamical equations of motion. In their method of analysis, also referred to as the augmented-body method, each body was con-

sidered separately as an augmented body with masses of all other bodies considered concentrated at appropriate joints. The rotational and translational equations were then written about the mass centre of the body, resulting in the explicit appearance of the constraint torques acting at the joints. Later, Roberson and Wittenberg [66] employed Lagrange multipliers to obtain the constraint torques, while a projection method to eliminate the constraint torques was also considered. A second method of analysis that emerged during this period was the direct path method, in which the rotational equations of motion are written about the body hinges or joints. This method eliminates the need for considering constraint torques at the joints [40]. Rigid body dynamics of spacecraft were also studied using Kane's equation and Newton-Euler equations.

In the 1970's, spacecraft were being designed with antennas and appendages, which exhibited distributed flexibility. Therefore, the need arose to include the elastic behavior of the spacecraft in their dynamics characterization. An inductive method to obtain the equations of motion of a system of rigid bodies with flexible appendages was also presented using Newton-Euler formulations as well as the direct-path method [37]. However, a directed modal analysis had yet to be accomplished.

The modal analysis of a flexible space station composed of a main rigid body connected to several flexible appendages needed to be addressed. In the past, several papers have been devoted to the modal analysis of rotating flexible structures [53,73]. Most of the study has been concerned with discrete models, in which the deformations are described by finite element methods or Rayleigh-Ritz methods. The analysis of the natural frequencies and modes of vibrations of a revolving space station is in general complicated by the presence of gyroscopic forces leading to real natural frequencies associated to complex eigenvectors. A stationary property for the Rayleigh's quotient has been established by Meirovitch [53].

The use of the continuum approach in the modal analysis of rotating flexible structures has been investigated by Kulla [45] and Likins, Barbera and Baddeley [49]. The approach employed in these papers has the flexible appendages of the structure modelled as an elastic rod. The mathematical modelling in these two papers represents the flexible parts of the structure as axial rods spinning about their longitudinal axis, or as radial rods spinning about axes perpendicular to the rods. The effects of three-dimensional Timoshenko beam bending have not been addressed in these models.

2.5.2 Finite Element Modelling

Traditionally, a simple dynamic finite element model (FEM) is developed to achieve improved correlation against modal test data. The detailed superelement model can be reduced to an equivalent simple model using Guyan reduction, Block Lanczos reduction or other suitable Ritz basis vectors. Effective correlation with valid test modes requires reasonable analytic modes. The process of integrating large scale finite element models (FEMs) for system structural analysis can be difficult, with the results often diverging or converging in a non-optimal sense. Thus, extensive FEM model checks are always required, and component modal synthesis (CMS) must be preceded by model verification at each component level and synthesis step [33,34].

The International Space Station substructure finite element models are designed to provide validation against vibration test modes for launch and on-orbit coupled load analysis. With the objective of improving correlation between test and analytical modes of vibration for a large scale space structure, such as the ISS, a constrained optimization formulation must be utilized in the execution of the FEM analysis. NASTRAN software has been employed by the structural team at Johnson Space Center to perform component modal synthesis based on Craig-Bampton coupled loads methodology. The Optimizer^{TM} postprocesses NASTRAN FEM modes to find the local minima for the modified FEM

without appreciably changing the design variables of the as-built test analysis model. Both analytical frequencies and mode shapes are then correlated against test modes and the FEM is modified until the correlation is satisfactory [52].

Optimum design of large-scale structures have been limited by the number of independent (or linked) design variables to less than 200, resulting from the increasing number of finite element analysis (FEA) iterations and partly from the commercial impracticability of repetitive eigenvalue analysis for updating eigenvalue/eigenvector sensitivity. The cost of performing either structural design optimization or FEM modal validation using optimality criteria is seemingly independent of the number of design variables, unlike mathematical programming in Vanderplaats' ADS code [80]. This cost-effectiveness quality of number independence in optimality criteria may also exist within the genetic search strategy proposed by Hajela [35] and in interval arithmetic, proposed by Sepulveda and Schmit [74] in pursuit of global optima. The cost of repetitive eigenvalue analysis during optimizer iterations is avoided by substituting the iterative perturbation algorithm of Van der Vooren [81] and Gupta, Newell and Roberts [33]. This algorithm updates eigenvalues, eigenvectors and their sensitivity in an approximative fashion. Patnaik, Guptill and Berke [62] discovered potential singularities in the constraint gradient matrix as a result of linear dependence among stress and displacement, but not necessarily frequency constraints, sufficient to prevent convergence of local minima. Armand and Lin [4] find that the Timoshenko beam modes are higher than those found using the NASTRAN Euler beam; mass moments of inertia and geometric stiffening resulting from pre-loading must always be taken into account, especially when modelling the photovoltaic arrays of a space station.

With frequency optimization or detuning, disjoint feasible spaces have been recognized, making the global optimization problem a challenging combinatorial problem; $(m+1)^r$ frequency subspaces exist for r retained structural modes and m forcing frequen-

cies. Allowing only one natural frequency to cross one forcing frequency, one need to examine $2r$ contiguous frequency subspaces, thus rendering the optimal mode prediction using finite element techniques difficult to interpret [74].

Large scale finite element stress models of structures, such as the ISS, are developed for the sake of including meticulous design detail. The more detailed the FEM, the higher the model fidelity, and the more difficult the problem of modal validation of the FEM, largely because of inseparable local modes, complex or coupled modes, and unobservable spurious modes.

The modal test/analysis correlation problem is formulated as a mathematical programming primal problem solved by ADS code [80], and as a dual Lagrangian solved by optimality criteria. The NASTRAN FEM of the ISS with the test boundary conditions is then modified using design sensitivity: derivatives of eigenvalues (vibration frequency) and eigenvectors (vibration modes) with respect to design variables (i.e., thicknesses, areas, moments of inertia, masses) in the physical FEM. The vibration sensitivity derivatives are then updated outside NASTRAN using an iterative perturbation algorithm during the inner optimization loop. Complete FEM analysis with MSC/NASTRAN is updated with the local minimum as an outer loop, and the optimization must be repeated until correlation is satisfactory and convergence is achieved. The objective is to adjust the design variables in the FEM so as to minimize the difference between the predicted analytical modes and the corresponding measured test modes [52]. Ideally, without any accumulated floating point error, the test and analytical modes have perfect correlation. Hence, the accuracy of the test model is vital to the proper development of a predictive FEM model.

2.5.3 Modal Test Analysis of Space Station Structures

Mathematical models of space station modules are required for the calculation of shuttle orbiter liftoff and abort landing dynamic loads, which in turn are critical for structural

design. Development of a verified structural dynamic model requires modal survey tests of the flight hardware and subsequent fine-tuning or updating of the model to obtain the best possible agreement with test data.

Constrained boundary or fixed-based tests have traditionally been used for verification of shuttle payload models, since these tests are designed to match the actual orbiter interface constraints of the payload. However, there are considerable difficulties and expense involved in development and use of fixtures for fixed based testing. Among the problems encountered are the following [78]:

1. Contamination of test data due to coupling of the test article and fixture.
2. Difficulty in accurately simulating the boundary constraints existing in flight.
3. Cost of design, construction and checkout of the fixture.

Although a modal universal test fixture (UTF) was designed specifically for tests of space station modules, it can be used for all shuttle payloads when verification is complete. Requirements for this fixture were as follows:

1. It must have no natural frequencies below 40 Hz, with a goal of 60 Hz.
2. It must accommodate all space station module elements
3. It must restrain trunnion and keel pins orbiter interfaces in all 7 orbiter constrained degrees of freedom.

While the first two requirements were met, a modal test of the space station module (SSM) prototype fixture revealed that the UTF did not properly restrain the 7 orbiter-constrained degrees of freedom [3].

In view of the difficulties and cost associated with fixed-based testing, less expensive alternative free-suspension methods have been studied, including the residual flexibility and mass-additive techniques. Both of these test methods have potential for widespread use. They are attractive partly because the suspension systems cost on the order of tens of thousands of dollars as opposed to the millions of dollars needed for the development and

construction of a large fixed-base test fixture. However, these free suspension techniques also have drawbacks and unresolved technical difficulties that are being addressed in current research efforts.

The concept behind the residual flexibility approach is that a subset of the payload free-boundary mode shapes along with the residual flexibility of the payload-to-orbiter interfaces can be used to derive the shuttle-constrained configuration. Residual flexibility of the interfaces provides an approximation of the free-boundary modes not measured. This technique of using an approximation of the effects of neglected higher-order modes, or residual modes, to improve the accuracy of reduced-basis mathematical models was first presented by MacNeal [51]. An improvement of the basic residual approach by including second-order effects, or residual mass, was presented by Rubin [72]. The main drawback to the use of the residual flexibility method is the difficulty in obtaining accurate measurements for the interface residual functions. Actual residual measurements are very noisy, making it difficult to identify the residual function. In addition, the interface frequency response function must have a well-defined stiffness line for accurate residual values to be obtainable.

In the mass-additive test technique, masses or weights are attached to the orbiter interfaces and the vibration mode shapes are measured. The idea behind this approach is that mass-loading the boundaries exercises them to a greater degree than is possible in simple free constrained boundary test and thus enhances the estimation of the constrained boundary modes. In addition, the presence of masses on the payload-to-orbiter interfaces brings the interface bending modes down into the frequency bandwidth of the test. No separate measurements need be done to characterize the interfaces, which are required in the residual flexibility approach. However, the worst case scenario accuracy of this method requires that over 100 test modes be used in order to achieve 5% frequency error [1].

Thus, the ability to verify any analytical model through modal test analysis is integral to the entire process of developing the model. Hence, modelling becomes an extremely powerful tool when validation is used properly to verify the model.

2.6 Summary

In the previous chapter, the background of the Russian Space Station Mir and the International Space Station was established. As well, the idea of a microgravity environment was addressed, especially pertaining to astronaut motions and its effect thereupon. Finally, the issue of modelling the modal dynamics of a large space structure was tackled, with attention given to the analytical, finite-element and experimental methods. The dynamic modelling of a space station is the first step in the process of determining a transfer function between an excitatory force and overall displacement, or as an extension, acceleration. This is addressed in the following chapter, which deals with the analytic modelling of a large space structure.

Chapter 3

Analytic Modelling of a Space Station

3.1 Modelling Techniques

The basis of analyzing and controlling a flexible system is developing an accurate mathematical model that represents the dynamics of the system. While there are quite convenient methods for modelling simple systems, a systematic modelling methodology is needed for more common, complex controlled structures. Therefore, the objective of this chapter is to provide the necessary structural dynamics to create an accurate model for the space station.

Because structures are continuous, the most natural manner in which to model a structural system is with continuous properties. Closed-form solutions for these problems, however, are only available for simple problems. A more common approach, especially with the onset of computers, is to discretize the structure into small elements, and solve an eigenvalue problem. This type of systematic modelling is usually much easier and simpler for modelling a complex system such as controlled structures.

However, before any approach can be made to model a structure, a study of the generalized inputs to the model must be made. Otherwise, the model sensitivities can be designed extremely poorly, yielding a model that is structurally correct but of no practical use in analyzing the overall behavior of the system.

3.2 Astronaut Motion

3.2.1 Gross Body Motion Categories

The types of motions performed by astronauts during EDLS activities can be assigned two types: active or passive. Active sessions involve the astronaut making concerted and pre-

42

determined motions. Passive sessions involve the astronaut conducting routine, average-force profile activities.

Motions performed in microgravity differ from those performed in a 1-g environment. Due to the lack of gravity to supply the traditional up-down vestibular cues, the body's sense of orientation is lost. Hence, many astronaut motions are performed in the horizontal plane, which would be impossible in a 1-g environment. As well, motions such a floating and re-orienting in free space are completely viable, and require what appears to be very little force. The motions performed by the astronauts can roughly be divided into several categories. The motions identified as being performed were [2]:

1. Pushoffs
2. Landings
3. Flexion/Extension
4. Singly Supported Stance
5. Doubly Supported Stance
6. Re-Orientation
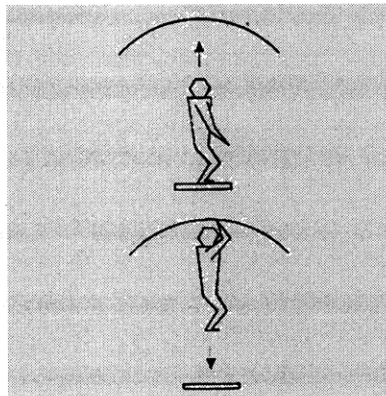
Figure 3.1: Push Off and Landing Motion [44]

The pushoff motion is usually one of the most forceful, and is comprised of the astronaut engaged with the sensor and then leaving the surface of the sensor, usually the footloop or the touchpad by projecting themselves forwards using their feet, toes, or fingers. The landing motion is also quite forceful, and involves the astronaut landing on a sensor surface, such as the footloop or the touchpad, occasionally using the handhold to slow

down their motion, creating a torque about the ankles. Flexion and extension involve the astronaut in a position where movement is restrained by the sensor, such as the footloop or the handhold, and flexing or extending the appropriate muscle groups to accomplish the desired motion. Singly and doubly supported stances refer to the astronaut being supported by either one or two contact limbs to a sensor or sensors, respectively. The re-orientation motion involves the astronaut changing his/her spatial attitude.

As well, passive operations of console and computer operation were performed. The astronaut remained in contact with the force sensor while performing motions typically associated with console and computer operation, such as flipping switches, hand-controller inputs and keyboard entries. The force profiles obtained from these activities can be used to create a baseline for stochastic model definition [8].

All of these motions included simple arm and leg movements in acts which can be characteristic of motions encountered in day-to-day operation about a space station. These motions can be used to extract the magnitudes of the loads applied to the space station, and ultimately can be modelled as a forcing input to a space station simulation. Thus, with the proper predictive capabilities inherent in a transfer function, general conclusions can be drawn with respect to the types of loads applied by astronaut motions, and their predicted response in the modelled behavior of the space station [12].

3.2.2 Model Input Approximations

Astronaut motion force and moment profiles are useful in the design of future spacecraft control systems, as well as in the verification of existing astronaut-station motion models. In general, a astronaut-motion force-time profile can be viewed as a stochastic process. It can be analyzed by its corresponding power spectral density, and thus the relationship between the energy and frequency of the motion can be divined. These frequency energy correlations can then be used to create the idealized forcing inputs that act to perturb the

model [8].

A caveat must be maintained, insomuch as that in any model, the simulation only approximates the actual problem and corresponding physical situation. Thus, the dynamic behavior of the space station must first be approximated using the rotational dynamics of a rigid body, then by the flexible body dynamics using the normal mode method. As well, the gravity gradient moment must be considered in all cases where moments are investigated, however a study of moments is beyond the scope of this text. In most cases, in the attempt to reduce the cost of analysis, a simple first order transfer function is usually approximated for each of the dominant modes of the system [14].

A simplified first order approximation was tested in the Skylab T-013 experiments, and it was found that the peak-to-peak values of the outputs show that the simplified model produces outputs of the order of 10-25% lower than a complex model [13].

3.3 Modelling of a Single Module

The Russian Space Station Mir is composed of a central node, branching into several modules, such as Priroda, where a majority of the EDLS passive session experiments occurred (Fig. 3.2). Some of the experimental data, that is, all of the active sessions, was recorded in the central block, but for modelling purposes, the effect of the experiment upon a single extended module shall first be considered.

Essentially, if the assumption can be made that the mass of the entire space station greatly outweighs the mass of an individual module, the module can be said to be, as a rough first-cut approximation, a clamped-free beam. More commonly know as a cantilever beam, clamped-free beams are constrained at one end and free at the other, and can be modelled exactly through analytic means.
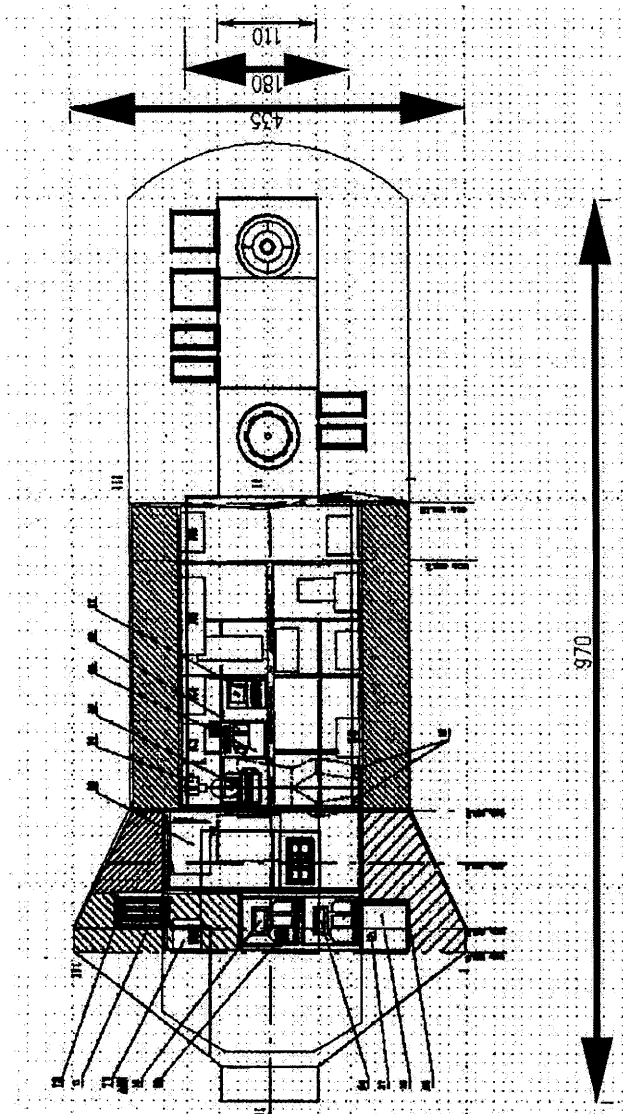
Figure 3.2: Schematics of Priroda Module [39]

3.3.1 Generalized Analytic Solution for Euler Bernoulli Beam

The general Euler-Bernoulli equation for transverse vibrations in a beam is governed by:

$$\frac{\partial^2}{\partial x^2}\left(EI\frac{\partial^2 v}{\partial x^2}\right) + \rho A\frac{\partial^2 v}{\partial t^2} = p(x, t) \tag{3.1}$$

where E is Young's modulus of elasticity for the beam, I is the moment of inertia of the beam, ρ is the density of the beam, A is the cross-sectional area of the beam, p(x,t) is the

46

forcing function, and v(x,t) is the deflection of the elastic line of the beam.

For free vibrations, this reduces to:

$$\frac{\partial^2}{\partial x^2}\left(EI\frac{\partial^2 v}{\partial x^2}\right) + \rho A\frac{\partial^2 v}{\partial t^2} = 0 \tag{3.2}$$

Assuming harmonic motion given by the equation:

$$v(x, t) = V(x)\cos(\omega t - \alpha) \tag{3.3}$$

and substitute (3.3) into (3.2) to get the eigenvalue equation:

$$\frac{d^2}{dx^2}\left(EI\frac{d^2 V}{dx^2}\right) - \rho A\omega^2 V = 0 \tag{3.4}$$

Since closed-form solutions are not available for this equation with variable coefficients, the model will be restricted to examine the free vibration of uniform beams. Free transverse vibration of uniform beams has been extensively studied, and the mode shapes of uniform beams have frequently been used in conjunction with approximation methods [14].

For the free vibration of a uniform beam, equation 3.4 reduces to:

$$\frac{d^4 V}{dx^4} - \lambda^4 V = 0 \tag{3.5}$$

where:

$$\lambda^4 = \frac{(\rho A\omega^2)}{EI} \tag{3.6}$$

The general solution of equation 3.6 may be written in the form:

$$V(x) = A_1 e^{\lambda x} + A_2 e^{(-\lambda x)} + A_3 e^{i\lambda x} + A_4 e^{(-i\lambda x)} \tag{3.7}$$

A more useful alternative form is:

$$V(x) = B_1 e^{\lambda x} + B_2 e^{(-\lambda x)} + B_3 \sin(\lambda x) + B_4 \cos(\lambda x) \tag{3.8}$$

This can be modified to the form:

$$V(x) = C_1 \sinh(\lambda x) + C_2 \cosh(\lambda x) + C_3 \sin(\lambda x) + C_4 \cos(\lambda x) \tag{3.9}$$

The arbitrary constants C_i must then be determined by substituting in the appropriate end conditions based on the type of beam element being modelled.

3.3.2 Boundary Conditions

There are five constants in the general solution, that is, four amplitude constants and the eigenvalue λ. The boundary conditions are used in evaluating these constants as will be illustrated below. For the free vibration of uniform beams, the following end conditions are the most common:

(a) Fixed End:

$$V = 0$$
$$\frac{dV}{dx} = 0 \tag{3.10}$$

(b) Simply Supported or Pinned End:

$$V = 0$$
$$\frac{d^2V}{dx^2} = 0 \tag{3.11}$$

(c) Free End:

$$\frac{d^2V}{dx^2} = 0$$
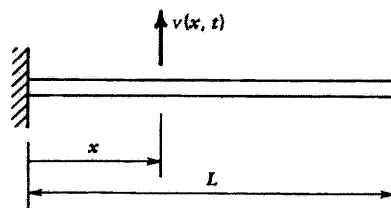$$\frac{d^3V}{dx^3} = 0 \tag{3.12}$$
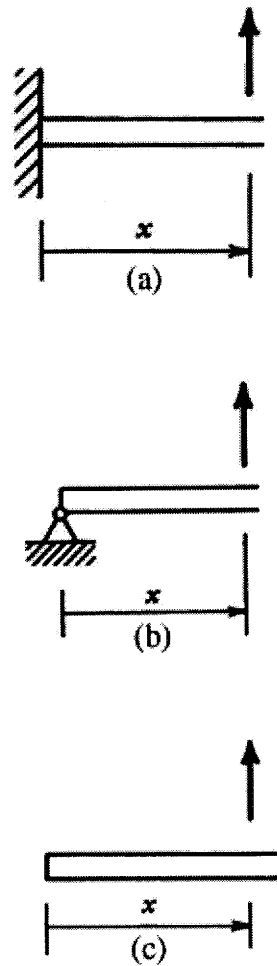
Figure 3.3: End Conditions (a) Fixed (b) Pinned (c) Free

Substitution of the correct end conditions into the Euler-Bernoulli generalized solution

will lead to the determination of the four constants of integration and the eigenvalues.

3.3.3 Particular Solution for a Cantilever Beam

Figure 3.4: Cantilever Beam

Now, employing the general solution given in equation 3.9,

$$V(x) = C_1 \sinh(\lambda x) + C_2 \cosh(\lambda x) + C_3 \sin(\lambda x) + C_4 \cos(\lambda x) \qquad (3.13)$$

with boundary conditions given by:

$$V(0) = 0$$
$$\left. \frac{dV}{dx} \right|_{x=0} = 0 \qquad (3.14)$$

at the clamped end x = 0 and

$$\left. \frac{d^2 V}{dx^2} \right|_{x=L} = 0$$
$$\left. \frac{d^3 V}{dx^3} \right|_{x=L} = 0 \qquad (3.15)$$

at the free end x= L, the coefficients can be determined.

From equation 3.13 we have:

$$\frac{dV}{dx} = \lambda(C_1 \cosh(\lambda x) + C_2 \sinh(\lambda x) + C_3 \cos(\lambda x) + (-C_4) \sin(\lambda x)) \qquad (3.16)$$

$$\frac{d^2 V}{dx^2} = \lambda^2 (C_1 \sinh(\lambda x) + C_2 \cosh(\lambda x) + (-C_3) \sin(\lambda x) + (-C_4) \cos(\lambda x)) \qquad (3.17)$$

$$\frac{d^3 V}{dx^3} = \lambda^3 (C_1 \cosh(\lambda x) + C_2 \sinh(\lambda x) + (-C_3) \cos(\lambda x) + C_4 \sin(\lambda x)) \qquad (3.18)$$

Substituting the general equation and its derivatives into the boundary conditions, the following equations result. For convenience, they have been placed into matrix form:

$$\begin{bmatrix} 0 & 1 & 0 & 1 \\ \lambda & 0 & \lambda & 0 \\ \lambda^2 \sinh \lambda L & \lambda^2 \cosh \lambda L & -\lambda^2 \sin \lambda L & -\lambda^2 \cos \lambda L \\ \lambda^3 \cosh \lambda L & \lambda^3 \sinh \lambda L & -\lambda^3 \cos \lambda L & \lambda^3 \sin \lambda L \end{bmatrix} \begin{bmatrix} C_1 \\ C_2 \\ C_3 \\ C_4 \end{bmatrix} = \begin{bmatrix} 0 \\ 0 \\ 0 \\ 0 \end{bmatrix} \qquad (3.19)$$

For this set of homogeneous equations to have a nontrivial solution, the determinant of the coefficients must vanish.

This leads to the characteristic equation:

$$2\cosh\lambda L\cos\lambda L + \sin^2\lambda L + \cos^2\lambda L + \cosh^2\lambda L - \sinh^2\lambda L = 0 \qquad (3.20)$$

which yields the transcendental relation:

$$\cos\lambda L\cosh\lambda L + 1 = 0 \qquad (3.21)$$

whose roots are the eigenvalues λ_r times the beam length L. No simple expression for the roots of the characteristic equation is available, so a numerical solution is required. These values have been computed, using Newton's method, to be:

$$\lambda_1 L = 0.597\pi$$
$$\lambda_2 L = 1.49\pi$$
$$\lambda_3 L = \left(\frac{5}{2}\right)\pi \qquad (3.22)$$
$$\lambda_4 L = \left(\frac{7}{2}\right)\pi$$

And, from our definition of λ, it is known that:

$$\omega_r = (\lambda_r L)^2 \sqrt{\frac{EI}{\rho AL^4}} \qquad (3.23)$$

so:

$$\omega_1 = \frac{3.516}{L^2}\left(\frac{EI}{\rho A}\right)^{1/2}$$
$$\omega_2 = \frac{22.03}{L^2}\left(\frac{EI}{\rho A}\right)^{1/2} \qquad (3.24)$$
$$\omega_3 = \frac{61.70}{L^2}\left(\frac{EI}{\rho A}\right)^{1/2}$$

This illustrates that there is an infinite number of degrees of freedom of the system, that is, there are an infinite number of eigenvalues, and thus an infinite number of eigenfunctions, or mode shapes. To determine the mode shape, three of the four equations in the matrix are utilized to express three of the constants in terms of the fourth, which remains arbitrary. The first two relations in the matrix of equations in (3.19) yield:

$$C_4 = -C_2 \qquad (3.25)$$

51

$$C_3 = -C_1 \tag{3.26}$$

The third equation says that:

$$C_1 \sinh(\lambda_r L) + C_2 \cosh(\lambda_r L) - C_3 \sin(\lambda_r L) - C_4 \cos(\lambda_r L) = 0 \tag{3.27}$$

which can be combined with the previous two relations to give:

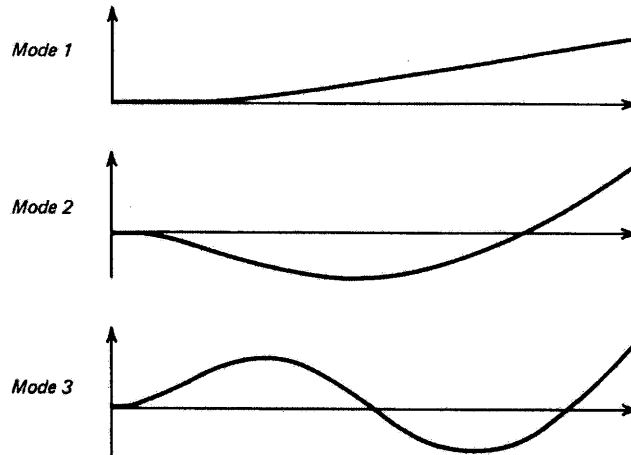$$C_1 \sinh(\lambda_r L) + C_2 \cosh(\lambda_r L) + C_1 \sin(\lambda_r L) + C_2 \cos(\lambda_r L) = 0 \tag{3.28}$$

or:

$$C_1 = -C_2 \left[\frac{\cosh(\lambda_r L) + \cos(\lambda_r L)}{\sinh(\lambda_r L) + \sin(\lambda_r L)} \right] = -k_r C_2 \tag{3.29}$$

These constants can then be substituted back into the general solution for an Euler-Bernoulli bean to give the mode shapes

$$V_r(x) = C\{ \cosh(\lambda_r x) - \cos(\lambda_r x) - k_r [\sinh(\lambda_r x) - \sin(\lambda_r x)] \} \tag{3.30}$$

where k_r is given by the above equation and C is an arbitrary amplitude constant. Three of the uniform modes are sketched below.

Figure 3.5: Cantilever Beam Mode Shapes

## 3.4 Model of Multiple Module Configuration

With the introduction of the multiple module approach, it is necessary to reflect upon the configuration of such a model. Essentially, the space station appears as a series of protrusions oriented around a central node.
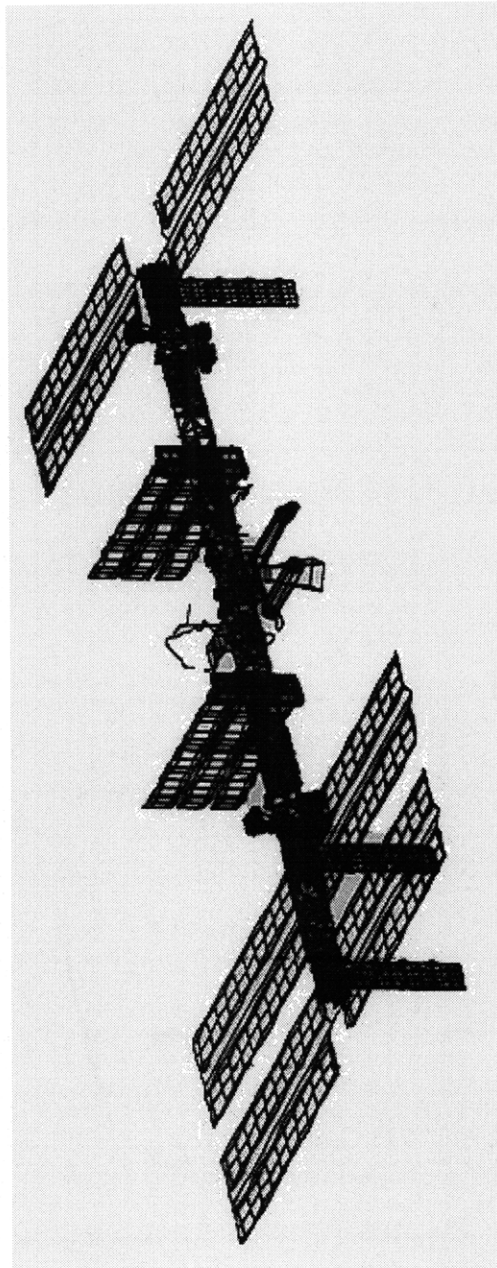
Figure 3.6: Finite Element Orientation of ISS [52]

If axes are assigned to the configuration, it can be seen that the modules can be pictured as lying along either the principle x, y or z axes, in relation to the origin at the central node. This arrangement of modules can be approximated roughly as a series of free-free beams, intersecting with one another aligned through a principle axis.

3.4.1 Free-Free Beam Configuration
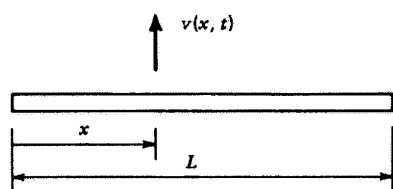
Figure 3.7: Free-Free Beam

Utilizing the generalized equation 3.1 above, all that is needed is to substitute in the boundary conditions:

$$\frac{d^2V}{dx^2}\bigg|_{x=0} = 0$$

$$\frac{d^3V}{dx^3}\bigg|_{x=0} = 0 \tag{3.31}$$

at the end x=0 and

$$\frac{d^2V}{dx^2}\bigg|_{x=L} = 0$$

$$\frac{d^3V}{dx^3}\bigg|_{x=L} = 0 \tag{3.32}$$

at the end x=L, and the transcendental equation can be arrived at, and the necessary eigenfrequencies and eigenfunctions can be determined:

$$\cosh\lambda L \cos\lambda L - 1 = 0 \tag{3.33}$$

$$\omega_r = (\lambda_r L)^2 \sqrt{\frac{EI}{\rho A L^4}} \tag{3.34}$$

$$V_r(x) = C\{\cosh(\lambda_r x) + \cos(\lambda_r x) - k_r[\sinh(\lambda_r x) + \sin(\lambda_r x)]\} \tag{3.35}$$

$$k_r = \left[\frac{\cosh(\lambda_r L) - \cos(\lambda_r L)}{\sinh(\lambda_r L) - \sin(\lambda_r L)}\right] \tag{3.36}$$

to arrive at the first three modes:

$$\omega_1 = \frac{(0)}{L^2}\left(\frac{EI}{\rho A}\right)^{1/2}$$

$$\omega_2 = \frac{(0)}{L^2}\left(\frac{EI}{\rho A}\right)^{1/2} \tag{3.37}$$

$$\omega_3 = \frac{61.685}{L^2}\left(\frac{EI}{\rho A}\right)^{1/2}$$

However, there is one major caveat of interest. It becomes immediately apparent from the equations that the beam has two zero-frequency, or rigid-body modes. The first mode comprises the body's ability to translate freely, and the second mode corresponds to the body's ability to rotate freely within the environment. Rigid body modes indicate the inability of the structure to store elastic potential energy during the execution of the mode.

These rigid body modes are dominant within the free-free beam structure, and thus it is a good approximation to say that these free-free beams behave in a cantilever fashion about their center of gravity [53].

Mode 1
Translation (plunge)
rigid-body mode

Mode 2
Rotation (roll)
rigid-body mode

Mode 3
Flexible mode
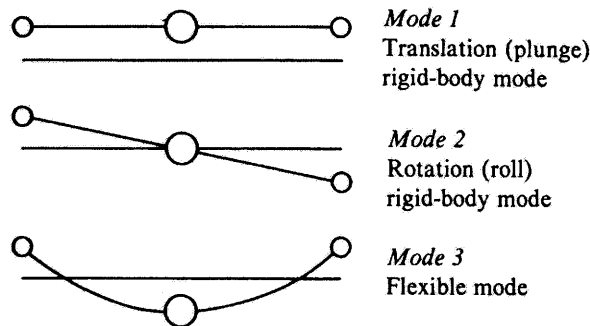
Figure 3.8: Free-Free Mode Shapes

Hence, the original approximation of a single module acting as a cantilever beam to the first order is justified.

3.5 Higher Mode Shape Estimation

The vibration modes and frequencies of uniform Euler beams for various boundary end conditions are traditionally expressed in terms of $\sin\lambda_n$, $\cos\lambda_n$, $\sinh\lambda_n$, $\cosh\lambda_n$ functions. For modes above the second, however, the numerical evaluation of these modes requires an increasingly large number of significant figures to be kept in order to distinguish small differences between $\sinh\lambda_n$, $\cosh\lambda_n$. Thus, what is needed is a simple expression for arbitrarily high-order modes and frequencies of uniform Euler beams, which also help to identify the physical nature of the mode shapes [14].

Consider for example, the free-free uniform Euler beam:

$$V_r(x) = C\{\cosh(\lambda_r x) + \cos(\lambda_r x) - k_r[\sinh(\lambda_r x) + \sin(\lambda_r x)]\} \tag{3.38}$$

$$k_r = \left[\frac{\cosh(\lambda_r L) - \cos(\lambda_r L)}{\sinh(\lambda_r L) - \sin(\lambda_r L)}\right] \tag{3.39}$$

If we non-dimensionalize the x coordinate with respect to L, and allow x to vary between 0 and 1, the mode shape satisfies the condition:

$$\int_0^1 V_n^{\,2}(x)dx = 1 \tag{3.40}$$

By adding and subtracting $\sinh\lambda_n$, the equation for the mode shape can be arranged into the form:

$$V_r(x) = \cosh(\lambda_r x) - k_r\sin(\lambda_r x) + (1 - k_r)\sinh(\lambda_r x) + e^{-\lambda_r x} \tag{3.41}$$

Introducing the expression for k_r, we can write:

$$\lambda_r \approx \left(r + \frac{1}{2}\right)\pi \tag{3.42}$$

where this solution for λ_r is found by plotting the right and left hand sides of the transcendental equation for the free-free beam. Since $e^{-\lambda_r r} \ll 1$ and $k_r \approx 1$, the higher vibration modes of uniform Euler beams with $n \geq 2$ can be approximated as:

$$V_r(x) = \sqrt{2}\sin(\lambda_r x + \theta) + Ae^{-\lambda_r x} + Be^{-\lambda_r(1-x)} \qquad (3.43)$$

where the constraints λ_r, θ, A, B are given in Table 3.1 below.

Table 3.1: Higher Mode Constants for Equation 3.43 [14]

| Boundary Condition	λ_r	θ	A	B
SS[a]-SS	$n\pi$	0	0	0
CL[b]-FR	$\left(n-\dfrac{1}{2}\right)\pi$	$\dfrac{-\pi}{4}$	1	$(-1)^{n+1}$
CL-CL	$\left(n+\dfrac{1}{2}\right)\pi$	$\dfrac{-\pi}{4}$	1	$(-1)^{n+1}$
FR[c]-FR	$\left(n+\dfrac{1}{2}\right)\pi$	$\dfrac{3\pi}{4}$	1	$(-1)^{n+1}$
SS-CL	$\left(n+\dfrac{1}{4}\right)\pi$	0	0	$(-1)^{n+1}$
SS-FR	$\left(n+\dfrac{1}{4}\right)\pi$	0	0	$(-1)^n$

a. Simply Supported End (SS)
b. Clamped End (CL)
c. Free End (FR)

3.6 Comparison to Actual Experimental Mode Shapes

The origin of the ISS reference coordinate system is located at the center of the S0 Truss segment. The S0 Truss Segment interfaces with the S1 Truss Segment, the P1 Truss segment, the LAB and the Mobile Transporter (Fig 1.1, Fig. 3.9). The positive x-axis direction coincides with the ISS flight direction, the positive y-axis is pointing toward the ISS starboard end. The right-hand rule defines the positive z-axis direction that points towards the Earth. The following figure demonstrates the alpha, beta and gamma angle rotation convention. The baseline configuration of the integrated system is defined as alpha and beta identically zero, and gamma as ninety degrees.
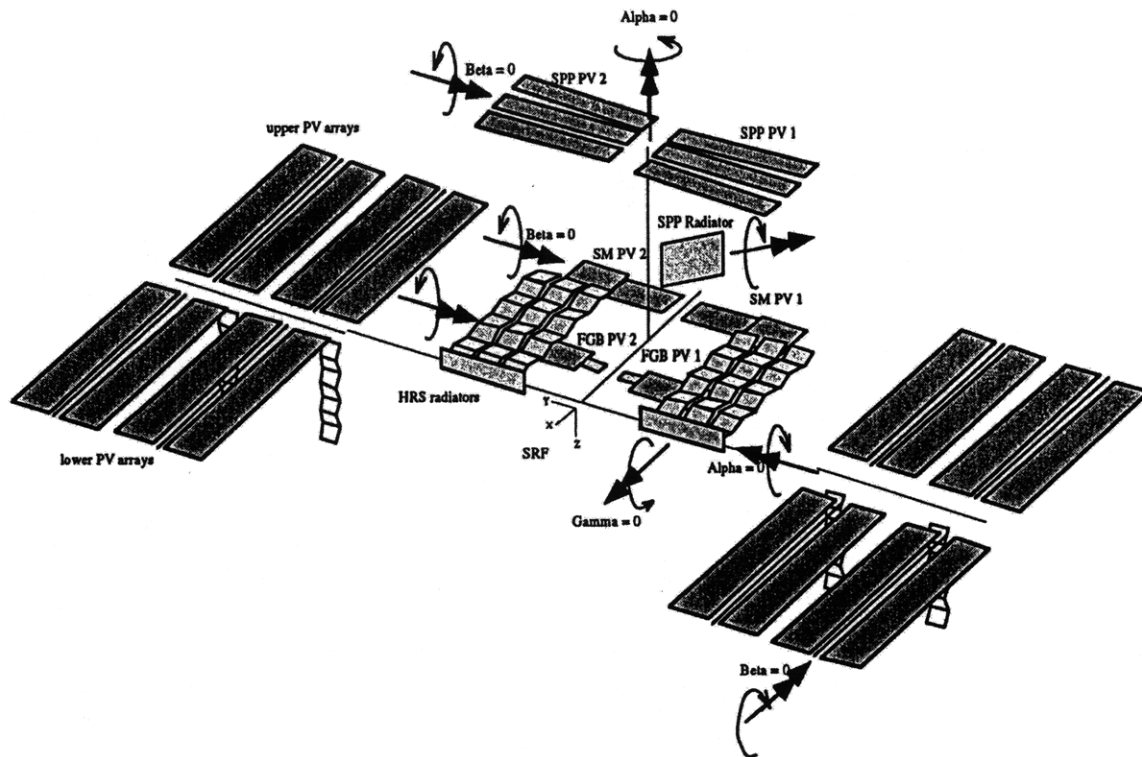
Figure 3.9: ISS with Truss and Angle Labelling (Stage 13) [52]

A total of 39 stage configurations occur during the assembly of the International Space Station. At the Johnson Space Center, a detailed finite element model was prepared, and the MSC/NASTRAN Superelement Eigensolution option using the Lanczos extraction method was employed to perform the normal mode analyses for thirteen configurations. The DMAP option, which performs comprehensive strain energy and total model weight calculations were also used to check the quality of the assembled system models. All system models rigid body modes were inspected for sufficient separation from the first system elastic mode. Visual inspection of the deformed and undeformed system mode shape plots were also performed.

Russian segment on-orbit transient loads analysis models were delivered by ERSC-Energia and Khrunichev centers for further ISS analysis [71]. These models were defined

in geometry, mass and stiffness properties of equivalent beam members in metric SI units. There was no model check-out documentation provided for these models.

The Functional Cargo Block (FGB) model is the first element launched for the construction of the International Space Station. The photovoltaic arrays were retracted for the initial launch, but were immediately deployed upon arrival into stable orbit upon day 13 of the mission. Due to the lack of structural properties for the retracted FGB arrays, they are modelled as rigid masses lumped at the array mast base. The mass properties of the FGB with respect to the Space Station coordinate system are:

Table 3.2: Properties of the FGB Array [52]

Axis	X	Y	Z
Weight (N)	188 057	188 057	188 057
Rotational Inertia (Pa)	$1.903{\times}10^6$	$3.454{\times}10^6$	$4.261{\times}10^6$
Centre of Gravity (m)	-16.083	0.000	4.199

Using this data and the previous analysis, the calculated natural frequencies for the Free-Free configuration of the FGB module are given by:

Table 3.3: First Five Modes of FGB Array

Mode Number	Free-Free Frequency
1	$1.8{\times}10^{-5}$
2	$2.1{\times}10^{-5}$
3	$2.5{\times}10^{-5}$

Table 3.3: First Five Modes of FGB Array

Mode Number	Free-Free Frequency
4	3.4×10^{-5}
5	5.1×10^{-5}

3.7 Transfer Function Modelling

So far, some experimentation and finite element simulations have been done in order to gain some insight into the behavior of complex, multibody space structures. In designing the structure and mission operations of the International Space Station, numerical analysis with dynamic math models and estimated input forces are primarily used to predict how a structure will react to given loads.

On-orbit dynamic analytic models of the ISS are generated by combining component analytic models that are correlated with ground-test results. However, there will be modelling errors, even with ground tests, due to different boundary conditions, different mass distribution and gravity effects in addition to test noise. Load prediction errors come from forcing function estimation and dynamic analysis methodology[1], which can also be called modelling errors in a broader definition [10].

When analyzing and predicting on-orbit structural and dynamic loads for the ISS, uncertainly factors are used to compensate for the load prediction errors. The later stage configurations of the ISS will have greater uncertainties due to an accumulation of component model errors. On-orbit testing of earlier ISS configurations, with ground testing of new hardware components, will lead to the verification of later, more complex configurations. This "phased verification" allows for the use of the same uncertainty factors in predicting structural dynamic loads and correlating them to overall accelerations [52].

---

1. In addition to the errors inherent in the analytic model.

3.7.1 The Descretized Structural Model

An analytic, closed form solution model for a complex structure quickly becomes cumbersome to work with for practical purposes. This analytical model is usually descretized and then transformed into a state space representation for simplicity sake [10]. The state space model can then be used to create an evaluatable model for the system. A further objective is to understand how many modal elements effect transfer function representations.
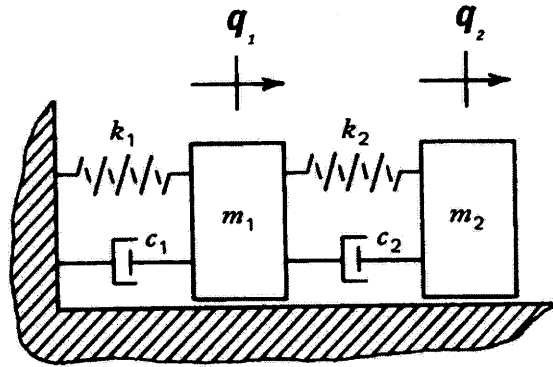
Figure 3.10: Discrete Approximation to Cantilever Beam

The actual starting point is the descretized structural model:

$$[M]\{\ddot{q}\} + [C]\{\dot{q}\} + [K]\{q\} = \{Q\} = [\beta_u]\{u\} + [\beta_w]\{w\} \tag{3.44}$$

where M, C and K are the mass, damping and stiffness matricies, q and Q are the generalized displacements and forces, β_u and β_w are the control and exogenous input matricies, and u and w are the control inputs and exogenous inputs.

The output equations can be expressed in the state space form as:

$$y = \begin{bmatrix} [C_{yq}] & [C_{y\dot{q}}] \end{bmatrix} \begin{bmatrix} q \\ \dot{q} \end{bmatrix} + [D_{yu}]u + [D_{yw}]w \tag{3.45}$$

$$z = \begin{bmatrix} [C_{zq}] & [C_{z\dot{q}}] \end{bmatrix} \begin{bmatrix} q \\ \dot{q} \end{bmatrix} + [D_{zu}]u + [D_{zw}]w \tag{3.46}$$

where y is the control measurement and z is the performance output or matrix, $C_{\dot{q}}$ and $C_{\ddot{q}}$ are the output matricies and the D matricies allow for a direct feedthrough of the inputs, u and w, to the outputs, y and z. In general, the measurement and performance outputs can be distinct spatially or temporally.

In the simplest form of the transformation, Equation 3.44 is transformed to modal co-ordinates. Solving the undamped free vibration case, $(C=0, Q=0)$, yields:

$$[M]\{\ddot{q}\} + [K]\{q\} = 0 \tag{3.47}$$

where M and K are NxN matricies. Letting:

$$q = \{\phi\}e^{\lambda t} \tag{3.48}$$

and substituting (3.48) into (3.47) gives the characteristic equation:

$$\lambda^2[M]\{\phi\} + [K]\{\phi\} = \{0\} \tag{3.49}$$

There are $2N$ solutions to this eigenvalue problem. These solutions appear in complex conjugate pairs:

$$\begin{aligned} \lambda_r &= j\omega_r \\ \lambda_{r+N} &= -j\omega_r \end{aligned} \tag{3.50}$$

which are paired with the same eigenvectors, the normal modes of the undamped system, that is $j\omega_r$ and $-j\omega_r$ are associated with the same mode ϕ_r. The orthogonality conditions of the system are given by:

$$\{\phi_r^T\}[M]\{\phi_r\} = m_r\delta_{rs} \tag{3.51}$$

$$\{\phi_r^T\}[K]\{\phi_r\} = m_r\omega_r^2\delta_{rs} = -m_r\lambda_{r+N}^2\delta_{rs} \tag{3.52}$$

where m_r is the modal mass and δ_{rs} is the Kroneker delta. The degrees of freedom can be expanded in terms of the normal modes:

$${q} = [\Phi]{\xi} \tag{3.53}$$

where

$$\Phi = [\phi_1 ... \phi_N] \tag{3.54}$$

is a matrix of the individual eigenvectors. Substituting into the undamped form of the structural model, pre-multiplying by Φ^T, and invoking orthogonality gives:

$$[m_r]\{\ddot{\xi}\} + [m_r\omega_r^2]\{\xi\} = [\Phi^T][\beta_u]\{u\} \tag{3.55}$$

Thus, the theoretical transfer function is given by transforming the preceding equation into the Laplace domain, where the response of the rth mode to a scalar input u is given by:

$$\xi_r = \frac{\{\phi_r^T\}[\beta_u]}{m_r(s^2 + \omega_r^2)}u \tag{3.56}$$

Substituting (3.56) into (3.53) then using this result to solve for the displacement output y in (3.45) gives:

$$y = \sum_{r=1}^{N} \frac{[C_{yq}]\{\phi_r\}\{\phi_r^T\}[\beta_u]}{m_r(s^2 + \omega_r^2)}u \tag{3.57}$$

which shows how the modal observability $[C_{yq}]\{\phi_r\}$, modal controllability $\{\phi_r^T\}[\beta_u]$ and modal mass m_r influences the response of the transfer function at any given pole $\pm j\omega_r$.

It is a very simple matter then to take the time derivative of this expression twice to obtain the transfer function between the acceleration of the module ($\ddot{y}$) and the input force ($Q = ([\beta_u]u)$).

$$\ddot{y} = \sum_{r=1}^{N} \frac{[C_{yq}]\{\phi_r\}\{\phi_r^T\}[\beta_u]}{m_r(s^2 + \omega_r^2)}s^2 u \tag{3.58}$$

3.8 Summary

In summary, it can be seen that a modular space station can be approximated as an inter-

section of free-free beams. Free-free beams which share a common fixed point of intersection behave as cantilever beams about this point of intersection. Thus, the modal response of a space station can be taken as the superposition of all the mode shapes from all of the cantilever beam-modules.
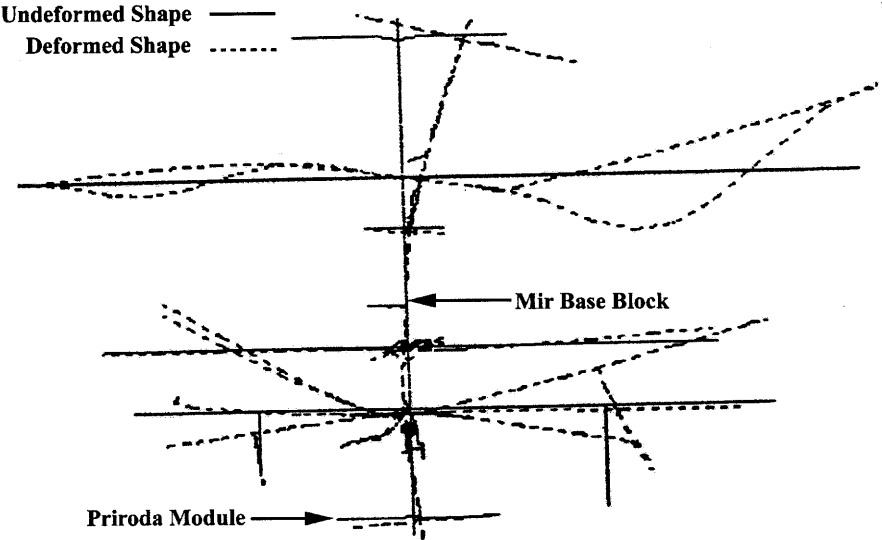
Figure 3.11: Mir Skeleton Modal Behavior in the Y Plane [71]

This continuous model was then descretized and truncated. A representation for the transfer function between a force input and a displacement output was found. It is a simple matter to take the derivative with respect to time of this transfer function, in the frequency domain, in order to convert the output into an acceleration, in order to gain the correct form of the transfer function to match the experimental data.

Chapter 4

EDLS Experimental Data Analysis

This chapter concerns the processing and analysis of the data retrieved from the EDLS space flight experiment. The EDLS experiment is described, and mention is made of the hardware problems encountered that led to the need for extensive post-calibration of the results. Once the data had been rendered into a form viable for analysis, further data correlation and reduction occurred to glean a proper measure of the actual forces being enacted.

4.1 Enhanced Load Sensors Experiment

4.1.1 Motivation

The International Space Station will be built in 77 stages using the U.S. Space Shuttle and Russian Launch vehicles starting in 1998. It is planned to operate for at least 15 years to conduct science and engineering projects [41]. But, as of yet, there has been little experience regarding how this complex structure will behave in space, especially under the influence of a permanent human presence. The effects of astronaut motions, and its quantification is the essential thrust of the EDLS experiment.

The Dynamic Load Sensor (DLS) experiment, performed on STS-62 in 1994 was the first quantification of astronaut-induced reaction forces since the Skylab program. The Skylab experiments had been performed under different experimental conditions than the DLS experiments, in the fact that the entire Skylab data set was essentially recorded in a single day, with the majority of the data being taken in a single 78 minute session. As well, a single astronaut subject performed a prescribed set of motions, such as "vigorous soaring" that involved a violent flapping of the arms, which produced loads with a maxi-

mum of 400 N [13]. These prescribed motions are not characteristic of the nominal astronaut motions created by astronauts on Mir, as observed by the video footage recorded by the EDLS experiment. Hence, a further study of nominal astronaut motions needed to be carried out.

The DLS experiment was designed in order to expand upon the data observed in the Skylab experiments, and create a database of nominal astronaut motions and forces. The DLS experiments took place on board the Space Shuttle, and were previously discussed briefly.

It should be noted that the Russian Space Station Mir has lower natural structural frequencies (approx. 1-5 Hz) than the Space Shuttle, where the DLS experiments were run [5]. This is primarily due to the size and structural differences between the two vehicles. Thus, further investigation of the effects of astronaut motion on a large structure, such as Mir, needed to be carried out in order to assist in the eventual design of a space station. The three main objectives for the EDLS experiment are the characterization of typical astronaut motion in microgravity, the measurement of the nominal astronaut-induced forces and moments during an extended stay in orbit and the quantification of changes in the forces and moments over time as the astronaut adapts to microgravity [58].

4.1.2 Experimental Protocol
The EDLS experiment used similar hardware to the DLS on the Shuttle. However, the addition of enhanced software, as well as a second foot restraint to the EDLS sensor arsenal allowed for the conduction of "active" operations sessions. One of the major breakthroughs was the addition of event detection software, where the data acquisition system only triggered once a certain force or moment threshold had been surpassed. By setting an appropriate threshold level, the data acquisition system operated continuously once activated by the astronaut but recorded only useful events [2].

The typical position of the EDLS sensors was in the Priroda module of the Russian Space Station Mir. The astronauts were encouraged to move the sensors to the location that best suited them. This occasionally lead to problems, as incorrect detachment of the sensors while the data acquisition system was still active created force spikes of approximately 500 N to 1000 N, and biased all further measurements.

During the course of the EDLS spaceflight experiment, the astronauts conducted two types of data collection sessions, passive sessions and active sessions. In a passive session, data acquisition was activated and the astronaut went about their regular business and whenever the forces/moments exceeded the threshold specified, data was recorded. In the active sessions, the astronauts used one or more foot restraints and conducted a throwing experiment. In the experiment the subjects were asked to throw a small ball at a target approximately 1.5 meters away with either hand and their eyes either open or closed.

Essentially, two sets of data exist from the EDLS experiment on Mir. Data was taken with Shannon Lucid operating the EDLS experiment during the NASA-2 mission, where thirty four sessions were recorded, two of which were active sessions, the remaining thirty two, passive sessions. Jerry Linenger was responsible for ELDS operations on the NASA-4 mission. From February 25 through May 9, 1997, Linenger initiated eighteen sessions, including six active ones. For the NASA-4 experiment, there were 5 different subjects participating; there were two to three subjects per active session; Subject 1 was in 5 sessions, Subject 2 was in 4 sessions, Subject 3 in 4 sessions and Subject 4 in 4 sessions, and Subject 5 in 1 session. It should be noted that after August 28th, 1996 the original data acquisition system failed to activate, thereby leading to no data being taken by John Blaha during the NASA-3 mission. The substitution of an alternate data acquisition system in order to render the experiment operable necessitated a great deal of post-flight calibration for the NASA-4 data [2].

4.1.3 Postflight Calibration of NASA-4 Data

Due to the substitution of a replacement data acquisition system for the NASA-4 mission, the EDLS sensors were calibrated postflight. The procedure for calibrating the handhold and foot restraints for forces and moments was identical. The touchpad was only calibrated for forces, as it was incapable of measuring moments.
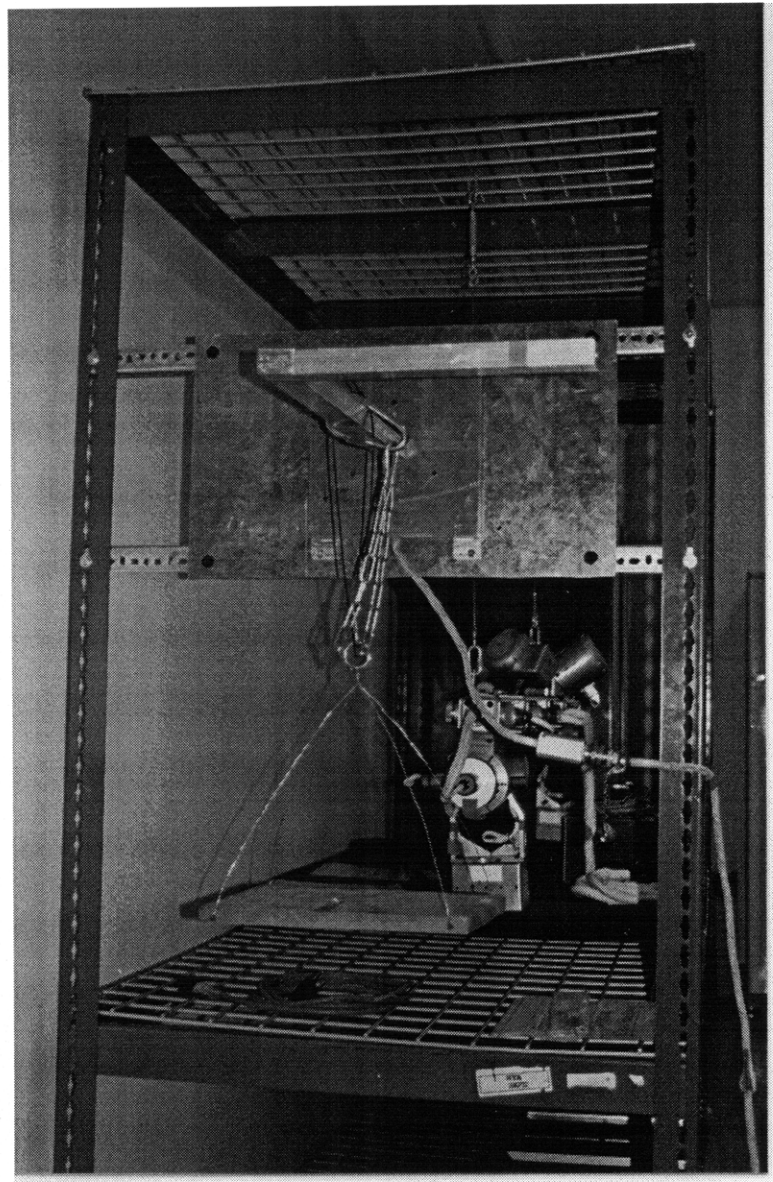
Figure 4.1: EDLS Load Sensor Postflight Calibration

The calibration procedures were as follows: the top plate of the sensor was removed and replaced with an aluminum plate of approximately the same size with an L-shaped aluminum bar on top of it. The sensor with the L-shaped bar was mounted vertically on a rack, so that gravity would act either in the $-y$ or in the $-x$ -direction. Thirteen weights ranging from 1.00 to 40.13 lb (0.455–18.20 kg) were suspended from the bar. There were four possible locations on the bar from which the weights were hung: (1) flush against the plate to create no moment, (2) in the middle of the long-section of the L-shaped bar to create a small moment, (3) at the end of the long-section of the L-shaped bar to create a large moment, and (4) at the end of the short section of the L-shaped bar to create moments about two axes. The sensor was then rotated on the rack as to apply forces and moments about another axis. To record forces in the z -direction, the sensor was placed on a flat surface, the L-shaped bar and its plate removed, and the weights placed at the center of the sensor, resting directly on the flexures. The data recorded then lead to a calibration matrix to adjust the NASA-4 data so that it could be processed and analyzed [2].

4.2 Techniques of Data Analysis

4.2.1 Metrics of Data Analysis

Various methods may be applied to the sampled set of data produced by the EDLS spaceflight experiment. The method or methods applied to the data are determined by the nature of information desired from the analysis. Common metrics applied to force-moment data are further described, along with the basic information that is typically extracted from each method.

4.2.1.1 FORCE/MOMENT VERSUS TIME

This is the most basic of all plots, where each given orthogonal axis force or moment axis trace is plotted with respect to time. This metric is most useful for gaining insight into the actual characteristic shape of the motion, and can be used to identify further similar

motions. A peak force or moment function can also be used to extract maxima or minima from the trace, and an arithmetic average function can be used to find a general level of force or moment exerted during a motion.

4.2.1.2 VECTOR VERSUS SINGLE AXES

In some cases, one may be interested in force or moment data from an individual axis. There may be a high degree of symmetry in the nature of the motion that make a single axis force predominate the character of the motion. The common method of processing to be applied to multidimensional (two or three axes) force sensors is to combine the individual orthogonal axis data into a vector magnitude. The vector magnitude of an individual data point is derived by the following equation:

$$\|V_j\| = \sqrt{X_j^2 + Y_j^2 + Z_j^2} \tag{4.1}$$

4.2.1.3 ARITHMETIC MEAN AND ROOT-MEAN-SQUARE (RMS) VERSUS TIME

By choosing a small interval of time relative to the sampling rate and the total time of the acquired data, an arithmetic mean or root-mean-square (RMS) calculation may be applied to the interval. Typically, the interval ranges from several seconds to a few minutes, depending of the sample rate of the data. By applying an arithmetic mean to the data within the time interval results in a total set of data with a frequency response less than the inverse of the time interval. An average plot may be produced by calculating an interval average of each axis and then combining the results into a vector magnitude representation. By applying an RMS calculation to the interval of data, information relative to the periodic content of the data is apparent. An RMS plot may be produced by calculating the RMS of an interval of data for each axis then combining the results into a vector magnitude representation.

4.2.1.4 POWER SPECTRAL DENSITY VERSUS FREQUENCY

The power spectral density of a signal illustrates where the energy content of the total signal resides. This is especially useful in determining the frequency beneath which most of the energy content of an event is bounded. A fast-Fourier-transform routine is applied to a window of force or moment versus time data. This transforms the time-sampled data into the frequency domain. Once the data has been transformed into the frequency domain, it is possible to estimate the peak PSD value and the frequency below which a certain percentage of the power is contained. Normally, a default value of 95% (approximately 3 standard deviations) is taken as the bounding value. As well, a corner frequency above which the power density of the signal is to be ignored can be specified, thus, eliminating the noise content of the signal [2].

4.2.1.5 POWER SPECTRAL DENSITY VERSUS TIME VERSUS FREQUENCY

Calculating successive power spectral densities of either the force or moment data, and concatenating them in time results in a three-dimensional plot of the force or moment data, for complex motions of lengthy duration. Activities that contain certain distinct frequencies then become apparent by horizontal bands or bars in the graph. This technique is useful for comparing several motions of the same type, and can thereby lead to an extraction of the signature power spectral density of the generalized motion. This can lead to the identification of this motion in further processed data, where video footage of the event is not available.

As a caveat, it should be noted that one cannot prepare a comparison of a PSD plot from a period of time from one mission with a period of time from either the same or a different mission. Such a comparison is not reasonable to perform by using the standard PSD plot because the microgravity acceleration environment on Mir is very dynamic. Thus, comparison of long-duration PSD plots is hindered by the non-stationary nature of

the acceleration environment. Spectral averaging techniques intended to suppress spurious peaks and accentuate significant spectral contributions obscure the spectrum where brief, transitory contributions occur (see Appendix C).

4.3 Data Correlation and the Space Acceleration Measurement System

The NASA Lewis Research Center (LeRC) manages several accelerometer projects for measuring the microgravity environment on board the NASA Shuttle missions and the Russian Space Station Mir. The LeRC accelerometers currently operating on Orbiter missions are the Space Acceleration Measurement System (SAMS) and the Orbital Acceleration Research Experiment (OARE) instrument. In 1994, a SAMS unit consisting of several accelerometer heads was installed on the Russian Space Station Mir to support U.S. and Russian microgravity experiments by measuring the microgravity environment during experiment operations. The SAMS measures the vibratory and transient environment from 0.01 Hz up to 100 Hz with a set of three distributed triaxial sensor heads [18].

4.3.1 Acceleration Data Measurement

The SAMS Triaxial Sensor Heads (TSHs) are mounted to a structure near an experiment in a predetermined manner. The orientation of the TSH axes relative to the vehicle is measured and must be recorded for later use in analyzing and correlating the acceleration data. In this particular case, the SAMS accelerations are correlated with the force and moment measurements recorded during the EDLS experiment. Using this information, the measured acceleration levels may be transformed to other orientations, such as an experiment-based coordinate system or, barring that, the Mir coordinate system.
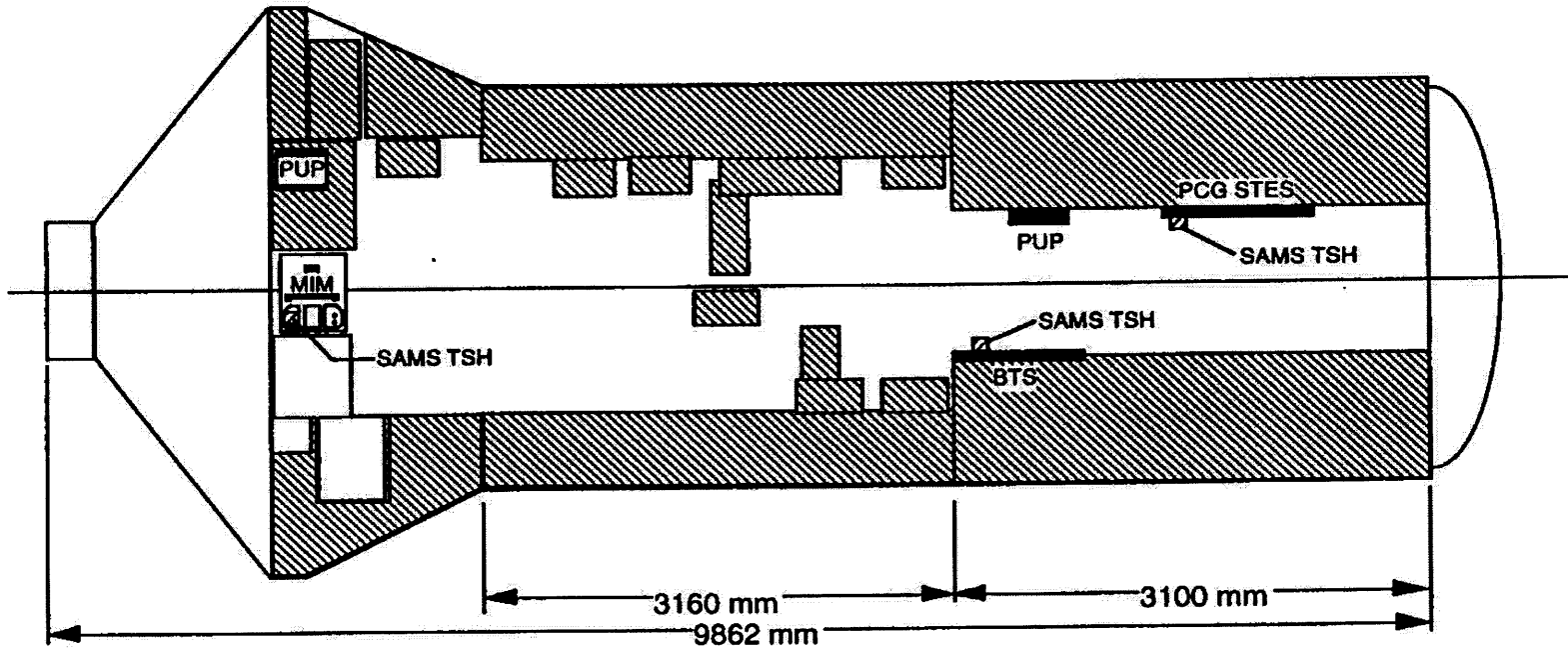
Priroda Module Configuration

Figure 4.2: Placement of SAMS in Priroda Module [20]

The determination of SAMS sensor head locations and orientations is made from a number of sources. Oftentimes, the dates are contradictory, especially when the sources refer to a planned move of SAMS, without verification that the move actually occurred. Ultimately, it is possible that the mounting of the sensor heads was not performed according to plan. So far, the tentatively reported orientation of the sensor heads is as follows (Table 4.1):

Table 4.1: Compilation of SAMS Sensor Head Locations during NASA-4 [57]

Date	DMT 1996 Day	Module	TSH A	TSH B
1 January 1997	001	Priroda	MIM $X_{(h,a)} = -Y_{Priroda}$ $Y_{(h,a)} = X_{Priroda}$ $Z_{(h,a)} = Z_{Priroda}$	MGBX $X_{(h,b)} = Y_{Priroda}$ $Y_{(h,b)} = -X_{Priroda}$ $Z_{(h,b)} = Z_{Priroda}$
31 January 1997	031	Priroda	MIM $X_{(h,a)} = Z_{Priroda}$ $Y_{(h,a)} = X_{Priroda}$ $Z_{(h,a)} = Y_{Priroda}$	MGBX $X_{(h,b)} = Y_{Priroda}$ $Y_{(h,b)} = -X_{Priroda}$ $Z_{(h,b)} = Z_{Priroda}$

4.3.2 Data Correlation Techniques between EDLS and SAMS

The greatest difficulty arising in the process of correlating results from two different experiments is the issue of time synchronicity. There has been a need for a simple, integrated characterization of a mission, carrier, time period etc. in order to compare this with another mission, carrier, time period, etc., to affect the comparison and correlation of data. An approach used to address this quandary of time synchronization has been found by using the Principal Component Spectral Analysis (PCSA) and the Quasi-steady Three-dimensional Histogram (QTH) techniques. The PCSA plot technique is based on the frequency distribution of the vibrational energy and is normally used for an acceleration data set containing frequencies above the lowest natural frequencies of the vehicle. This technique is particularly applicable to the data collected from the SAMS experiment. The

QTH plot technique is based on the direction and magnitude of the acceleration and is normally used for acceleration data sets with frequency content less than 0.1 Hz, and is primarily used for the correlation of the OARE data. The PCSA and QTH techniques bring both the range and median of the microgravity environment into a single graphical context for an entire mission time [57].

A study of the exact nature of the technique used to correlate the SAMS data to a given accelatory event aboard the Russian Space Station Mir, is helpful to interpret the precision and accuracy of all correlated measurements. The source of microgravity acceleration data for a PCSA plot is a sampled data set produced by, in this case, the SAMS system. The time frame to be analyzed is divided into equal duration time intervals. The duration of the interval is chosen based upon the desired frequency resolution, given by:

$$\Delta f = \frac{1}{\Delta t_i} \tag{4.2}$$

The Power Spectral Density (PSD) is then computed for each interval. The significant spectral peaks in each of the PSD's from all of the successive time intervals are then extracted. For the purpose of the SAMS data, a significant spectral peak is defined to be a PSD magnitude value that is a local maximum that is at least as high as any other magnitude point within a specified frequency range. The frequency range is usually specified by a number of frequency resolution intervals (a neighborhood) on either side of a data point. Typical values for a neighborhood were 0.05 to 0.1 Hz. A cutoff frequency of 25 Hz is employed for motions aboard a large vehicle in microgravity, as most disturbances above this frequency usually occur due to mechanical components onboard the space station [26].
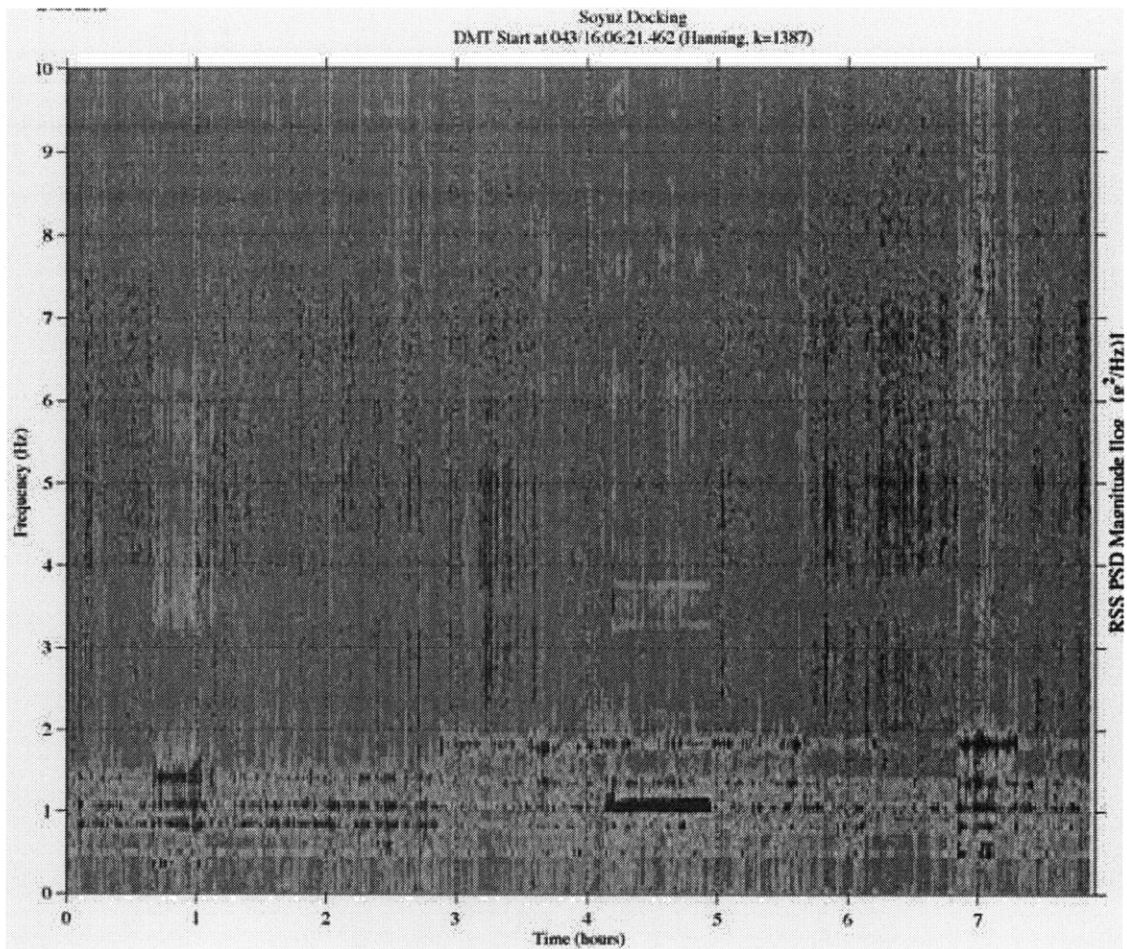
Figure 4.3: PCSA Plot from SAMS Data [57]

An individual set of significant spectral peak points extracted from a PSD indicate the upper levels of the microgravity environment for the time period of that particular PSD. This upper level of the microgravity environment acts as a broad gauge of the maximum effects of the acceleration due to an event. It should be noted that this technique is not suited for events that create acceleration levels in very narrow frequency bands, in this case, data calculated from the root-mean-square levels of acceleration are preferable. However, correlation of PCSA plots to known mission events has led to a method to relate characteristics of a PCSA plot with mission activities and vehicle equipment operation [57].

Thus, a viable method for synchronizing the time of an event from video footage with data from both the EDLS and SAMS experiments has been advanced. Now, the next concern was rendering the data collected from the EDLS experiment into a format easily manipulated by data analysis software.

4.4 EDLS Data Processing Software

The raw data files written by the data acquisition system from the EDLS experiment were not of a format easily read by standard analysis software, and thus a data processing and analysis software package, entitled Enhanced Dynamic Load Sensors Application Package (EDLSAP) was created [2]. The program was written in MATLAB code, and can convert the raw data into processed MATLAB data, which can then be displayed in many forms, thus enhancing the understanding of the motions.

4.4.1 Processing

All raw data files from the NASA-4 mission were batch-processed with EDLSAP. EDLSAP provides the capability to convert files manually (i.e., one file at a time) or automatically by reading in a "batch file", that is, a text file, and converting a number of files in a row. Since most raw data files were very large and include hours of data, the processed data files were limited in size to 5 minutes of data. After processing, there were 42 MATLAB data files, each holding 5 minutes of EDLS data (excepting the leading or trailing files which may be shorter). The 5-minute length was selected based on the capability of the computers to process the raw data and to display and edit the processed data [2].

4.4.2 Editing and Analysis

EDLSAP makes it easy to edit the processed data. Data segments, such as noise, can be removed from the data by cutting out unwanted portions. The signal can be unbiased, so that when no load is applied the average signal is zero. The data can also be scaled (i.e.,

multiplied by an arbitrary factor) and filtered with a low-pass digital elliptic filter (with a variable number of poles and a corner frequency) [2]. Once a specific event has been located, EDLSAP can illustrate the force vector through a 3-D animation. EDLSAP also includes several elementary statistical functions, such as an average function, a maximum function and a power spectral density function.

4.5 Elementary Data Analysis

In the analysis of the NASA-4 data, the main parameters of interest for a recorded motion were the maximum force, the root-mean-square force and the power spectral density of the motion. After the EDLS data was parsed into 5 minute files, the next phase of the data reduction involved visually inspecting the force and moment traces for every file. Each five minute file of data had three sensor components[1] for a total of 15 force and moment traces. Then, for each force or moment trace which was not Gaussian white noise, the pertinent motion was then identified, both from the generalized force traces and from the video log, and used to create a database of motions. After this motion database was compiled, the necessary statistics were extracted, and statistical analysis could be carried out. Only the EDLS data from the NASA-4 mission has been fully analyzed, and analysis of the NASA-2 mission data has only been cursory due to experimental procedural errors in recording.

4.5.1 Motion Extraction

The enormous amount of data collected from the NASA-4 mission (1024 MByte) due to a low threshold setting on the sensors necessitated the manual culling of the data, to approach manageable levels for analysis purposes. Each file was reviewed manually, and discernible motions were extracted using EDLSAP. The extracted motions were renamed

---

1. Configurations are either Footloop-Footloop-Touchpad (FFT) or Footloop-Handhold-Touchpad (FHT)

with the name corresponding to the starting time of the motion.
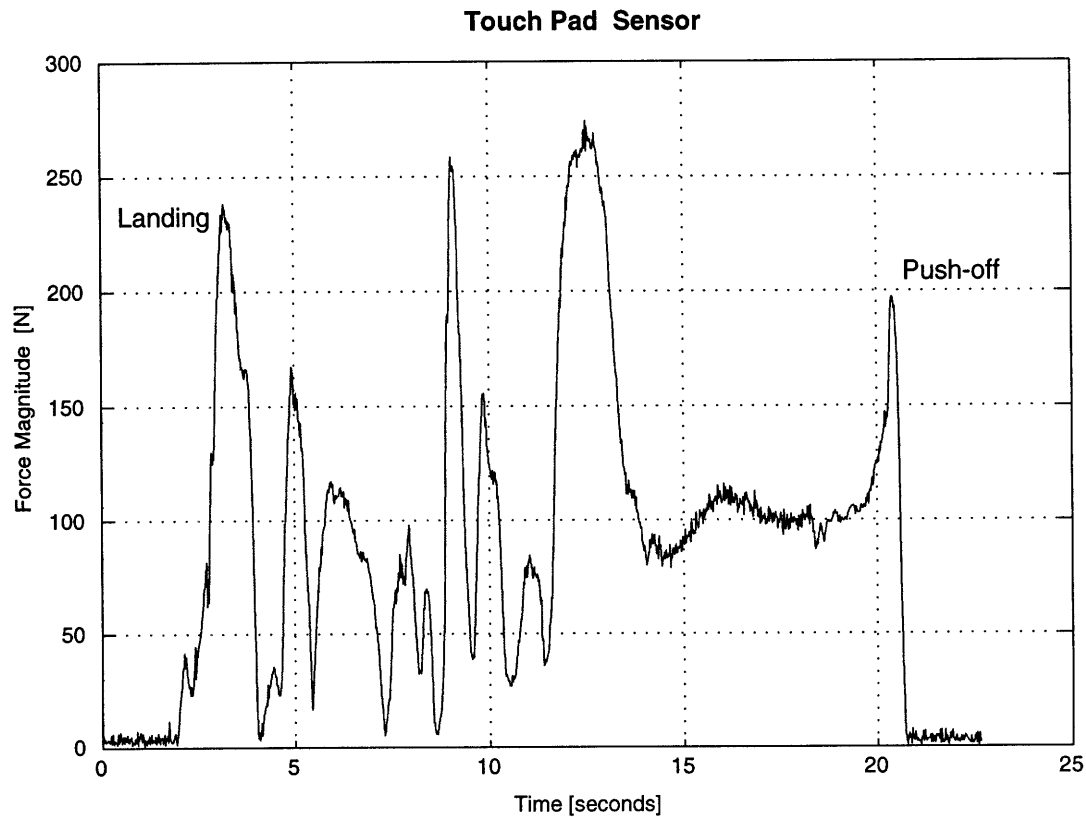
Figure 4.4: Concatenated Landing and Pushoff Motion

An attempt was made, wherever possible, when events occurred on more than one sensor, that the entire timespan of the event was processed and thus the event comprised the force traces of all of the sensors involved (Fig 4.4). For instance, if the astronaut were to land on both footloops, with a slight time delay between the touchdown of one foot on one of the sensors, the event was processed in such a way as to incorporate both motions into one data file. If a motion were to span a length greater than a file, an EDLSAP-related subroutine enabled the motion to be concatenated into its entirety. This technique, which certainly made for a more accurate force or moment trace of the motion of the astronaut, especially in conjunction with the video footage of the events, later caused problems in the power spectral density analysis, as will be discussed in the next section.

A spreadsheet was prepared, which noted all the necessary attributes of each and every motion. Parameters such as start time, motion duration, pertinent sensors, active or passive operating session, and sensor configuration were all recorded in the spreadsheet, as well as any pertinent comments that seemed necessary to the interpretation of the motion. A summary of these spreadsheets can be found in Appendix B.

4.5.2 Data Extraction

Once the painstaking process of compiling a manual database of event motions had been finalized, and the spreadsheet of motion events had been prepared, the next step was the extraction of the characteristic motion metrics necessary for further analysis. The metrics selected for initial analysis were the aforementioned maximum force of the motion, root-mean-square force of the motion and the power spectral density of the motion.

Now, given that there were initially 1440 motions identified in the spreadsheet, the task of manually extracting the metrics for the motions was completely untenable. Thus, a further MATLAB script was written. The script loaded the force data for the motion, identified the maximum force, root-mean-square force and power spectral density for the motion, then outputted the results to a separate data file. This data file could then be imported into Microsoft Excel, for further analysis.

During the course of extracting these pertinent metrics, a problem with the power spectral density manifested itself. Due to the algorithm used to compile the motions, portions of signal noise were incorporated into the motion profile if an event on one sensor overlapped that of another sensor. This white noise drastically altered the power spectral density of the motion, driving it toward the corner round-off frequency of 30 Hz. A feasible way to extract the actual power spectral density of the force profile of the motion without loosing the overall multi-sensor scope of the motion has not yet become apparent, thus, many of the motions became unusable for PSD calculations (See Appendix C).
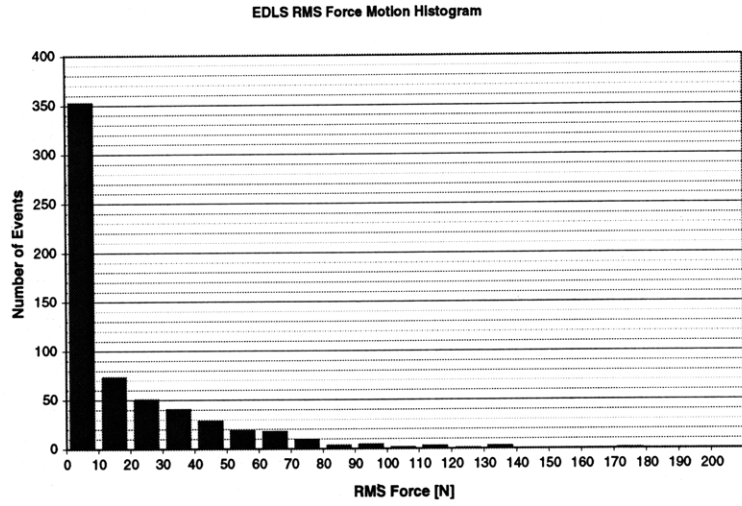
Several other factors, such as duration of the motion, disconnection of sensors, and improper biasing and calibration of the sensors conspired to render many other motions unusable, resulting in a final database of 614 motions.

4.5.3 Results

Based on the analysis of the 614 usable motions, utilizing the metrics of maximum force, root-mean-square force and power spectral density, several elementary conclusions can be drawn. Approximately three standard deviations, that is, about 95% of all data points, of the maximum force data for all motions lie below 275 N. Similarly, three standard deviations of all root-mean-square forces for all motions lie below 60 N. As well, three standard deviations of the 95% power spectral density data lies below 22 Hz.

It can be seen that the majority (63% or approximately one standard deviation) of the maximum force data lies below 75 N, and that 69% of the root-mean-square force data lies below 20 N. This differs greatly from the very high force data observed aboard the Skylab experiments. This could be due, in fact, to the tremendous adaptive ability that the astronauts possess while in a microgravity environment for a prolonged period of time. According to the literature, after a period of approximately 30 days in microgravity, the astronaut becomes extremely attuned to his environment, and can judge what finely measured forces are necessary to affect a change in motion.

This is also evidenced by the fact that 65% (approximately one standard deviation) of all 95% power spectral density results are below 3 Hz. Hence, the astronaut can be likened to a consummate ballerina in space, capable of exerting incredible precision and control of the power and forces he/she uses for motions in the weightless environment of space.

EDLS RMS Force Motion Histogram

Frequency Below which 95% of the Power is Contained

EDLS Max Force Histogram
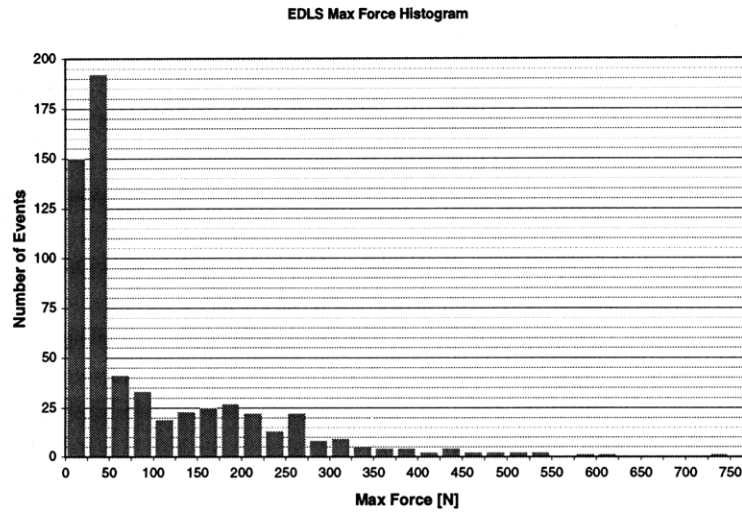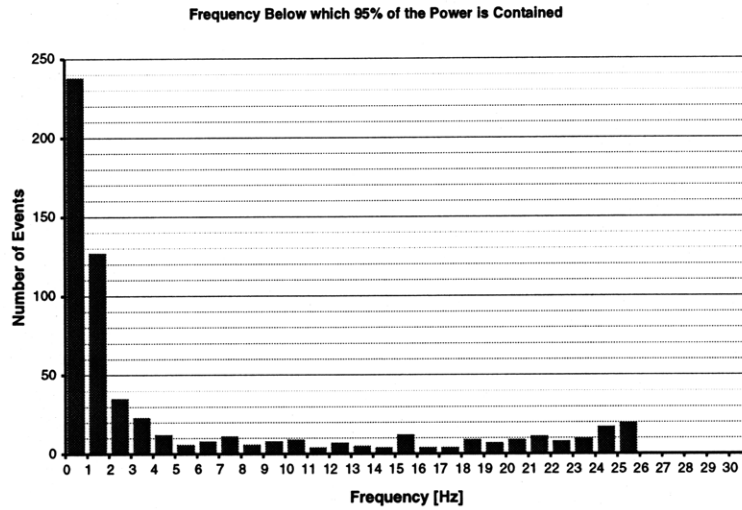
Figure 4.5: Histograms (a) RMS Force (b) Maximum Force (c) 95% PSD

4.5.4 Correlated Results

With the flight of EDLS on NASA-2 and NASA-4, video footage of the passive and active operation sessions was requested, allowing for direct correlation of occasional video footage to actual motion traces in the data. Table 4.2 summarizes all the instances where this direct video correlation was possible:

Table 4.2: Table of Video Correlated Motions

Motion	Video File	Video Date	Video Time	Data File
Landing	Twist_Landing_4.mov	March 13 1997	10:19	072_10_19_15.mat
Landing	Twist_Landing_5.mov	March 27 1997	2:45	086_17_45_04.mat
Landing	Twist_Landing_1.mov	May 9 1997	8:41	129_11_41_08.mat
Landing	Twist_Landing_2.mov	May 9 1997	9:01	129_12_00_49.mat
Landing	Twist_Landing_3.mov	May 9 1997	9:15	129_12_15_04.mat
Pushoff	Push_Off_4.mov	March 12 1997	11:19	071_11_15_31.mat
Pushoff	Push_Off_5.mov	March 13 1997	10:39	072_10_38_51.mat
Pushoff	Push_Off_6.mov	March 13 1997	11:39	072_11_37_11.mat
Pushoff	Push_Off_7.mov	March 27 1997	2:17	086_17_14_59.mat
Pushoff	Push_Off_8.mov	March 27 1997	2:26	086_17_25_04.mat
Pushoff	Push_Off_9.mov	March 27 1997	2:45	086_17_45_04.mat
Pushoff	Push_Off_1.mov	May 9 1997	8:38	129_11_37_11.mat
Pushoff	Push_Off_2.mov	May 9 1997	8:55	129_11_54_50.mat
Pushoff	Push_Off_3.mov	May 9 1997	9:15	129_12_15_04.mat

A trend can be noticed for motions where there is correlated video data. For pushoff motions, performed early in the mission (March 12), the maximum force exerted to perform the motion is approximately 15% higher than the maximum force exerted to perform the same motion later in the mission (May 9). This general trend can also be observed in the landing motion as well. This would seem to support the hypothesis that astronauts

seem to adapt to the microgravity environment with time, altering their control strategies for performing generic motions. This has far reaching ramifications for the adaptive strategies used by astronauts on long term missions. However, more in depth research should be conducted before any firm conclusions can be made.
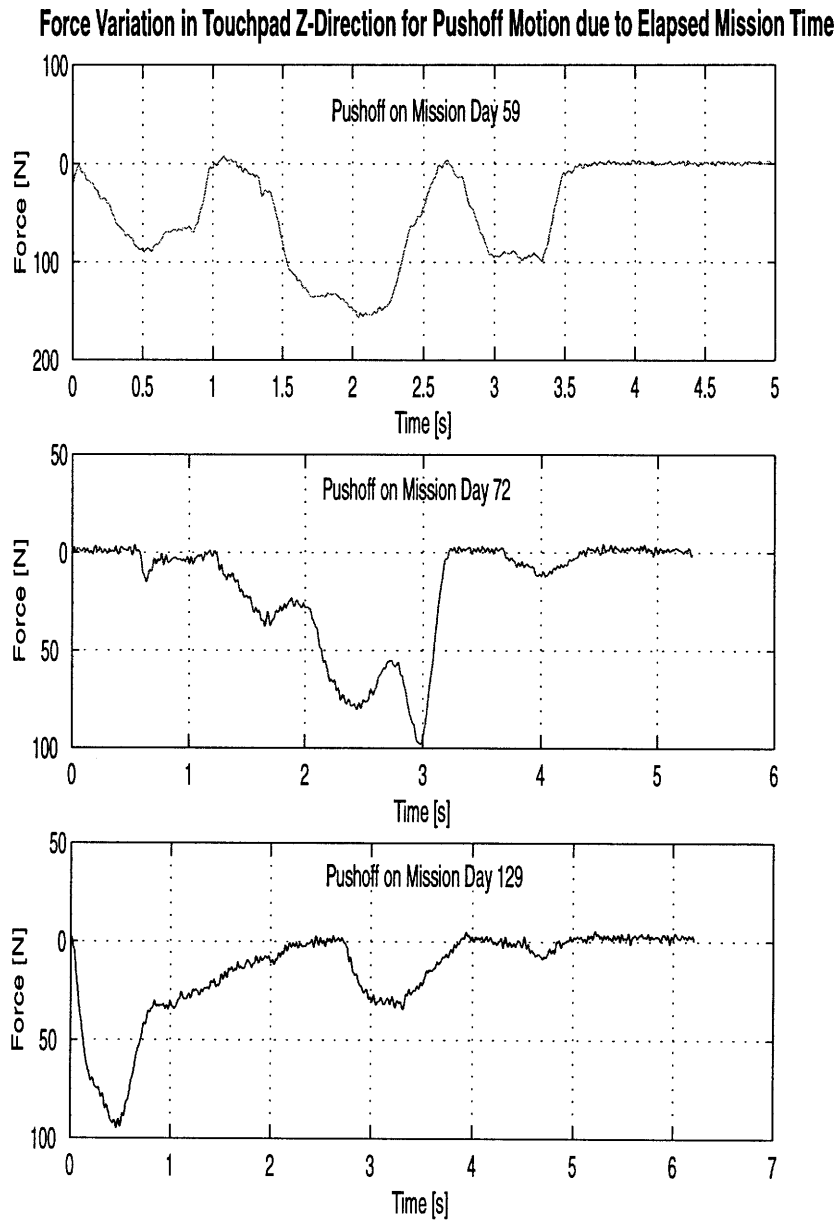
Figure 4.6: Pushoff (a) Early (b) Middle and (c) Late in the Mission

The primary statistics of the data have been determined at this point, and a general picture of the maximum force profiles, root-mean-square force profiles and power spectral density profiles of the data has been created. As well, force and acceleration data for specific motions from the EDLS and SAMS experiments, respectively, were correlated. Hence, we can now turn the focus of the remaining chapters of the thesis towards the problem of transfer function determination from this correlated force-acceleration data.

Chapter 5

Transfer Function Analysis

As of yet, no analysis of forces due to astronaut motion aboard the Russian Space Station Mir has ever been coupled with acceleration data from the aforesaid station in order to derive a transfer function. This thesis will make the first attempt to develop a transfer function between the forces exerted by astronauts onboard the station and the overall acceleration of the space station. This means the flexible dynamics of the Russian Space Station Mir under the influence of internal astronaut forces will have to be analyzed.

From a dynamical systems perspective, determining the flexible dynamics of a space station may be seen as a linear system identification problem [10]. Input signals and outputs must be measured and available for identification purposes. Both are presumably corrupted by noise arising from unidentified sources that may include motor vibrations, thruster control firing and robotic control influences. Such noise may arise both as process or sensor noise. A process noise is a Gaussian noise introduced into the process to be measured, normally by a disturbance. A sensor noise arises in the measurement capability of the sensor, acting to distort the true value of the signal to be measured. At steady-state operating conditions, a generalized space station is modelled, in this chapter, as a linear, time-invariant system. For such a system, several identification procedures are available. In particular, spectral estimation techniques with or without time and frequency windowing are very robust identification procedures [84]. If enough data is produced, Welsh's averaged periodograms eventually converge to good transfer function estimates. Other popular identification techniques include the prediction error method, which appears to be very thorough. Recent and useful additions to these include the subspace identification

technique which use time-domain input-output data. Subspace identification techniques have recently been extended to handle frequency-domain data as well [8].

With the exception of Fourier analysis, all the methods just mentioned are black-box identification techniques, whose convergence properties have been demonstrated for specific noise categories. However, for a structure as complicated as a space station, the input (force) and output (acceleration) data is expected to be rather noisy, and the noise characteristics are neither well known nor necessarily stationary. Fourier analysis may be used to cross-check the results of these other methods, but also tends to be sensitive to the high levels of noise encountered. Time-frequency analysis thus is the most reliable technique for the uncertainties presented by this complex problem, and will be employed [84].

5.1 Time-Frequency Analysis of Signals

5.1.1 Fourier Analysis

Since the EDLS and SAMS data can be considered to be derived from a sampled data system, all signals are supposed to last from $-\infty \leq t \leq \infty$, taking nonzero values only in the interval [0,T], which corresponds to the duration of the data sample. Define the sampling time ΔT and let N be the smallest positive integer such that $N\Delta T \geq T$. Given a signal $u(t)$, $-\infty \leq t \leq \infty$, the sampled signal will be noted:

$$u_n = u(n\Delta T) \tag{5.1}$$

where n is any unsigned integer. The most common representation of u is its discrete Fourier Transform (DFT):

$$\hat{u}(j\omega) = \sum_{n=-\infty}^{\infty} u_n e^{-j\omega n\Delta T} \tag{5.2}$$

$$\hat{u}(j\omega) = \sum_{n=0}^{N} u_i e^{-j\omega n\Delta T} \tag{5.3}$$

where ω is a real number. The discrete Fourier transform is very useful because it allows

87

for the observation of the frequency content of the signal u.
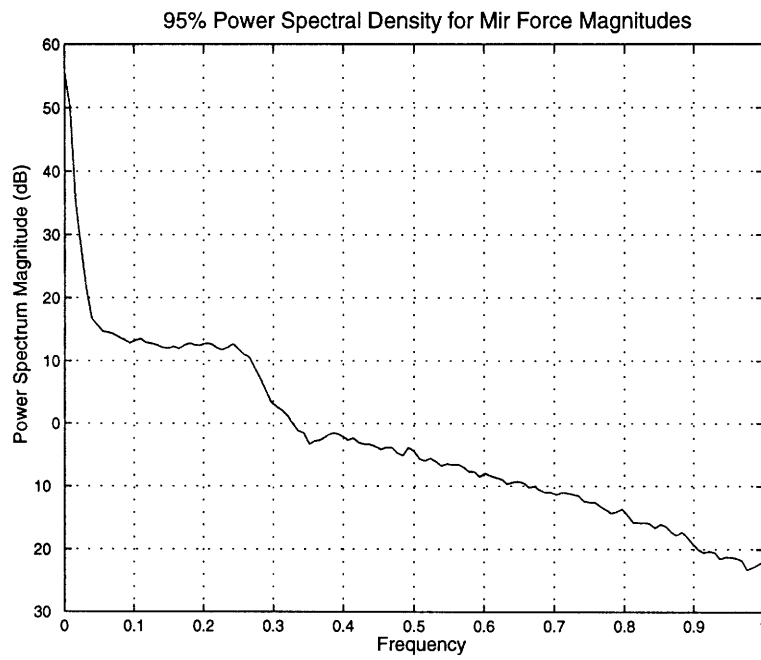
(a)
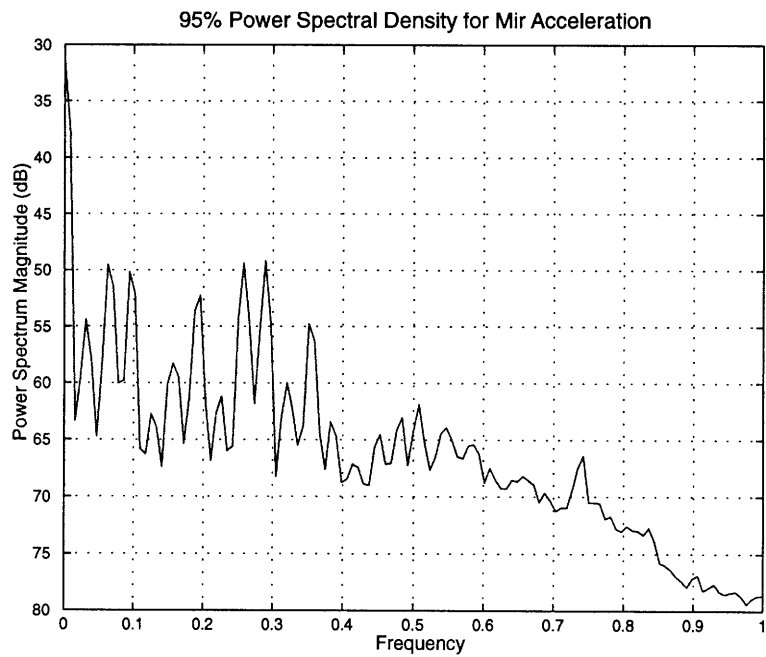
(b)

Figure 5.1: (a) EDLS Force PSD (b) SAMS Acceleration PSD

Figures 5.1 (a) and 5.1 (b) show the time representation and power spectral densities of typical input and output signals for the Russian Space Station Mir under the astronaut landing motion and the Priroda module's acceleration. A considerable quantity of information is available from both signal representations; in particular, the power spectral density of the input shows resonances close to 0-0.1 Hz, and the power spectral density of the output shows resonances close to 0.2-0.3 Hz, although these are not necessarily easy to determine in the latter case because of the presence of high levels of noise. Specific techniques such as signal windowing contribute to smoother transfer functions. However, they also tend to decrease frequency resolution and to distort frequency estimates (see Appendix C).

5.1.2 Time Frequency Analysis of Signals

Although the frequency representation $\hat{u}$ is very useful and computationally easy to handle, it does not easily represent signals whose spectral characteristics evolve with time. A model for astronaut motion signals is postulated:

$$u(t) = A\cos[(\dot{\omega}_0 t + \omega_0)t + \phi] \qquad (5.4)$$

This is typically the case with random astronaut motions, which do not yield the same characteristic trace each time.

This lack of repeatability of the motion signal may lead to many lost opportunities for study if the signal is polluted by broadband noise. Therefore time-frequency representations of signals are introduced: given a passband filter template b with discrete-time transfer $\hat{b}$, we define the family of passband filters b_{ω_0} as:

$$\hat{b}_{\omega_0}(\omega) = \hat{b}(\omega - \omega_0) \qquad (5.5)$$

Let us define the time frequency representation, TF, of any signal u:

$$TF(u, \omega_0, p) = \sum_{n=-\infty}^{\infty} u_n b_{\omega_0, p-n} \qquad (5.6)$$

This transformation, *TF*, maps one-dimensional signals to two-dimensional pictures indexed by time $(p\Delta T)$ and frequency ω_0. This transform is not necessarily invertible, although it is linear. The transform may be seen as filtering the initial signal through a filter bank parameterized by ω_0. This transform is similar to the short-time Fourier transform[1]. The short time Fourier transform first truncates the signal in possibly overlapping windows and then performs a Fourier analysis of the truncated signals, thus resulting in another time-frequency analysis of the signal [8]. However, there are many detrimental side effects to arbitrary truncation. The most well know of these is that of arbitrarily decreased frequency resolution, as well as leveling of resonant peaks (Fig. 5.2). The transform *TF* does NOT truncate signals *a priori* (see Appendix C).
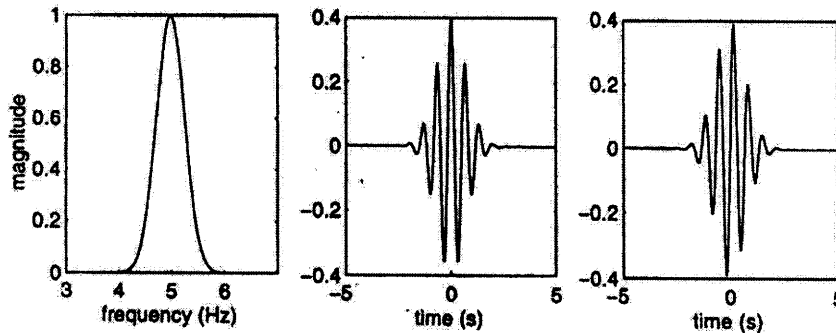
Figure 5.2: Transformation with Arbitrary Truncation

In order to divide the input and output data up into time windows which will then be transformed into the frequency domain, and given the assumed sinusoidal behavior of the signals involved, we have chosen the following the windowing/filtering function:

$$\hat{b}(\omega) = e^{-\lambda\omega^2} \tag{5.7}$$

By adjusting both parameters, λ and ω_0, it is possible to generate a family of passband filters with arbitrary central frequency ω_0 and bandwidth B, given by:

---

1. Implemented as the Specgram Function in the signal processing toolbox of Matlab[TM]

90

$$B = \sqrt{\frac{\log(2)}{(2\lambda)}}$$ (5.8)

Traditionally, the scaling factor λ is used primarily to obtain multi-resolution information across frequencies such that every decade of the spectrum is covered equally. However, in the context of structural analysis, it is usually found that λ is kept constant and ω_0 is varied, thus emphasizing the linear scaling of the frequency axis, better suited to structural analysis [48].

Utilizing this technique, the EDLS force data and the SAMS acceleration data can be transformed into the frequency domain without incurring any loss of information inherent in the signal. Thus, the first major step towards deriving a transfer function has been accomplished.

5.1.3 Transfer Function Estimation Using Time Frequency Analysis

The time-frequency analysis procedure described previously suggests the following three-step transfer function identification process [29]:

1. Perform the time-frequency analysis of the EDLS force input signal and the SAMS acceleration output signal.
2. For each frequency of interest, remove the noisy parts of the time-frequency representations using the appropriate filtering algorithm
3. Obtain estimates of the frequency response using the de-noised time-frequency representations of the signals

Thus, for our general case, if we wish to identify the transfer function from a multi-input system (i.e., more than one EDLS force sensor) to a given output (SAMS accelerometer measurement), the preceding procedure is utilized. This process is best illustrated in Figure 5.3.
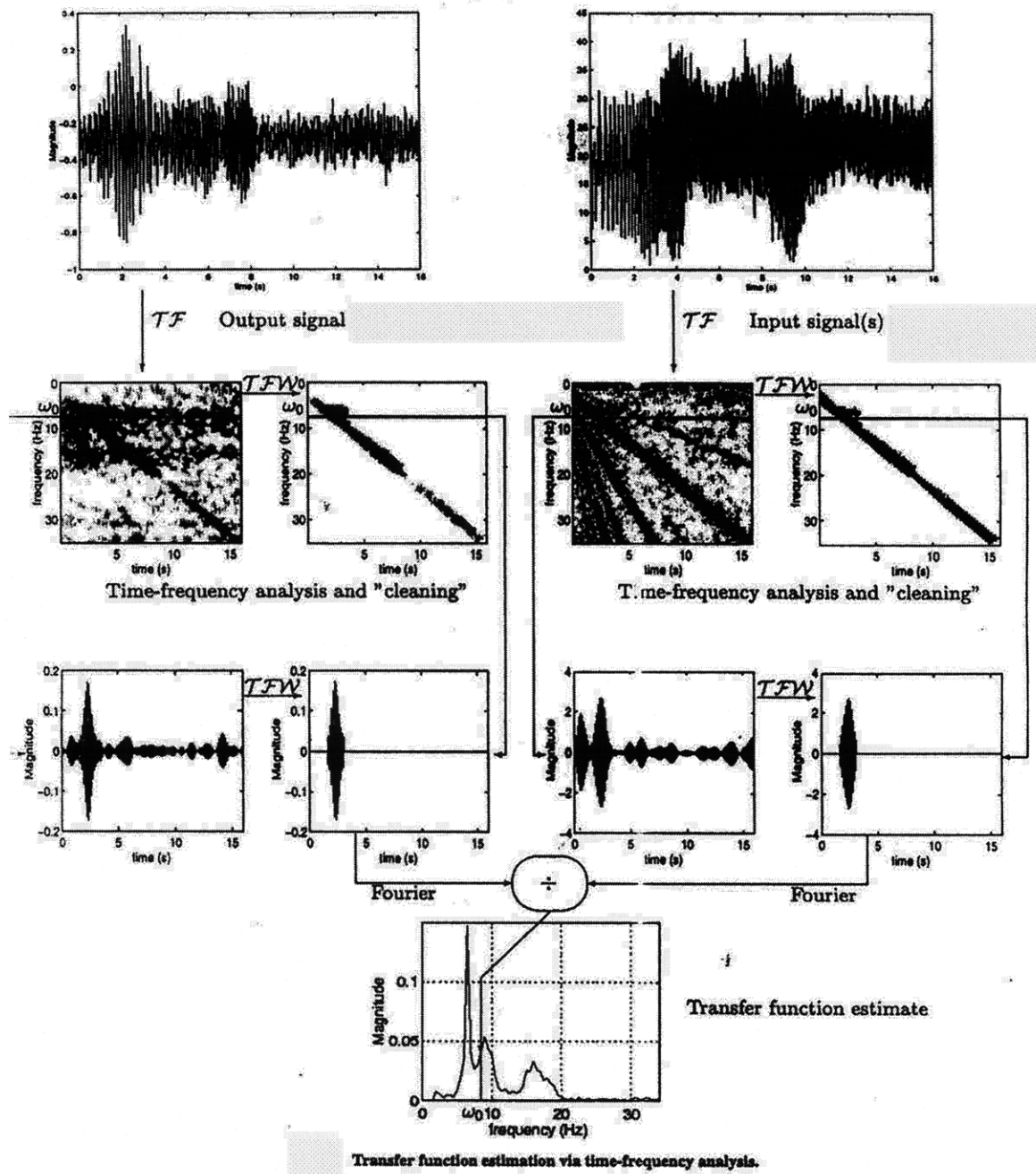
Figure 5.3: Three Step Transfer Determination Process [29]

Consider the case of a system with m inputs $u_1, u_2, ..., u_m$ and one output y. Assuming the dynamical system to be linear, there exist linear, single-input/single-output operators $h_1, h_2, ..., h_m$ such that:

$$y = h_1 \otimes u_1 + h_2 \otimes u_2 + \ldots + h_m \otimes u_m \tag{5.9}$$

where the operator $h \otimes u$ represents the convolution between the functions h and u.

The goal of transfer function estimation is to obtain approximations for $h_1, h_2, \ldots, h_m$. From equation 5.6 we have:

$$TF(y, \omega) = b_\omega \otimes y \tag{5.10}$$

and

$$TF(u_i, \omega) = b_\omega \otimes u_i \tag{5.11}$$

where $i = 1, 2, \ldots, m$.

Consequently we have:

$$TF(y, \omega) = \sum_{i=1}^{m} TF(h_i \otimes u_i, \omega) \tag{5.12}$$

$$TF(y, \omega) = \sum_{i=1}^{m} b_\omega \otimes (h_i \otimes u_i) \tag{5.13}$$

$$TF(y, \omega) = \sum_{i=1}^{m} h_i \otimes (b_\omega \otimes u_i) \tag{5.14}$$

$$TF(y, \omega) = \sum_{i=1}^{m} h_i \otimes TF(u_i) \tag{5.15}$$

Hence, the transformation TF leaves the input-output relation invariant, and the transfer functions $h_1, h_2, \ldots, h_m$ may be identified from the transformed inputs and outputs as well [29].

5.1.4 Noise Removal

The procedure for deciding what qualifies as the useful part of both input and output signals, based on their time-frequency representation, is very much at the discretion of the analyst. Selecting the appropriate filter to remove the noise occurs very much through trial and error, and is an extremely complex process, involving many data set calculations.

The de-noising procedure uses the full time-frequency representation of the signal $TF(u)$ and amounts to setting to zero any element of $TF(u)$ that appears to represent more noise than actual information. Thus, the noise removal procedure is manual in nature, and is a time- and frequency-dependent thresholding technique that takes into account the particular structure of the signal. Let us denote this operation as $TFW(u)$. For a particular frequency ω_0, $TFW(u, \omega_0)$ thus represents the original signal, filtered through the bandpass filter b_{ω_0}, and then time-windowed. It has been found experimentally that identical time-windowing of input and outputs yields the best eventual results.

Since white noise is defined to be a stationary random process having a constant spectral density function, it appears as a simple bias in the data in the frequency domain, and is easily removed. The noise introduced due to measurement error is much more difficult to determine, and a general signal-to-noise ratio of approximately 5 is used as a benchmark at low frequencies [8].

5.1.5 Transfer Function Estimation

From the de-noised data, the transfer function estimation procedure is straightforward. Assuming no significant information was lost during the noise removal procedure, equation 5.11 suggests that estimates $\bar{h}_1, \bar{h}_2, ... \bar{h}_m$ of the transfer functions $h_1, h_2, ..., h_m$ may be obtained at the frequency ω_0 by solving the equation:

$$TF(y, \omega_0) = \sum_{i=1}^{m} \bar{h}_k \otimes TFW(u_i, \omega_0) \qquad (5.16)$$

Denoting Y as the discrete Fourier Transform of $TFW(y, \omega_0)$ and U_i as the discrete Fourier transform of $TFW(u_i, \omega_0), i = 1, 2, ..., m$, 5.16 can be written in the frequency domain at the frequency ω_0 as:

$$Y(\omega_0) = \sum_{j=1}^{m} \hat{\bar{h}}_i(j\omega) U_i(\omega_0) \qquad (5.17)$$

To obtain these estimates, n independent samples need to be used, with n greater than m. Let Y^i and U_i^j, $i = 1, 2, ..., m$ be the frequency domain outputs and inputs for the jth sample. Using equation 5.16, the estimates $\bar{h}_1(j\omega), \bar{h}_2(j\omega), ...\bar{h}_m(j\omega)$ at the frequency ω_0 satisfy the possibly overdetermined linear system:

$$Ax = b \qquad (5.18)$$

where

$$A = \begin{bmatrix} U_1^1(\omega_0) & ... & U_m^1(\omega_0) \\ ... & ... & ... \\ U_1^n(\omega_0) & ... & U_m^n(\omega_0) \end{bmatrix} \qquad (5.19)$$

$$x = \begin{bmatrix} \hat{\bar{h}}_1(j\omega_0) \\ ... \\ \hat{\bar{h}}_m(j\omega_0) \end{bmatrix} \qquad (5.20)$$

$$b = \begin{bmatrix} Y^1(\omega_0) \\ ... \\ Y^n(\omega_0) \end{bmatrix} \qquad (5.21)$$

Estimates may thus be obtained by solving this system in a least-squares sense:

$$x = A^{\dagger}b \qquad (5.22)$$

where $A^{\dagger}$ is the pseudoinverse of A, in the traditional linear algebra sense for rectangular matrices.

5.2 Experimental Results

With the time averaging analysis of the 614 EDLS astronaut motions, approximately 1.4 GBytes of data were employed in the calculation of the overall force-acceleration transfer function. This provided an adequate database of motions for the determination of the

transfer function. The motions were run sequentially through an averaging program, and then were put through a fine-tuned passband filter which was eventually focused about 0.4 Hz. They were then mapped into the frequency domain using the techniques elaborated upon in Section 5.1.3. The same technique was employed with the SAMS acceleration data, however, a substantial amount of time was spent tweaking the filter in order to get a usable signal. Both sets of data were then de-noised using the above procedure, and then a further windowing method was used to divide the data into uniform samples. In order to arrive at an estimation of the transfer function, the least-squares method is employed to allow for sufficient overlap of the sample windows.
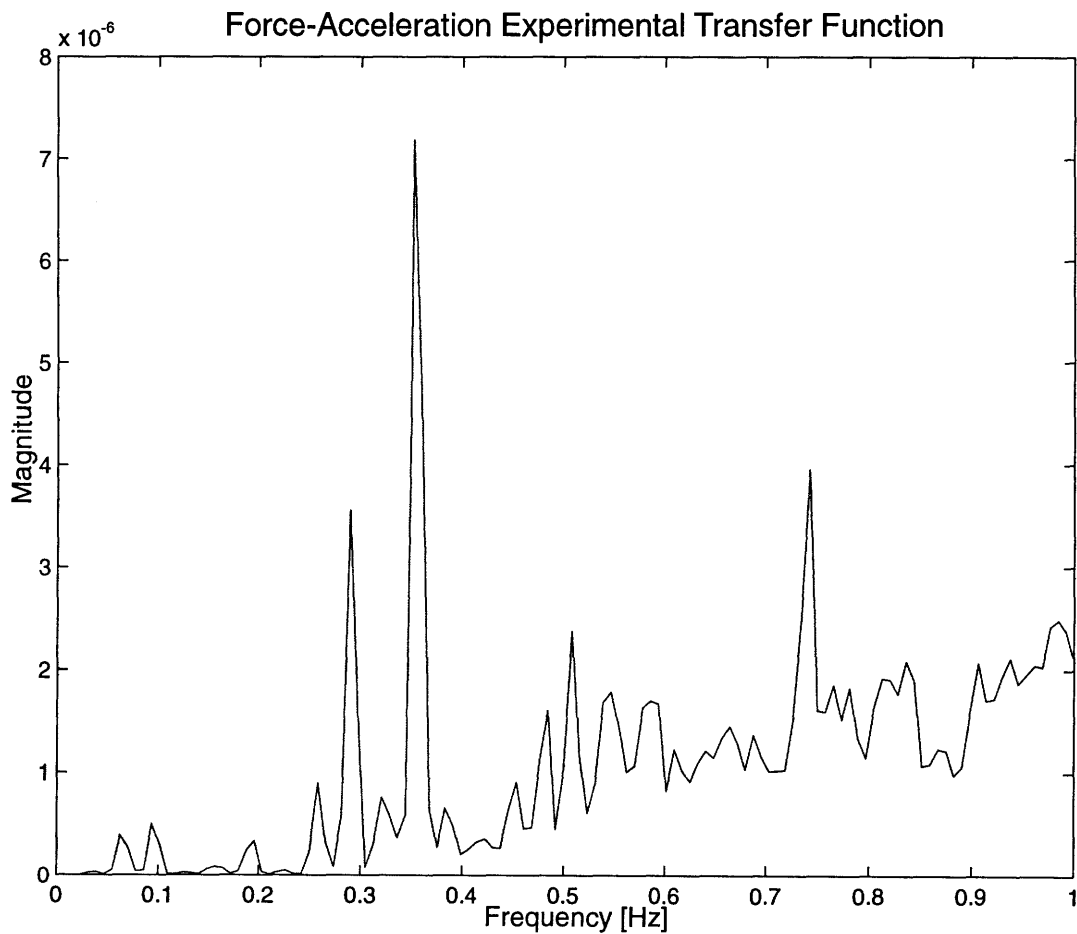
Figure 5.4: Transfer Function for the Russian Space Station Mir

It becomes obvious from the experimental transfer function for the Russian Space Station Mir, that even for large loads, the overall accelerations of the station are small. The magnitude of the transfer function exhibits major poles, that is, poles with high residues, at approximately the following frequencies:

Table 5.1: Poles of Experimental Transfer Function for Mir

Pole Frequency	Peak Magnitude
0.295	3.9×10^{-6}
0.375	7.5×10^{-6}
0.51	2.5×10^{-6}
0.73	4.0×10^{-6}

Furthermore, it can be seen that even the largest of the high residue poles has a magnitude of approximately 7.5×10^{-6} g, at a frequency of 0.375 Hz. Thus, the overall conclusion can be made that nominal astronaut operations are unlikely to disturb the microgravity environment of a space station, or otherwise cause the station to accelerate. Thus, astronaut motions need not be of overly restrictive concern when designing the limits for the structural integrity of a space station.

Chapter 6

Results and Discussion

Having previously derived a theoretical model for a modular space station in Chapter 3, and determined an experimental transfer function for the Russian Space Station Mir from the EDLS and SAMS experimental data, a connection must be made between these two results. The objective of this chapter is to understand how information is stored in a derived model; and how various model elements affect transfer functions; and how various representations of the transfer function are interrelated. The location of the zeroes of a transfer function are investigated, and the effect of output non-transmission is addressed. The implications towards our experimentally determined transfer function are then addressed, and generalizations are made to concerning the effects of astronaut motion on structural design.

6.1 Mathematical Representation of an Experimental Transfer Function

When modelling a high performance structure, such as a space station, two additional factors must be considered beyond the simple structural simplifications (such as the neglect of the effects of damping):

1. The modeller must know enough to actually model the input and output at the preliminary stage, that is, the form of the input (forces) and of the output (accelerations) should be previously established, as is the present case.

2. The model must ultimately capture the input-output transfer function between these two points.

It is obvious that the experimentally determined transfer function from Section 5.2 can be mathematically represented as a function of its poles and zeroes in the form derived in Section 3.5.1:

$$G_{yu}(s) = \frac{y}{u} = \sum_{r=1}^{N} \frac{[C_{yq}]\{\phi_r\}\{\phi^T_r\}[\beta_u]s^2}{m_r(s^2 + \omega^2_r)}$$

(6.1)

Now, if the parameter:

$$T_{yu,r} = \frac{[C_{yq}]\{\phi_r\}\{\phi^T_r\}[\beta_u]}{m_r}$$

(6.2)

is introduced, where T_r is a real number, due to the definitions of the quantities C_{yq}, ϕ_r, β_u, then the transfer function can be expressed much more compactly. Note that the quantity T_r is referred to as the normal modal residue, as it is the residue of the transfer function at the poles $\pm\omega_r$. This residue is the product of two matrices, termed the modal controllability and the modal observability where [10]:

$\{\phi^T_r\}[\beta_u]$ is the modal controllability and

$[C_{yq}]\{\phi_r\}$ is the modal observability

Thus, using the theoretical model for a modular space station in Section 3.5.1, we have established the general mathematical form of the experimental transfer function in Section 5.2. By examining the physical implications of the mathematical form of the experimental transfer function, such as the location of poles and zeroes, insight can be gleaned into the behavior of the Russian Space Station Mir under astronaut loads.

6.2 Poles and Zeroes

The information in the transfer function is stored in the residue and complex poles, or alternatively in the form of model residue, frequency, and possibly damping ratio. The complex pole (or frequency and damping ratio) is a shared and common feature of all pos-

sible representations of the transfer function of the system. This complex pole is relatively easy to interpret as the residue indicates how strongly a mode contributes to a given transfer function. To better illustrate, consider the case of the free-free beam, and truncate the model of the beam at the third natural frequency. The transfer function for a simple three mode undamped system can be written in modal form as:

$$G_{yu}(s) = \frac{T_1}{(s^2 + \omega_1^2)} + \frac{T_2}{(s^2 + \omega_2^2)} + \frac{T_3}{(s^2 + \omega_3^2)} \tag{6.3}$$

Consider the contribution of each mode separately to the transfer function, with $s = j\omega$ and with T_1, T_2 assumed positive, and T_3 assumed negative, for the sake of argument. Figure 6.2 (a) shows the contribution of each mode separately to the transfer function, while in Figure 6.2 (b) the individual contributions have been algebraically summed to generate the graph of the overall transfer function. The transfer function has resonances at the natural frequencies of the individual terms ω_1, ω_2 and ω_3. These are the natural poles of the system. The transfer function then has an anti-resonance at the points where all of the contributions sum to zero. These points are referred to as the zeroes of the system.

In general, there are at least as many poles in a transfer function representation as there are zeroes, although there may be a few zeroes unaccounted for at infinity. This rationale is due to the fact that for a transfer function to have a bounded output, there must exist more poles than zeroes, in order for the magnitude of the bode plot of the transfer function to have a non-positive slope when it terminates [84]. In the general example taken above, it can be seen that one zero exists between the first and second poles (ω_1 and ω_2). However, because T_3 was assumed as negative, the zero between the second and third poles is missing. This zero can actually be found at a higher frequency, and there is a final zero at infinity.
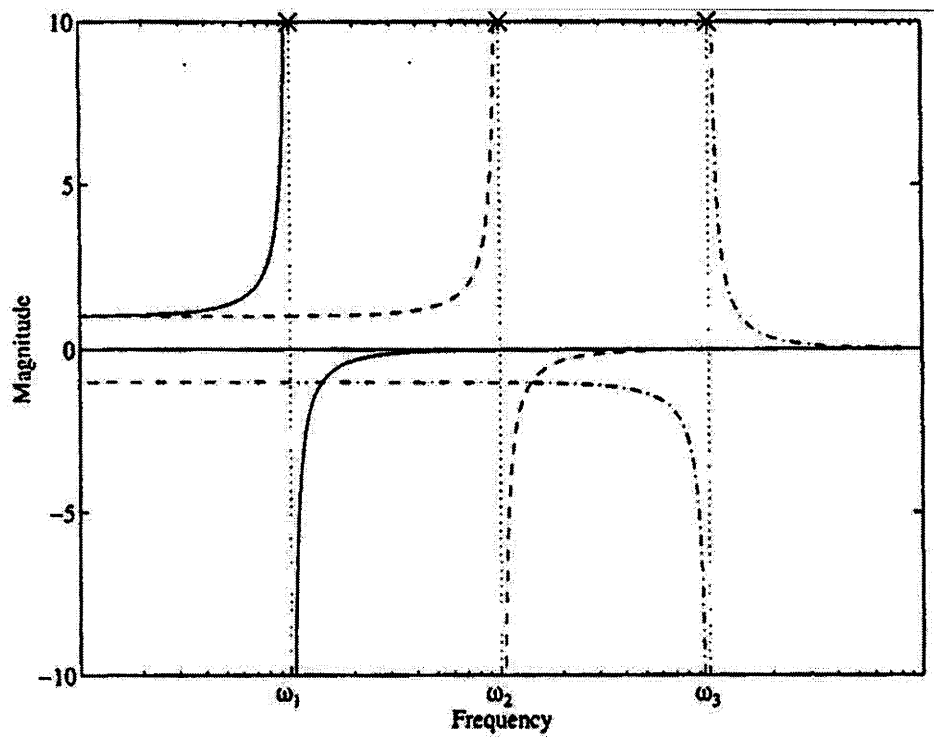
(a) Three individual systems.
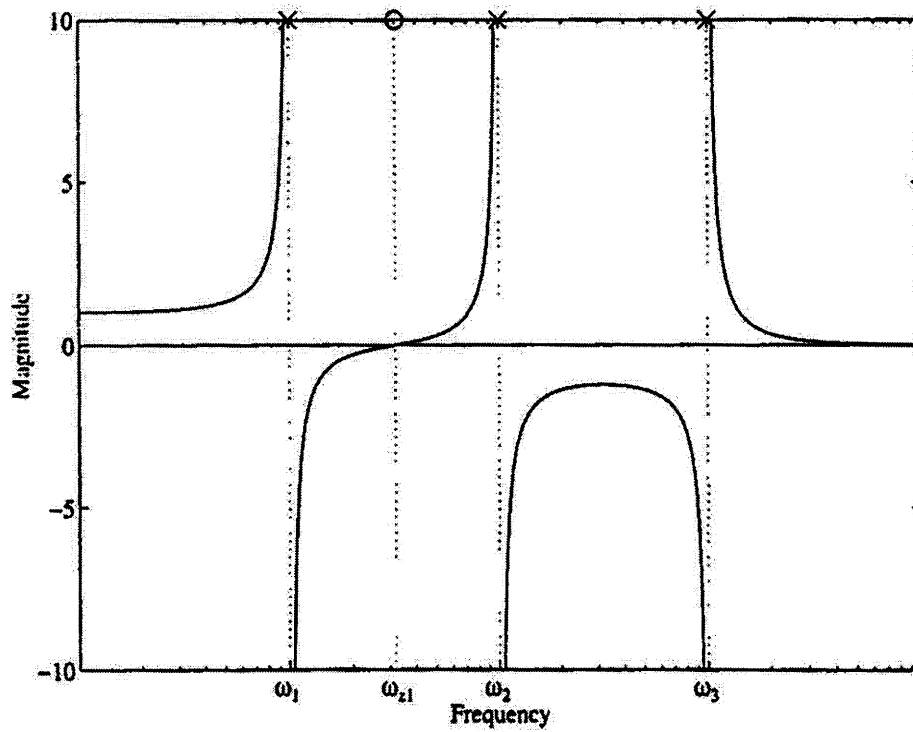
(b) Sum of the three systems.

Figure 6.1: Summation of Adding Three Resonances

101
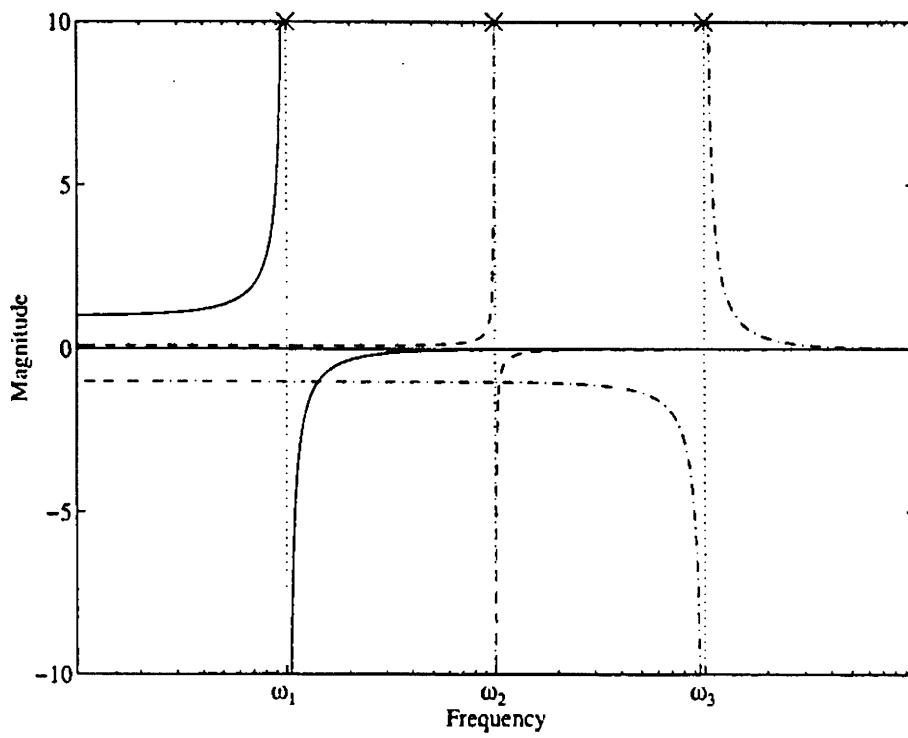
(a) Three individual systems.
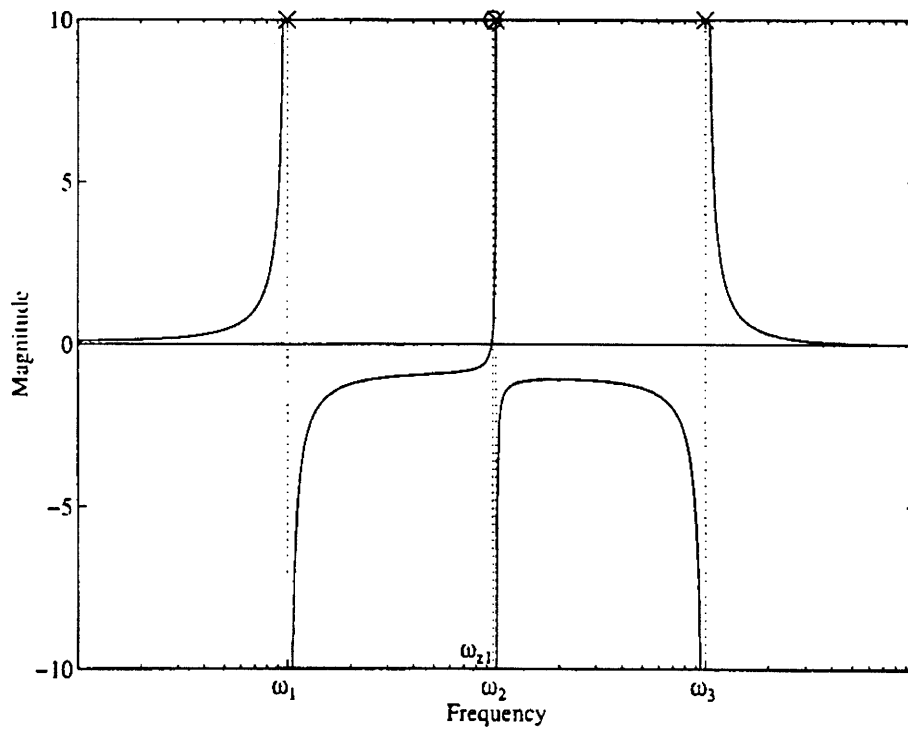
(b) Sum of the three systems.

Figure 6.2: Summation of Residues with T_2 Reduced by Factor of 10

The behavior of zeroes in a the transfer function can be qualified by successively reducing the value of T_2 and replotting the transfer function. As can be seen in Figure 6.2, where the individual and summative transfer functions are shown when T_2 is reduced by a factor of 10, the zero can be seen to be migrating towards the pole at ω_2. In general, as the residue T_i is reduced, the zero will move towards the corresponding pole at ω_i. In the limit as T_i vanishes, the zero comes to reside on top of the pole ω_i. Note that the modal residue T_i can be decreased by reducing either the modal observability or the modal controllability.

Hence, one can say that the qualitative dynamics of modal transfer functions can be characterized by their pole-zero patterns, and are captured by the following behavior:

1. The relative closeness of a zero to a pole versus the relative uniform spacing, indicating the relative magnitude of neighboring residues
2. The presence or absence of a zero between two poles, indicating whether the residues algebraically have the same or different signs

It should be noted that for damped and complex systems, the physics of the problem is the same, but the mathematical interpretation of the model is more complex.

As an aside, it should be noted that there are several formal definitions for zeroes, depending on the representation of the transfer function. For a rational representation of single-input/single-output system, the transfer function from the input to the output can be written as:

$$G_{yu}(s)) = \frac{y}{u} = \prod_{r=1}^{2N} g_{yu} \frac{(s - z_r)}{(s - p_r)} \tag{6.4}$$

where p_r represents the rth pole, z_r represents the rth zero, and g_{yu} represents the gain at zero frequency, or the DC gain. This form most easily accommodates infinite zeroes. For an output y, there are 2N poles, 2N zeroes and a zero frequency gain of g_{yu}. In this representation, the zeroes are explicit. However, the cancellation of a pole by a zero can occur

without affecting the mathematical form of the transfer function, and this new reduced transfer function no longer captures the dynamics of the structure or system being modelled.

The second definition of a zero occurs from the residue expansion definition for a single-input/single-output system:

$$G_{yu}(s) = \frac{y}{u} = \sum_{r=1}^{2N} \frac{R_{yu,r}}{(s - p_r)} + D_{yu} \tag{6.5}$$

where for a structural system with a displacement output:

$$G_{yu}(s) = \frac{[C_{yq}]\{\phi_r\}\{\phi_r^T\}[\beta_u]}{(s - \lambda_r)} \tag{6.6}$$

The advantage of this pole-residue representation is that the modal observability and controllability are easily observed. However, the zeroes are now implicit within these two quantities. Note, however, that in both formulations, there are 2N poles, and 2N+1 other pieces of information characterizing the system. These 2N+1 pieces of information are either:

1. 2N zeroes and the low frequency (DC) gain

or

2. 2N residues and the high frequency feedthrough (D_{yu})

These two definitions of zeroes are primarily used to characterize single-input/single-output systems, although the pole-residue form can be generalized to multivariable systems by defining a residue matrix. In addition, each representation can be used to represent a multiple-input/multiple-output system by constructing a matrix of cross-coupled transfer functions. We shall confine our discussion to the single-input/single-output interpretation for the remainder of this chapter.

6.3 Relationships between Zeroes and Residues

In order to understand the behavior of the transfer function of a mode of a complex structure, some formal insight must be achieved as to the relationship between the zeroes and the residues of the transfer function, as the residues of the transfer function ultimately influence the magnitude of the overall output of the system in the time domain. In the case where the modal frequencies of the model have been previously determined, only the zeroes and residues of the transfer function remain in order to create a deterministic model [10].

The residue of a transfer function at a given pole determines the magnitude of the effect of that pole upon the overall output of the system. Finding the residues of a transfer function if the zeroes are known is relatively straightforward. Using the polynomial representation of the transfer function, the residue can be found using the complex variable residue expansion theorem:

$$R_{yu,r}(p_r) = \frac{1}{(m-1)}\left[\frac{d^{m-1}}{ds^{m-1}}\{(s-p_r)^m G_{yu}(s)\}\right]\Bigg|_{s=p_r} \tag{6.7}$$

where there are m repeated poles. For a single pole, this reduces to:

$$R_{yu,r}(s) = [(s-p_r)G_{yu}(s)]\big|_{s=p_r} = \lim_{s \to p_r}(s-p_r)G_{yu}(s) \tag{6.8}$$

Consider for simplicity's sake, a two degree of freedom undamped free-free beam whose transfer function can then be written as:

$$G_{yu}(s) = \frac{y}{u} = g\left[\frac{\left(1-\frac{s}{z_{1a}}\right)\left(1+\frac{s}{z_{1b}}\right)\left(1-\frac{s}{z_{2a}}\right)\left(1+\frac{s}{z_{2b}}\right)}{\left(1-\frac{s}{j\omega_1}\right)\left(1+\frac{s}{j\omega_1}\right)\left(1-\frac{s}{j\omega_2}\right)\left(1+\frac{s}{j\omega_2}\right)}\right] \tag{6.9}$$

If there is no high frequency feedthrough term, then the two zeroes z_{2a} and z_{2b} are at infinity and the residues are given by:

$$R[j\omega_1] = g\left|\frac{\left(1 - \frac{j\omega_1}{z_{1a}}\right)\left(1 - \frac{j\omega_1}{z_{1b}}\right)}{2\left(1 - \frac{\omega_1^2}{\omega_2^2}\right)}\right| \tag{6.10}$$

$$R[-j\omega_1] = g\left|\frac{\left(1 + \frac{j\omega_1}{z_{1a}}\right)\left(1 + \frac{j\omega_1}{z_{1b}}\right)}{2\left(1 - \frac{\omega_1^2}{\omega_2^2}\right)}\right| \tag{6.11}$$

and similarly for $R[\pm j\omega_2]$.

Now, when a transfer function is envisioned as a root locus diagram, it becomes apparent that there are only two possibilities for the remaining zero pair. The first is that they form a complex conjugate pair:

$$\begin{aligned} z_{1a} &= j\omega_z \\ z_{1b} &= -j\omega_z \end{aligned} \tag{6.12}$$

while the second option is that both are on the real axis at the same frequency, but one is in the right half plane, while the other is in the left half plane. The zero which is in the right half plane is termed a non-minimum phase zero:

$$\begin{aligned} z_{1a} &= \sigma_z \\ z_{1b} &= -\sigma_z \end{aligned} \tag{6.13}$$

For the complex conjugate zeroes, the residues simplify to:

$$R[j\omega_1] = g\left|\frac{\left(1 - \frac{\omega_1^2}{\omega_{z1}^2}\right)}{2\left(1 - \frac{\omega_1^2}{\omega_2^2}\right)}\right| = R[-j\omega_1] \tag{6.14}$$

and for real zeroes:

$$R[j\omega_1] = g\left[\frac{\left(1+\dfrac{\omega_1^2}{\sigma_{z1}^2}\right)}{2\left(1-\dfrac{\omega_1^2}{\omega_2^2}\right)}\right] = R[-j\omega_1] \tag{6.15}$$

The normal modal residue $T_{\omega 1}$ can now be defined by combining the complex conjugate poles or:

$$\frac{T_{\omega 1}}{1+\dfrac{s^2}{\omega_1^2}} = \frac{R[j\omega_1]}{1-\dfrac{s}{j\omega_1}} + \frac{R[-j\omega_1]}{1+\dfrac{s}{j\omega_1}} = \frac{2R[j\omega_1]}{1+\dfrac{s^2}{\omega_1^2}} \tag{6.16}$$

Therefore, the normal modal residues for the complex zeroes are given by:

$$T_{\omega 1} = g\left(\frac{\omega_2^2}{\omega_z^2}\right)\left(\frac{\omega_z^2-\omega_1^2}{\omega_2^2-\omega_1^2}\right) \tag{6.17}$$

$$T_{\omega 2} = -g\left(\frac{\omega_2^2}{\omega_z^2}\right)\left(\frac{\omega_z^2-\omega_2^2}{\omega_2^2-\omega_1^2}\right) \tag{6.18}$$

For the real zeroes, the normal mode residues are:

$$T_{\omega 1} = g\left(\frac{\omega_2^2}{\sigma_z^2}\right)\left(\frac{\sigma_z^2+\omega_1^2}{\omega_2^2-\omega_1^2}\right) \tag{6.19}$$

$$T_{\omega 2} = -g\left(\frac{\omega_2^2}{\sigma_z^2}\right)\left(\frac{\sigma_z^2+\omega_2^2}{\omega_2^2-\omega_1^2}\right) \tag{6.20}$$
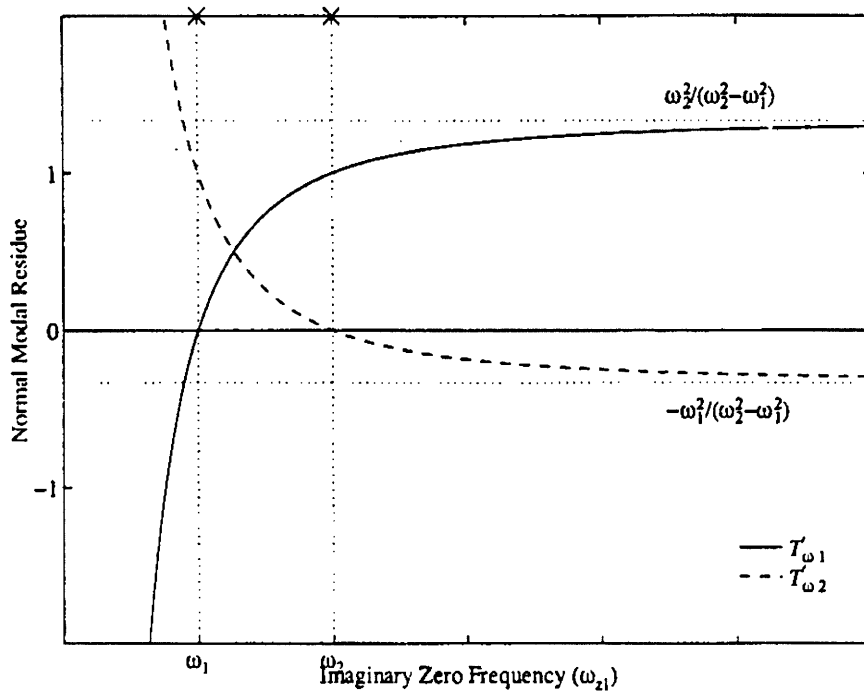
Figure 6.3: Residues as a Function of Imaginary Zero Frequency
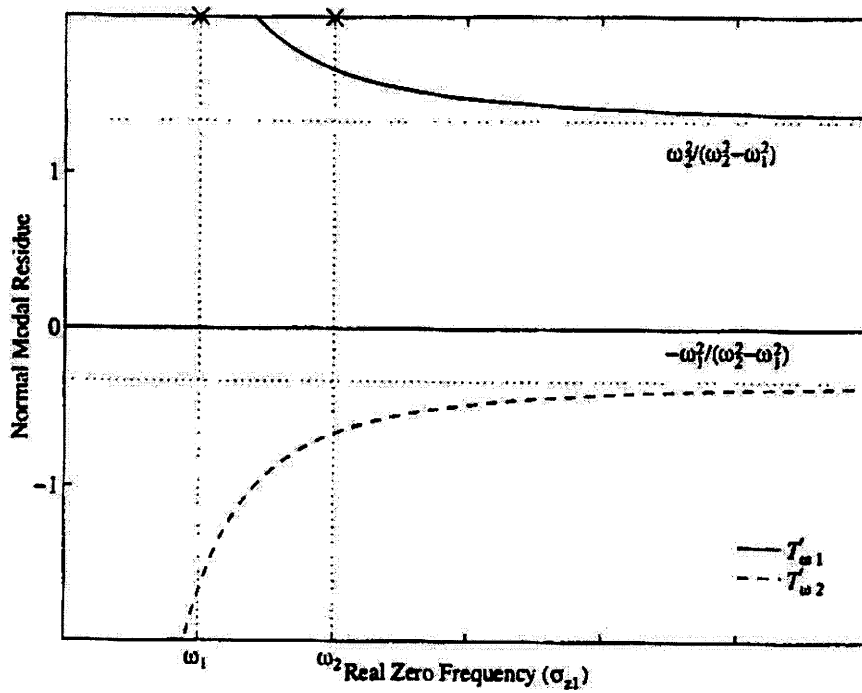
Figure 6.4: Residues as a Function of the Real Zero Frequency

To gain a better understanding of what this means for the transfer function, consider the modal residue ratio $\frac{T_{\omega 2}}{T_{\omega 1}}$ as a function of the zero frequency ω_z, be it real or complex. For most values of $\frac{T_{\omega 2}}{T_{\omega 1}}$, it can be seen from Figures 6.3 and 6.4 that a zero is in the right half plane only in the narrow range of $-1 \le \frac{T_{\omega 2}}{T_{\omega 1}} \le \frac{-\omega_1^2}{\omega_2^2}$. Thus, for this behavior, it can be seen that there are the following four possible pole-zero patterns for this transfer function:

(a) ZPP   (a) PZP   (a) PPZ   (a) NMP
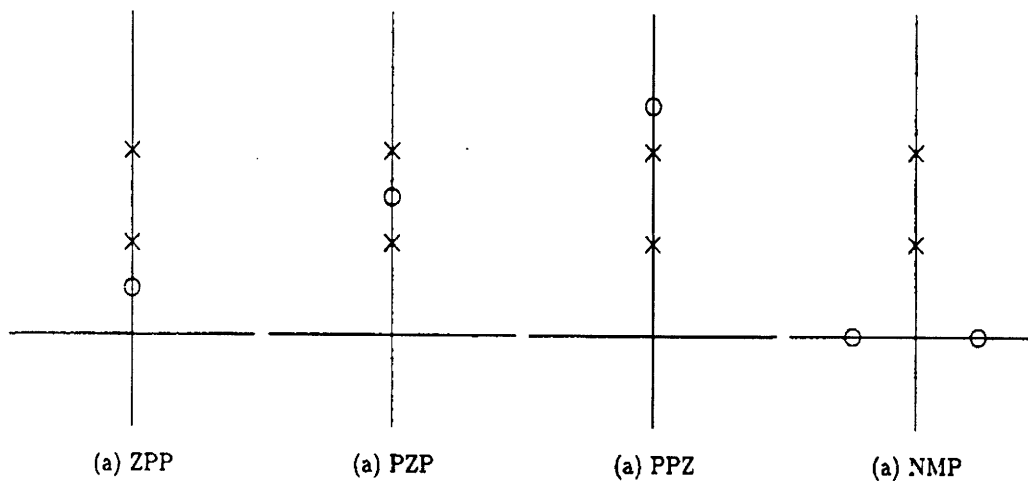
Figure 6.5: Four Possible Pole-Zero Patterns

1. The zeroes are oscillatory and below the lower pole, with a zero-pole-pole pattern (Fig. 6.5a), and the residues have opposite signs such that:

$$\frac{T_{\omega 2}}{T_{\omega 1}} < -1$$

$$|T_{\omega 2}| > |T_{\omega 1}|$$

(6.21)

2. The zero is oscillatory and between the poles with a pole-zero-pole pattern (Fig. 6.5b), the residues have the same signs and:

$$\frac{T_{\omega 2}}{T_{\omega 1}} > 0$$

(6.22)

3. The zeroes are oscillatory and above the higher pole, with a pole-pole-zero pattern

   (Fig. 6.5c), the residues have opposite signs and:

$$-\left(\frac{\omega_1^2}{\omega_2^2}\right) < \frac{T_{\omega 2}}{T_{\omega 1}} < 0$$

$$|T_{\omega 2}| < \left(\frac{\omega_1^2}{\omega_2^2}\right)|T_{\omega 1}|$$

(6.23)

4. The zeroes are real and one is in the right half plane (Fig. 6.5d), the residues have

   opposite signs and:

$$-1 < \frac{T_{\omega 2}}{T_{\omega 1}} < -\left(\frac{\omega_1^2}{\omega_2^2}\right)$$

$$\left(\frac{\omega_1^2}{\omega_2^2}\right)|T_{\omega 1}| < |T_{\omega 2}| < |T_{\omega 1}|$$

(6.24)

For the case of this simple, two degree of freedom approximation of a structure, the

transfer function for both zeroes is given by:

$$G_{yu}(s) = \frac{T_{\omega 1}}{\left(1 - \frac{\omega^2}{\omega_1^2}\right)} + \frac{T_{\omega 2}}{\left(1 - \frac{\omega^2}{\omega_2^2}\right)}$$

(6.25)

so the value for zero frequency gain is given by:

$$G_{yu}(\omega = 0) = T_{\omega 1} + T_{\omega 2} = g$$

(6.26)

The transfer functions are drawn for all these cases in Figure 6.6.

The most subtle case involves the right half plane (or non-minimum phase) zero. As

can be seen by the graph of the transfer function (Fig. 6.6 d), the presence of the non-min-

imum phase zero is not readily apparent. Hence, deductive reasoning must be applied to

any suspicious responses of the system to excitation.
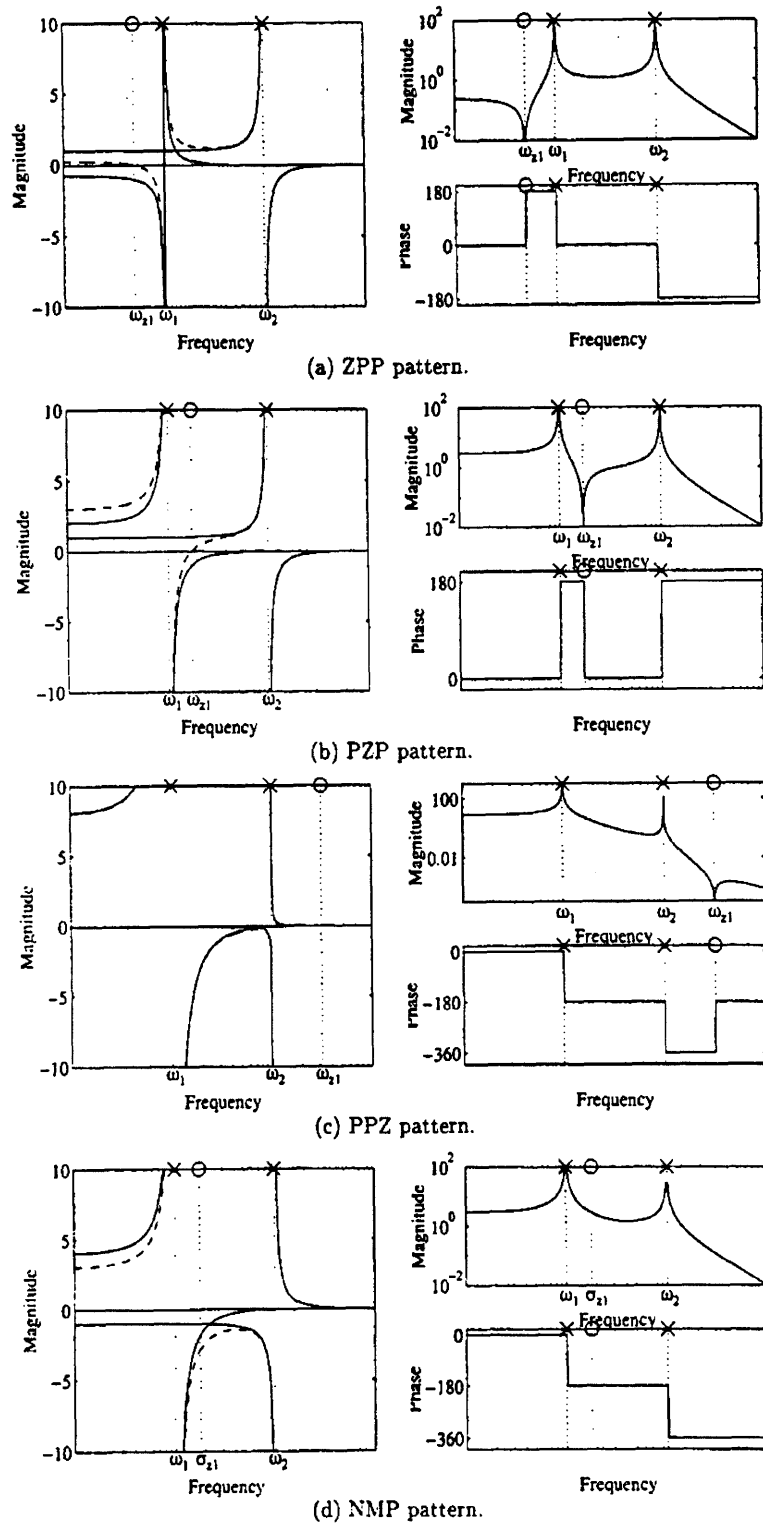
Figure 6.6: Magnitude and Bode Plots of Four Pole-Zero Patterns

111

In the case of a right half plane zero, there is an apparent mismatch between the direction of the response at low and high frequency. At low frequency $(\omega < \omega_1)$, the system responds in the same direction as the applied force. At high frequency, in the initially dominated frequency range $(\omega > \omega_2)$, the system also responds in the same direction as the applied. force. One way to recognize the presence of a right half plane zero is by noting that the low frequency response occurs in the direction of the force, then, after the first pole of the system has been reached, the response occurs in a direction opposite to the forcing function, and finally, when the frequency of the second pole has been surpassed, the response then again reverts to the same direction as the forcing function [49]. The simplest method to test for a non-minimum phase zero is to subject the structure to a step input. The step response of a right half plane zero system will first go the "wrong" way, and then eventually correct itself.

Also of note is the fact that when the two normal modal residues have the same sign, then the sign of the residue is set by the relative signs on the modal observability and controllability. So, if the modal controllability and observability have the same sign for each mode, (which is a stably interacting system), the pole zero pattern is pole-zero-pole. If they are not of the same sign, which is an unstably interacting system, the pole-zero pattern is one of the other three cases, that is: zero-pole-pole, pole-pole-zero or non-minimum-phase zero.

One way to ensure that all the modal observabilities and controllabilities are of the same sign is to force the modal observability matrix to be the transpose of the modal controllability matrix. This would be done by either measuring the input and output at the same location or in the same axis direction. Since neither of these holds true for the input forces and output accelerations measured aboard the Priroda module during the EDLS experiment, there is no guarantee of a stable pole-zero-pole pattern in the theoretical rep-

resentation of the experimental transfer function. This leads to the very serious issue of output blocking by zeroes.

6.4 Output Blocking by Zeroes

The physical interpretation of an output blocking zero is that if a structure is driven harmonically at the input point at the frequency of the zero of the transfer function, the output point does not move. This result becomes obvious in the special case when the input and output of the model are measured from the same point. This arrangement of input-output measurement is termed collocated. The zeroes of a collocated system are exactly at the resonant frequencies of the same system if the point at which the collocated input and output are being taken is "locked", that is, unresponsive in output to the excitation provided by the input. In general, the zeroes of a transfer function between an input and output that are collocated and have the same type and direction are the resonances of the same system if the degree of freedom corresponding to the input and output were removed.

(a)

(b) System (a) if mass 2 was locked.
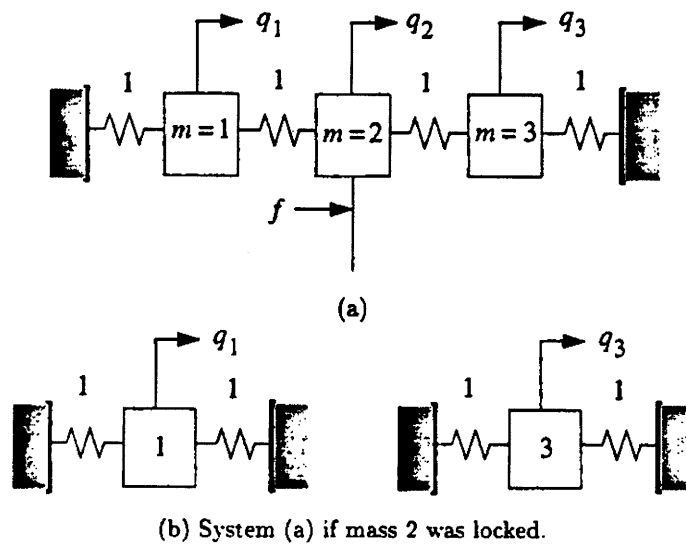
Figure 6.7: (a) Zeroes of System become (b) Poles of System

113

For a non-collocated system, however, there is the added worry of 'missing' zeroes. It is generally true that as the input and output of a transfer function become noncollocated, the number of zeroes in the frequency range of interest begins to diminish, and then start to appear as 'missing' zeroes between two poles [10].

(a) free-free beam.
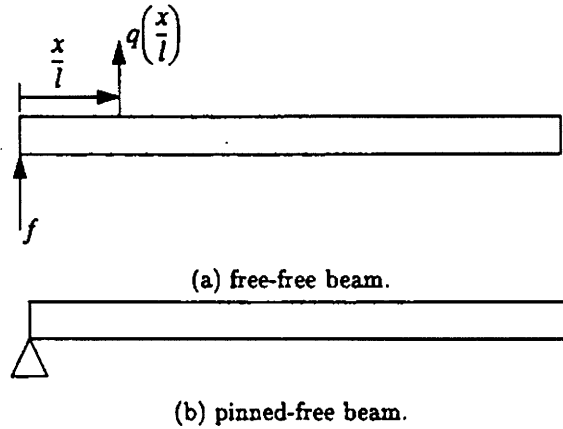
(b) pinned-free beam.

Figure 6.8: (a) Zeroes of a Free-Free Beam (b) Poles of a Pinned-Free Beam

Taking the general case of the free-free beam (Fig. 6.8 (a)), where the input f is at $\frac{x}{l} = 0$ (i.e., the left end), and the output is a measured displacement $q\left(\frac{x}{l}\right)$ and is allowed to vary along the length of the beam. When $q = q(0)$, the input and output are collocated and the zeroes of the system are the same as the resonant frequencies of the pinned free beam (Fig 6.9(b))[1]. The location of these poles and zeroes are shown in Figure 6.9 for $\frac{x}{l} = 0$.

As the location of the output moves away from the input $q = \frac{x}{l} > 0$, the zero frequencies rise in their frequency. Examining the first two poles, the rigid body mode at $\omega_0 = 0$ and the first flexible pole at $\omega_1 = 22.4$ (where ω_i is the non-dimensionalized frequency in Chapter 3), they have an intervening zero, that is, a pole-zero-pole pattern, until $\frac{x}{l} \cong 0.22$.

---

1. The system has the output locked at the point of input, as if by placing a pin or restraint there, constraining that degree of freedom.

114
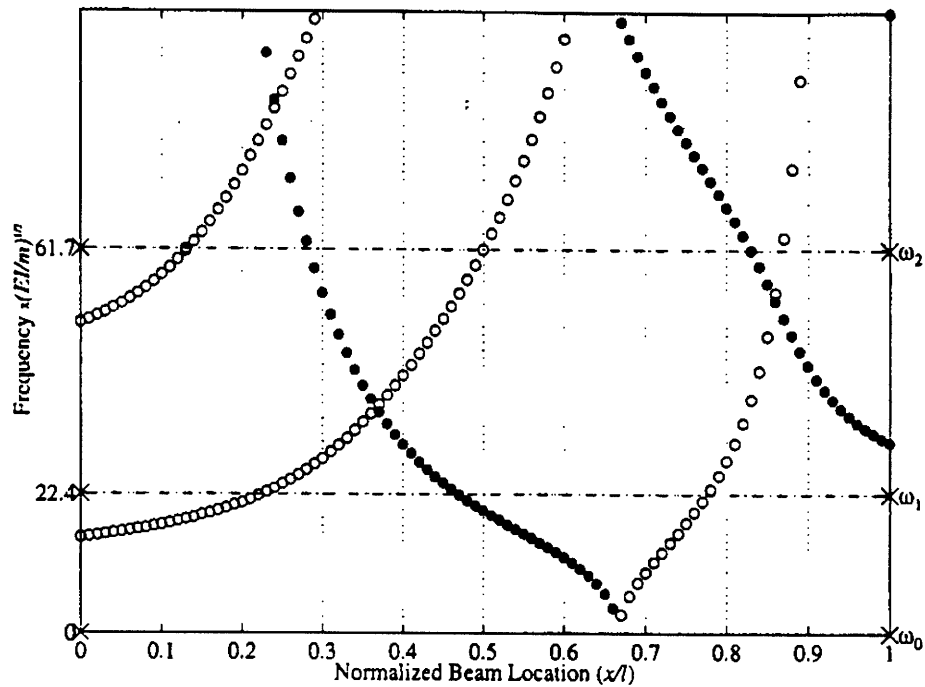
Figure 6.9: Movement of Zeroes on FF Beam as Sensor Location Changes

At that location, the zero passes beyond the first flexible pole, and the pattern of the first

two poles becomes a pole-pole-zero pattern. Interestingly enough, it can be seen that at

$\frac{x}{l} \cong 0.22$, a right half plane zero also appears. As the input and output become more non-

collocated, the non-minimum phase zero decreases in frequency, crossing each mode until

it becomes a complex zero pair again at $\frac{x}{l} \cong 0.67$, which is the center of percussion of the

beam (i.e., both zeroes are superimposed on the root locus diagram). Beyond $\frac{x}{l} \cong 0.67$

there is an intervening zero between the poles again.

While the zeroes in the collocated transfer function are the resonances of the pinned-

free beam, the zeroes for the non-collocated transfer function do not yield to any simple

physical interpretation. When examined in the Laplace domain, the general zero move-

ment is shown in Figure 6.11.

115
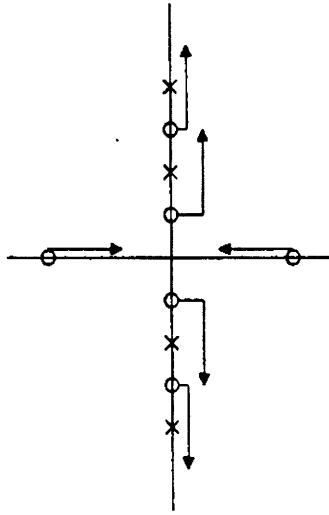
Figure 6.10: Movement of Zeroes on FF Beam for Increasing Non-Collocation

The zeroes tend to "rise" relative to the poles as the degree of noncollocation increases. With enough non-collocation, real zeroes appear in minimum and non-minimum phase pairs and descend into the frequency range of interest, forming a non-minimum phase system. Such motion of zeroes up the $j\omega$ axis and on the σ axis is sometimes called "circulation" of the zeroes. Thus, it becomes difficult in the extreme to predict the collocated position of the zeroes of the experimental transfer function.

The case of $\frac{x}{l} \cong 0.22$ is a special case of an output blocking zero. At this point, the output is at a node of the first free-free mode of the beam, thus making the mode unobservable. What this means, is that if a displacement sensor attached to the beam at this point along its length, it would witness no change in displacement for any excitation. This is due to the fact that the nodes of a natural frequency do not displace when the mode shape corresponding to that natural frequency is excited. This is mathematically made obvious by the fact that when a mode becomes unobservable, the normal mode residue of that mode goes to zero, that is:

116

$$[C_{yq}]\{\phi_r\} = 0 \qquad\qquad (6.27)$$

This is the case of the rth zero cancelling the rth pole. The output blocking "direction" takes on a special form at the moment of loss of observability. The direction of the rth zero for this case is found by solving the eigenvalue problem. Hence, it becomes obvious that for any input, a zero output will occur. These losses of observability are the limiting case of output blocking by zeroes.

6.5 Implications Non-Collocation upon Transfer Functions

As is previously stated, the transfer function for the model of a complex structure such as a space station can be fully determined where the station is modelled as a series of intersecting free-free beams. The poles of the transfer function will be the natural frequencies of all of the free-free beam-modules, superposed together. The zeroes can then be approximated by modelling the clamped-free natural frequencies of the same beam-modules, due to the assumption that the joints between station modules are rigid. Hence, using the values for the eigenvalues of a clamped-free beam and a free-free beam as calculated in equation 3.24 and 3.37, and the material properties of the Priroda module from Table 2.1, the poles and zeroes of the theoretical transfer function can be evaluated.

Using the values of the poles and zeroes in the transfer function representation equation 6.1, the residues can be calculated using the methods of Section 6.3. It immediately becomes apparent that the transfer function thus derived does not match the experimental transfer function of Section 5.2. This is due to the assumption that the zeroes of the transfer function can be approximated by the poles of the clamped-free beam identical to the free-free beam from which the poles are determined. This assumption is only valid if the input and output to the transfer function are collocated, that is, located in the same position.

In the case of the input data taken from the EDLS experiment aboard Mir, and the correlated SAMS data, it is obvious that the input and output signals are not collocated. Thus, it becomes impossible to predict the frequency of the collocated zeroes based on the non-collocated data. Coupling this uncertainty with the possibility of falling prey to output blocking zeroes, the mathematical model of the experimental transfer function can only be used with great caution in order to extract the particular behavior of the structure. Due to the fact that the model assumes the zero frequencies occur at the clamped-free frequencies of the module, once the experimental non-collocated zeroes begin to circulate, there is no means by which to bound the error in the theoretical transfer function [84]. With the possibility of a non-minimum phase zero, or an output blocking zero, the stability of the system is impossible to predict. Simple order-of-magnitude conclusions can be made with great certainty, but beyond that, treacherous assumptions must be made in order to progress beyond generalizations.

Essentially, after the input and output data has been filtered, transformed and re-filtered, the frequency responses of the output and the input can be used to estimate the transfer function over a series of samples in a least squares sense in order to achieve an experimental plot of the transfer function. As can be seen, the bandwidth of the input activity is concentrated about the 0.4 Hz point, while the output activity is of the maximum order of 7.5×10^{-6} g. Hence, the effect of astronaut motions on the overall acceleration of the Russian Space Station Mir is minimal at best, especially when compared to other events, such as station reboosting, which is of the order of 1×10^{-3} g, or Shuttle or Soyuz docking, which is of the order of 1×10^{-2} g [24]. Thus, while astronaut motion is of great interest, it should not be the predominant consideration for determining structural and experiment design for the International Space Station.

This data is in accordance with the analysis performed by the McDonnell Douglas Aerospace Transient Loads Group [52], which analyzed the effects of astronaut motion in the time domain, attempting to find the effect of transients in acceleration due to astronaut forces.
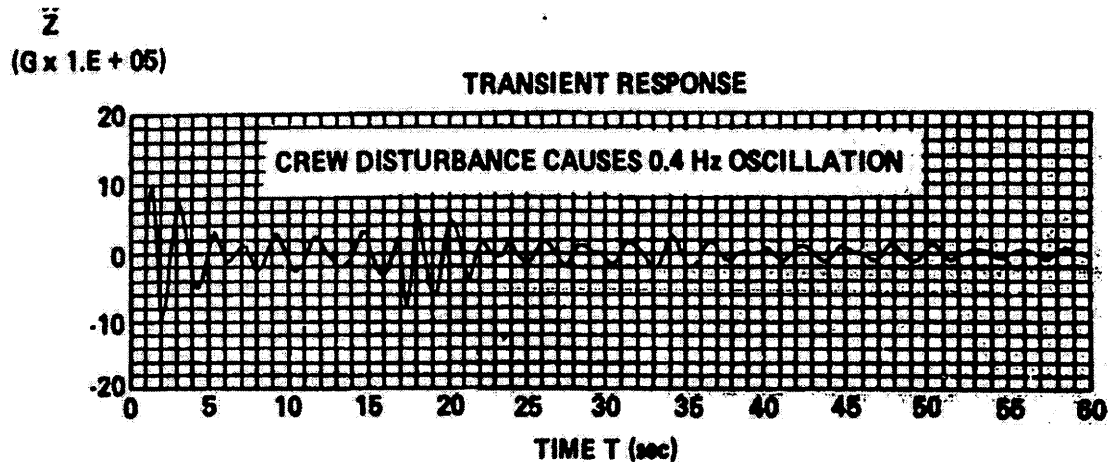
Figure 6.11: NASA/JSC Time Domain Acceleration Analysis of Crew Motion [6]

The data analysis from this experiment also predicts a major resonance due to astronaut motion at approximately 0.4 Hz oscillation [6], very close to the largest resonant peak at 0.375 Hz indicated by the transfer function. Thus the general experimental transfer function should be used to quantify the effect of astronaut motions on the Russian Space Station Mir. The theoretical transfer function should be used only with great caution, and only in the case of collocated input/output sensors. Otherwise, the possibility of encountering non-minimum phase zeroes or output blocking zeroes due to improperly modelled dynamics is very high, even for small degrees of non-collocation.

Chapter 7

Conclusions and Recommendations

7.1 Summary

The first chapter of this thesis stated the primary objective of this work: to find a transfer function between forces caused by astronaut motion aboard a space station and the station's overall acceleration as a result of these forces. The second chapter helped provide the motivation for this goal, as a description of previous space stations, and the microgravity environment aboard a space station was given. As well, background was provided upon previous experiments designed to measure forces exerted by astronauts in a microgravity environment. Finally, a survey of analytical modelling techniques for the modal analysis of space stations was conducted.

The subject of Chapter 3 was the study of the dynamics of a modular space station modelled by a main rigid node connected to several flexible appendages. The aim of this chapter was to conduct a modal analysis of this particular topology of system. It was hypothesized that due to the rigid nature of the joints between the main node and the flexible appendages, the station could be modelled as an intersection of free-free beams in space. It was shown that the flexible appendages could then be individually modelled as cantilever beams. A method for calculating higher mode shapes was then advanced. This simplistic, continuous Euler-Bernoulli beam model of a generic modular space station was then discretized, thus placing it in a form more conductive to transfer function analysis.

In Chapter 4, the EDLS experiment is discussed in detail. Due to the failure of the MODE ESM, the MiSDE ESM was substituted, necessitating a thorough postflight calibration. After the postflight calibration, the data was processed by the EDLSAP software.

The data was reduced during the extraction process, where all of the extraneous noise was eliminated, and the remaining signals were divided into small files containing individual motions. Of the 1440 identified motions, only 614 were usable due to difficulties with the PDS analysis, and various other factors. From these 614 identified motions, the attempt was then made to correlate the force traces with video footage of the EDLS experiment. However, in the end, only 14 classified motions, mainly pushoffs and landings, were verifiable through both the force data and the video. The maximum force, RMS force and 95% PSD values were calculated for each motion. As well, the SAMS experiment is discussed, and techniques for correlating the SAMS acceleration data to the EDLS force data are postulated.

Chapter 5 provides an explanation of the technique applied to the EDLS and SAMS experimental data in order to derive a transfer function between astronaut motion forces and overall acceleration:

1. Perform the time-frequency analysis of the EDLS force input signal and the SAMS acceleration output signal.
2. For each frequency of interest, remove the noisy parts of the time-frequency representations using the appropriate filtering algorithm
3. Obtain estimates of the frequency response using the de-noised time-frequency representations of the signals

A least-squares form of minimization is then performed on the transformed force and acceleration signals, in order to "best-fit" the experimental transfer function.

The focus of Chapter 6 was directed towards relating the theoretical expression of the transfer function to the experimentally determined graph. This chapter addressed the discrepancies between the theoretical transfer function model derived in Chapter 3 and the experimental transfer function calculated in Chapter 5. The concept of how information is stored in a transfer function is addressed, and the significance of poles and zeroes is elucidated. The issue of sensor collocation is discussed, with the concepts of modal observability and controlability in the forefront. The ramifications of sensor collocation on the

correlation process between force and acceleration data is then outlined, and the discrepancy between the degree of validity of the theoretical model and the experimental data is clarified.

7.2 Conclusions

The results of the statistical analysis on the 614 motions from the EDLS force data showed that the majority of astronaut motions are not overly forceful. Approximately 95% of all motions possessed a maximum force less that 275 N, an RMS force less than 60 N and a PSD less than 22 Hz. Hence, the level of disturbance caused by astronaut motion does not seem to be such that it would create a major concern when devising design constraints and computing safety factors for a space station. Astronaut motion forces are certainly several orders of magnitude below the disturbance forces caused by the docking of the Soyuz vehicle with Mir.

A trend was detected in the magnitude of the force traces during the performance of a pushoff at different times during the mission. The pushoff performed at the beginning of the mission for the astronaut had a 15% higher force magnitude than one performed much later in the mission, even though the profiles of the force traces were similar in shape. This would seem to indicate the implementation of an adaptive control strategy by an astronaut who has been in the microgravity environment for a long period of time for the execution of common motions. However, much more study into this phenomenon must be accomplished before concrete conclusions can be drawn.

A crude model for a topologically modular space station was derived by representing each module as a flexible cantilever beam attached to a rigid node. Hence, employing modal analysis techniques, an expression for the transfer function between the input (the

forcing function of an astronaut load) and the output (the acceleration of the station) for a given space station module was found to be:

$$\ddot{y} = \sum_{r=1}^{N} \frac{[C_{yq}]\{\phi_r\}\{\phi_r^T\}[\beta_u]}{m_r(s^2 + \omega_r^2)} s^2 u \qquad (7.1)$$

In conjunction with this, the forces from the EDLS motions which had been correlated with the accelerations from the SAMS data were filtered, de-noised and then transformed into the frequency domain, where they were used to calculate an experimental transfer function between astronaut forces and the Priroda module acceleration. The pole with the maximum residue was found at approximately 0.375 Hz, and had a magnitude of about 7.5×10^{-6}. This was corroborated by the experimental data from the NASA-Johnson Transient Loads Group analysis [52,6], which placed a large resonance at 0.4 Hz due to the transients from astronaut motions.

The major cause for discrepancy between the theoretical transfer function and the experimental transfer function was due to the lack of collocation between the force and acceleration sensors. Without the assumption of collocated input and output, it becomes impossible to validate the theoretical transfer function. The non-collocated input negates the assumption that the transfer function zeroes occur at the clamped free modes of the equivalent free-free beam. Thus, a meaningful comparison between the theoretical model and the experimental results could not be carried out.

7.3 Recommendations

For a future modelling study, a similar modal analysis of a generalized large space structure could be carried out, taking into account the more realistic case where the structure is gravity gradient stabilized and revolves around the Earth in a circular orbit with a constant angular velocity. This analysis of a spinning structure would be further complicated by the fact that the natural frequencies and modes of vibration lead to complex eigenvectors asso-

ciated with real eigenvalues, due to the gyroscopic forces [61]. The rotating base cantilever modes of the flexible module will still, however, constitute a set of independent orthogonal vectors, which can be used to expand the overall deflection response (and by extension, acceleration) of the module. It is expected, however, that the analytical form for the eigenfucntions for the rotating modes cannot be expressed in a closed form solution, due to the fact that the terms involving centrifugal and gravity gradient effects are non-constant forcing functions.

If the original database of 1440 motions could be reanalyzed, it might be advantageous for the motions to be extracted such that they did not overlap in different sensors. This would eliminate the noise incorporated into the PSD calculation for the motion, probably eliminating any anomalously high statistics, rendering more motions viable for constructive analysis [8].

Further investigation into the adaptive ability of astronauts in microgravity environments for long periods of time should be conducted. A careful study should be made of the minimum mission length required for the astronaut to evince adaptive strategies during the performance of simple motions. As well, an investigation into the effect of mission duration upon the success of these adaptive strategies would also be beneficial to the overall understating of adaptive astronaut control in microgravity environments.

Improved video footage, with the focus being upon the astronaut's interaction with the sensor surface would be a great asset. As well, a standard method for time synchronization between spaceflight experiments, astronauts and video footage should be adopted, thus greatly aiding in the attempt to correlate data from different experiments, as well as identifying landmark occurrences during experiments.

Finally, experimental data between a collocated input force sensor and output acceleration sensor would be invaluable. It would aid in the verification of the theoretical model of the

force-acceleration transfer function of a space station. If any further experiments such as

EDLS and SAMS are to be conducted on board a space station, an attempt at collocating

the accelerometer heads with the force plate sensors would be of inestimable value

towards future validation of any analytical models.

References

[1] Admire, John R., Michael L. Tinker and Edward W. Ivey, "Mass-Additive Modal Test Method for Verification of Constrained Structural Models", American Institute of Aeronautics and Astronautics Journal, Vol. 31, No. 11, November 1993.

[2] Amir, A. R., "Design and Development of Advanced Load Sensors for the International Space Station", Engineer in Aeronautics and Astronautics Thesis, Massachusetts Institute of Technology, Cambridge, MA, September 1998.

[3] Anderson, J.B., Driskill, T.C., and P. Jefferson, "Space Station Common Module Prototype Fixed-Base Modal Survey Test Report", SS-DEV-ED91-005, NASA/MSFC, Huntsville, AL, April 1991.

[4] Armand, S. and P. Lin, "Influence of Mass Moments of Inertia on Normal Modes of Preloaded Solar Array Mast", 1992 MSC World User's Conference, Dearborn, Michigan, May 18-22, 1992.

[5] Baugher, Charles R., Gary L. Martin, and Richard DeLombard, "Low-Frequency Vibration Environment for Five Shuttle Missions" NASA Technical Memorandum 106059, January 1993.

[6] Berka, Reg, "Space Station Dynamics", NASA/Johnson Space Center, N91-12423, Presentation 24, pp. 1-34

[7] Boeing Defense & Space Group, "System Specifications for the International Space Station," SSP 41000, Revision H (Advanced Copy), Type 1, NASA, 25 May 1998.

[8] Brown, Robert, G. and Patrick Y.C. Hwang, *Introduction to Random Signals and Applied Kalman Filtering*, John Wiley &Sons, New York, NY, 1997, pp. 72-128.

[9] Buckingham, Bruce, "International Space Station Partners Adjust Target Dates For First Launches, Revise Other Station Assembly Launches", Kennedy Space Center Release No. 66-98, May 31, 1998.

[10] Campbell, Mark and E. F. Crawley, "Development of Structural Uncertainty Models", AIAA Journal of Guidance, Control and Dynamics, Vol. 20, No. 5, September 1997, pp. 841-849.

[11] Conway, Bruce A., "Investigation of Crew Motion Disturbances on Skylab-Experiment T-013," Advances in the Astronautical Sciences, Vol. 31, Part 1, Proceedings of the AAS 20th Annual Meeting, 1974.

[12] Conway, Bruce A., "Mathematical Crew Motion Disturbance Models for Spacecraft Control System Design," S.M. Thesis, Virginia Polytechnic Institute, August 1974.

[13] Conway, Bruce A. and T. C. Hendricks, *A Summary of the Skylab Crew/Vehicle Disturbance Experiment T-013*, NASA Technical Note D-8128, March 1976.

[14] Craig, Roy R., *Structural Dynamics: An Introduction to Computer Methods*, John Wiley & Sons, New York, NY, 1981, pp. 207-235.

[15] Crawley, E. F., M. C. van Schoor, and E. Bokhour, *The Middeck 0-Gravity Dynamics Experiment*, NASA CR-4500, March 1993.

[16] Cyril, Xavier, "Dynamics Analysis of Complex Space Structures Using Natural Orthogonal Complement", 12th International Astronautical Congress, Montreal, Canada, Oct. 1991.

[17] Del Basso, S., "The International Space Station Microgravity Environment," 34th Aerospace Sciences Meeting & Exhibit, AIAA Paper 96-0402, January 1996.

[18] DeLombard, Richard, "Compendium of Information for Interpreting the Microgravity Environment of the Orbiter Spacecraft," NASA Technical Memorandum 107032, August 1996.

[19] DeLombard, Richard, "Microgravity Environment Countermeasures Panel Discussion," 35th Aerospace Sciences Meeting & Exhibit, AIAA Paper 97-0351, January 1997.

[20] DeLombard, Richard, "SAMS Acceleration Measurements on Mir From January to May1997", NASA Increment 4, Technical Memorandum 1998-208646. October 1998.

[21] DeLombard, Richard, "Space Acceleration Measurement System on Mir Investigation 8.8.1/SAMS", Third Phase 1 Research Program Results Symposium, NASA Marshall Space Flight Center, November 3-5 1998.

[22] DeLombard, Richard, B. D. Finley, and C. R. Baugher, "Development of and Flight Results from the Space Acceleration Measurement System (SAMS)," 30th Aerospace Sciences Meeting & Exhibit, AIAA Paper 92-0354, January 1992.

[23] DeLombard, Richard and Finley, Brian D., "Space Acceleration Measurement System Description and Operations on the First Spacelab Life Sciences Mission," NASA Technical Memorandum 105301, November 1991.

[24] DeLombard, Richard and Kevin McPherson, "Comparison Tools for Assessing the Microgravity Environment of Missions, Carriers and Condition," NASA Technical Memorandum 107446, April 1997.

[25] DeLombard, Richard and et al., "An Overview of the Microgravity Environment and Its Effects on Science," AIAA Paper 96-0401, 34th Aerospace Sciences Meeting & Exhibit, January 1996.

[26] DeLombard, Richard. et al., "Further Analysis of the Microgravity Environment on Mir Space Station During Mir-16," NASA Technical Memorandum 107239, June 1996.

[27] Ellison J., G. Ahmadi, and C. Grodsinsky, "Evaluation of Passive and Active Vibration Control Mechanisms in a Microgravity Environment," Journal of Spacecraft. Vol. 32, No. 2., 1994.

[28] Feonychev, A. I., B. J. Tillotson, L. P. Torre, and H. J. Willenberg, "Characterization of the Microgravity Environment on the Salyut and Mir Space Stations," SPIE Vol. 2220, 1994.

[29] Feron, E., M. Brenner, J. Paduano and A. Turevskiy, "Time-Frequency Analysis for Transfer Function Estimation and Application to Flutter Clearance", AIAA Journal of Guidance, Control and Dynamics, Vol. 21, No. 3, June 1998, pp. 375-382,

[30] Finley, B. D., C. M. Grodsinsky and R. DeLombard, "Microgravity Environment of STS-57 and Summary Comparisons with Selected Previous Missions," AIAA Paper 94-0435, 32nd Aerospace Sciences Meeting & Exhibit, January 1994.

[31] Graham, S. J. and R. C. Rhome, "Achievements in Microgravity: Ten Years of Microgravity Research," 32nd Aerospace Sciences Meeting & Exhibit, AIAA Paper 94-0344, January 1994.

[32] Grodsinsky, Carlos M. and Gerald V. Brown, "Low Frequency Vibration Isolation Technology for Microgravity Space Experiments," NASA Technical Memorandum 101448, September 1989.

[33] Gupta, Viney K., James F. Newell and W.H. Roberts, "Band Lanczos Vibration Analysis of Aerospace Structures", Presented at the Symposium on Parallel Methods for Large-Scale Structural and Physics Applications, NASA Langley Research Center, February 5-6, 1991.

[34] Gupta, Viney K., James F. Newell, Laszlo Berke and Armand Sasan, "Modal Test/ Analysis Correlation of Space Station Structures using Nonlinear Sensitivity", NASA-TM-105850, Fourth Symposium on Multidisciplinary Analysis and Optimization, Cleveland, Ohio. September 1992.

[35] Hajela, P., "Genetic Search —An Approach to Non-Convex Optimization Problem", AIAA Journal, Vol. 28, No. 7, pp. 1205-1210.

[36] Harman, P. and D. Rohn, "The Impact of an IVA Robot on the Space Station Microgravity Environment", AIAA Paper 89-0596, 27th Aerospace Sciences Meeting, January 1989.

[37] Ho, J. Y. L., "Direct Path Method for Flexible Multibody Spacecraft Dynamics", Journal of Spacecraft and Rockets, Vol. 14, 1977, pp. 102-110.

[38] Hooker, W. W., and G. Margulies, "The Dynamical Attitude Equations for a N-Body Satellite", The Journal of the Astronautical Sciences, Vol. 12, No. 4, 1965, pp. 123-128.

[39] Hoyt B, and G. H. Kitmacher, Priroda Interface Control Document (PICD), Report JSC-27027/SM-P-Eng-01, July 1995.

[40] Huston, R. L., Passerello, C.E., and M.W. Harlow, "Dynamics of Multi-Rigid-Body Systems", Journal of Applied Mechanics: Transactions of the ASME, Vol. 45, 1978, pp. 889-894.

[41] —, "International Space Station Assembly Sequence (5/31/98: Revision D)," NASA Facts. NASA Johnson Space Center, June 1998.

[42] —, "International Space Station, U.S. Space Station History," NASA Johnson Space Center, IS-1995-08-SS004JSC, August 1995.

[43] —, "International Space Station, Russian Space Stations," NASA Johnson Space Center, IS-1995-08-SS005JSC, August 1995.

[44] Klute, Glenn K., "Pilot Investigation: Nominal Crew Induced Forces in Zero-G, "SAE Technical Paper 921155, July 1992.

[45] Kulla, P., "Dynamics of Spinning Bodies Containing Elastic Rods", Journal of Spacecraft, Vol. 9, No. 4, 1972, pp. 246-253.

[46] Kullas, Conlon M., "Handbook on Astronaut Crew Motion Disturbances for Control System Design," NASA Reference Publication 1025, 1979.

[47] Larson, Wiley J., and James R. Wertz (eds.), *Space Mission Analysis and Design*, 2nd Edition, Microcosm, 1992.

[48] Lew, Jiann-Shiun, "Transfer Function Parameter Changes Due to Structural Damage", AIAA Journal of Guidance, Control and Dynamics, Engineering Notes, Vol. 21, No. 3, May 1998, pp. 525-527.

[49] Likins, P.W., Barbera, F. J. and V. Baddeley, "Mathematical Modeling of Spinning Elastic Bodies for Modal Analysis", AIAA Journal, Vol. 11, No. 9, 1973, pp. 1251-1258.

[50] Lockheed Martin Space Mission Systems & Services, *International Space Station On-Orbit Assembly, Modelling and Mass Properties Databook*, Contract NAS-9-19100, Huston, Texas, October 1997.

[51] MacNeal, R.H., "A Hybrid Method of Component Mode Synthesis", Computers and Structures, Vol. 1, 1971, pp. 581-601.

[52] McDonnell Douglas Aerospace Transient Loads Group, "On Orbit Transient Loads Integrated Finite Element Model Report", International Space Station Incremental Design Review 2, November 15, 1995.

[53] Meirovitch, L., "A Stationarity Principle for the Eigenvalue Problem for Rotating Structures", AIAA Journal, Vol. 14, No. 10, 1976, pp. 217-234.

[54] Modi, V. J. and A. Suleman, "An Approach to Dynamics of Flexible Orbiting Systems with Application to the Proposed Space Station", 12th International Astronautical Congress, Montreal, Canada, Oct. 1991.

[55] Moore, Cherice et al., "Phase 1: A Journey to Mir 1994–98" CD-ROM SM-G-472, Lockheed Martin, 1998.

[56] Morgan, S.E., "Avoiding on-Orbit Control/Structure Interaction Problems with Space Station Freedom", SAE Aerotech 1992 Conference, Anaheim, CA, Oct. 5-8, 1992, pp.10-12.

[57] Moskowitz, Milton E., "SAMS Acceleration Measurements on Mir From March to September 1996," NASA Technical Memorandum 107524, August 1997..

[58] Newman, D. J., Marthinus van Schoor, and Javier de Luis, "Crew Force Measurements: Dynamic Load Sensors (DLS) on Mir," Proposal to the NASA Office of Life & Microgravity Sciences & Applications, May 1994.

[59] Newman, Dava J., Michail Tryfonidis, and Marthinus C. van Schoor, "Astronaut-Induced Disturbances in Microgravity," Journal of Spacecraft and Rockets, Vol. 34, No. 2, March–April 1997.

[60] Pappa, Richard S., Stanley E. Woodard, and Jer-Nan Huang, "A Benchmark Problem for Development of Autonomous Structural Modal Identification", 15th International Modal Analysis Conference, Society for Experimental Mechanics, Inc. February 1997, pp. 1071-1077.

[61] Pascal, M., "Modal Analysis of a Rotating Flexible Space Station by a Continuous Approach", Dynamics and Control of Structures in Space III, Proceedings of the 3rd International Conference, May 1996, pp. 491-505.

[62] Patnaik, S.N., J.D. Guptill, and L. Berke, "Singularities in Optimum Structural Design", NASA Technical Memorandum 4365, Washington, D.C. 20546-0001, March 1992.

[63] Plang, Ronnie D., et al., "International Space Station Alpha Reference Guide, Incremental Design Review #1," Boeing Defense & Space Group, March 29, 1995.

[64] Poli, Corrado R. "Effect of Man's Motion on the Attitude of a Satellite," Journal of Spacecraft, Vol. 4, No. 1, January 1967.

[65] Roberson, Robert E., "Comments on the Incorporation of Man into the Attitude Dynamics of Spacecraft," The Journal of the Astronautical Sciences. Vol. X, No. 1, Spring 1963.

[66] Roberson, R.E., and J. Wittenberg, "A Dynamical Formalism for an Arbitrary Number of Interconnected Rigid Bodies, with Reference to the Problem of Attitude Control", Proceedings of the 3rd International Congress of Automatic Control, Butterworth, London, 1967.

[67] Robey, J., "Planning for Microgravity Science Research on the International Space Station," 35th Aerospace Sciences Meeting & Exhibit, AIAA Paper 97-0106, January 1997.

[68] Rochon, Brian V. and Steven A. Scheer, "Crew Activity & Motion Effects on the Space Station," Presented at the Workshop on Structural Dynamics and Control Interaction of Flexible Structures, George C. Marshall Space Flight Center, April 22–24, 1986.

[69] Rogers, M. J. B., et al., "A Comparison of Low-gravity Measurements On-board *Columbia* During STS-40." Microgravity Science & Technology. Vol. VI, No. 3, 1993.

[70] Rose, David, International Space Station Familiarization, NASA Space Flight Training Division, Mission Operations Directorate, ISS FAM C 21109, December 1997.

[71] RSC "ENERGIA", "Complex of Structure Dynamic Experiments During STS-71 through STS-91 Missions", Third Phase 1 Research Program Results Symposium, NASA Marshall Space Flight Center, November 3-5 1998.

[72] Rubin, S., "Improved Component Mode Representation for Structural Dynamic Analysis", AIAA Journal, Vol. 13, 1975, pp. 995-1006.

[73] Sellappan, R., and P. M. Bainum, "Motion of Spinning Spacecraft with Hinged Appendages", AIAA Journal, Vol. 15, No. 6, 1977, pp. 866-869.

[74] Sepulveda, A.E., and L.A. Schmit, "An Approximation Based on Global Optimization Strategy for Structural Synthesis", AIAA 32nd Structures, Structural Dynamics, and Materials Conference, Paper No. AIAA-91-1035, Baltimore, Maryland, April 8-10, 1991.

[75] Sridhar, Banavar, "Identification of Space Station Dynamics", Proceedings of 24th IEEE Conference on Decision and Control, Ft. Lauderdale, FL, December 1985, pp. 1264-1265.

[76] Suleman, Afzal, "Dynamics and Control of Evolving Space Platforms: An Approach with Applications", Report No. ISBN-0-315-79707-X, Ph.D. Thesis, University of British Columbia, Vancouver, Canada, 1992.

[77] Sutliff, Thomas J., "An Acceleration Measurement Capability on International Space Station Supporting Microgravity Science Payloads," 35th Aerospace Sciences Meeting & Exhibit, AIAA Paper 97-0349 / NASA Technical Memorandum 107415, January 1997.

[78] Tinker, Michael L., "Modal Vibration Test Facilities and Methods for Space Station Modules", AIAA Structures, Structural Dynamics and Materials Conference, December 1995, p. 1190-1197.

[79] Thomson, W. T. and Y. C. Fung, "Instability of Spinning Space Stations Due to Crew Motion." AIAA Journal, Vol. 3, No. 6, June 1965.
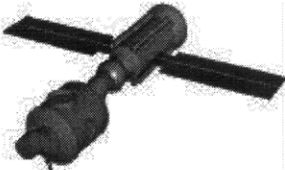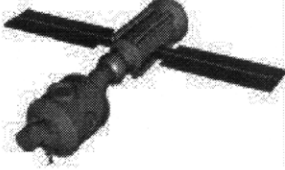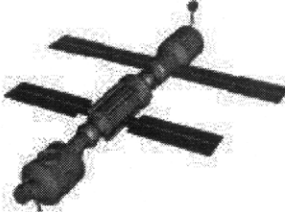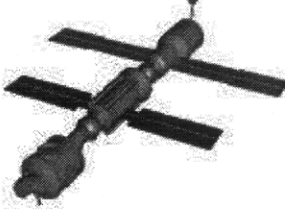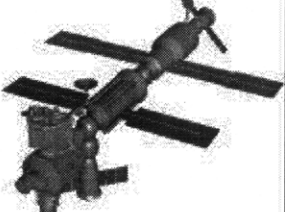
[80] Vanderplaats, G.N., *ADS—A Fortran Program for Automated Design Synthesis*, VMA Engineering, Goleta, California.

[81] Van der Vooren, A.I., "A Method to Determine the Change in Flutter Speed due to Changes in the Mechanical System", National Aeronautical Research Institute, Report V.1366, Amsterdam, 1947.

[82] van Schoor, Marthinus C. and Dava J. Newman, "Dynamic Load Sensor Experiment: Background, Science Objectives, Requirements, and Preliminary Design," November 18, 1992

[83] Yao, Leehter, William A. Sethares and Daniel C. Kammer, "Sensor Placement for On-Orbit Modal Identification via a Genetic Algorithm", American Institute of Aeronautics and Astronautics Journal, Vol. 31, No. 10, October 1993, pp. 1923-1930.

[84] Zhou, Kemin and John C. Doyle, *Essentials of Robust Control*, Prentice-Hall Inc., Upper Saddle River, NJ, 1998.
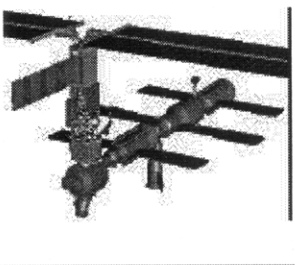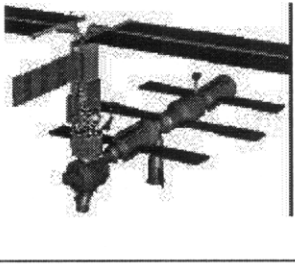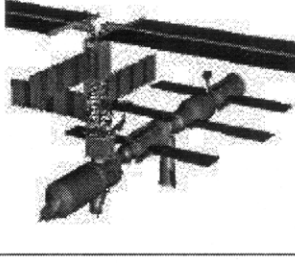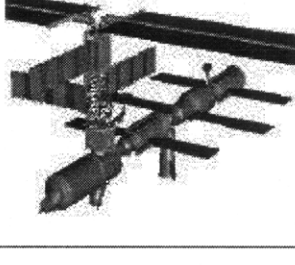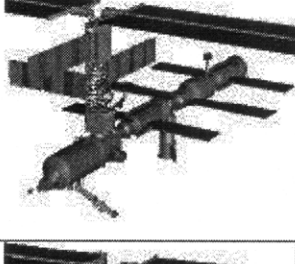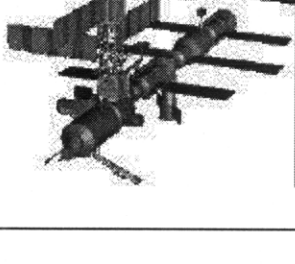
Appendix A
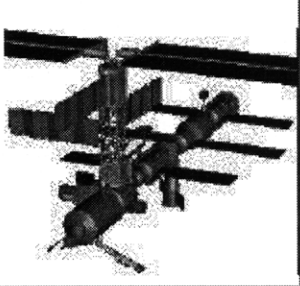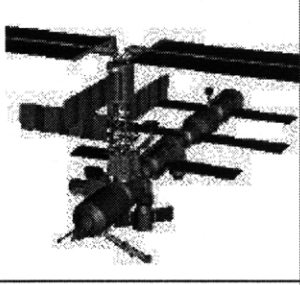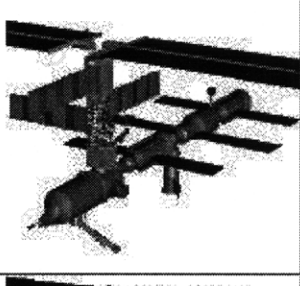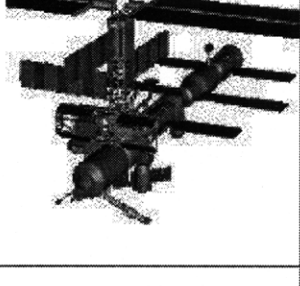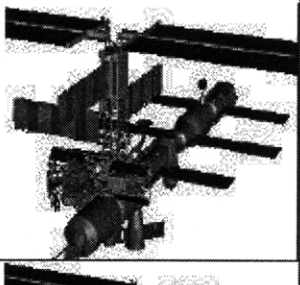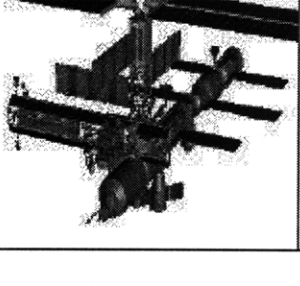
International Space Station Assembly Timetable
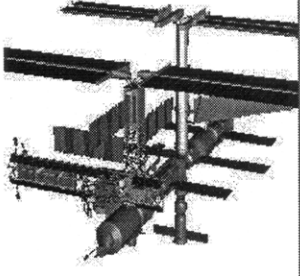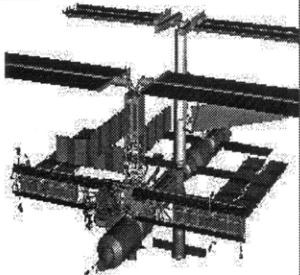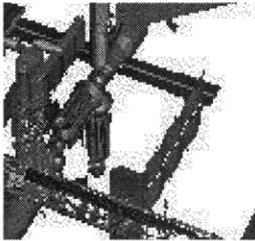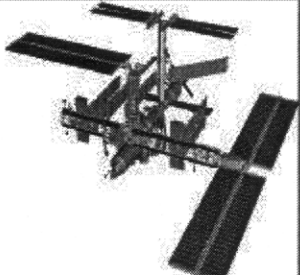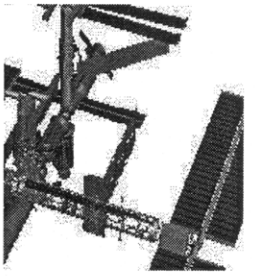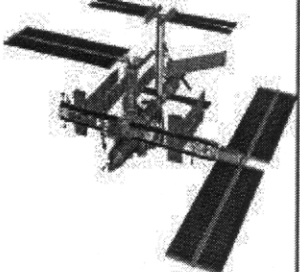
A.1 Assembly Schedule
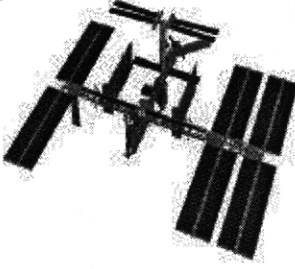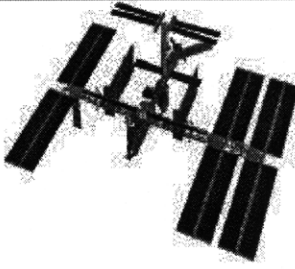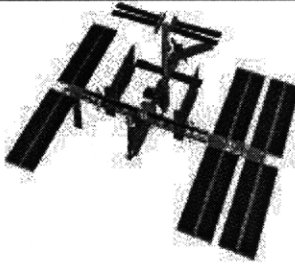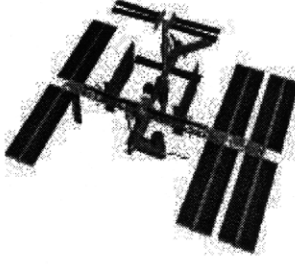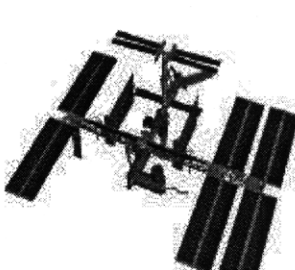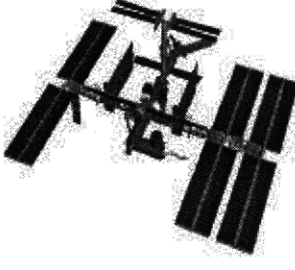
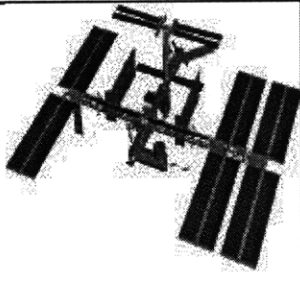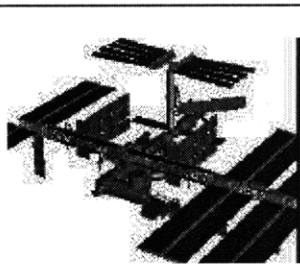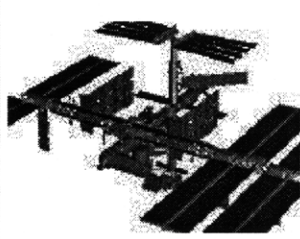| Date	Flight	Launch Vehicle	Configuration	Element(s)	Rationale
Nov 1998	1A/R	Russian Proton Rocket		• Zarya control module (Functional Cargo Block-FGB)	• The Control Module (FGB) is a self-supporting active vehicle. • It provides propulsive control capability and power through the early assembly stages. • It provides fuel storage capability. • It provides a rendezvous and docking capability to the Service Module.
Dec 1998	2A	US Space Shuttle (STS-88)		• Unity connecting module (Node 1) • 2 Pressurized Mating Adapters attached to Unity	• Unity is launched passive with 2 Pressurized Mating Adapters (PMAs) attached and 1 stowage rack installed inside. • PMA-1 will connect US and Russian elements. PMA-2 provides a Shuttle docking location. • Eventually, Unity's six ports will provide connecting points for the Z1 truss exterior framework; U.S. lab; airlock; cupola; Node 3; and the MPLM as well as the Control Module.
May 1999	2A.1	US Space Shuttle (STS-96)		• Spacehab Double Cargo Module	• Carries internal logistics and resupply cargo for station outfitting. • Carries external Russian cargo crane to be mounted to exterior of Russian station segment and used to perform spacewalking maintenance activities.
July 1999	1R	Russian Proton Rocket		• Service Module	• The Service Module is the primary Russian station contribution and an early station living quarters. It provides life support system functions to all early elements. • Primary docking port for Progress-type cargo resupply vehicles. • Provides propulsive attitude control and reboost capability for early station.
Aug 1999	2A.2	US Space Shuttle (STS-101)		• Spacehab Double Cargo Module	• Carries logistics and resupply cargo for station outfitting.
Oct 1999	3A	US Space Shuttle (STS-92)		• Integrated Truss Structure (ITS) Z1 • PMA-3 • Ku-band communications system • Control Moment Gyros (CMGs)	• ITS Z1 is an early exterior framework to allow first U.S. solar arrays on flight 4A to be temporarily installed on Unity for early power. • Ku-band communication system supports early science capability and U.S. television on 6A. • CMGs provide non-propulsive (electrically powered) attitude control when activated on 5A. • PMA-3 provides Shuttle docking port for solar array installation on 4A, Lab installation on 5A.
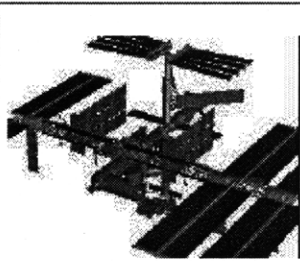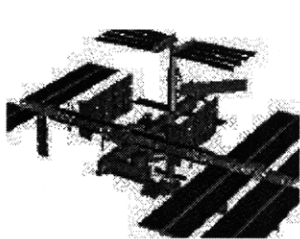
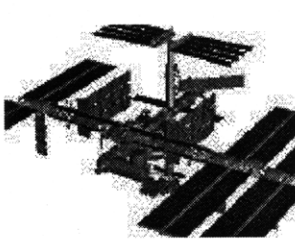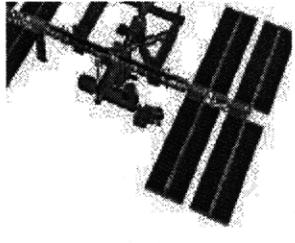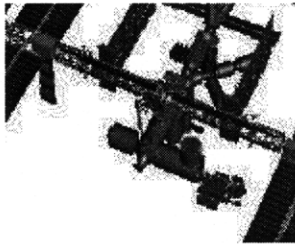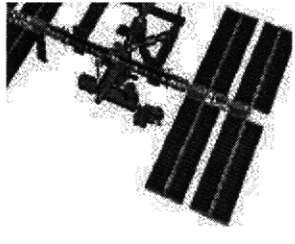| Date	Flight	Launch Vehicle	Configuration	Element(s)	Rationale
Dec 1999	4A	US Space Shuttle (STS-97)		• Integrated Truss Structure P6 • Photovoltaic Module • Radiators	• Provides first US solar power with solar arrays and batteries, called photovoltaic (PV) module. • First PV module installed temporarily on Z1 truss until after 13A when can be moved to P5 truss. • Two radiators provide early cooling, called photovoltaic (PV) Thermal Control System (TCS) radiators. Also, S-band communications system is activated for voice and telemetry.
Jan 2000	2R	Russian Soyuz Rocket		• Soyuz	• Establishes first station manning with three-person crew: Commnader Bill Shepherd; Soyuz Commander Yuri Gidzenko; Flight Engineer Sergei Krikalev. • Provides Russian assured crew return capability without the Space Shuttle present. • Station begins permanent human presence.
Feb 2000	5A	US Space Shuttle (STS-98)		• U.S. Laboratory Module	• Provides initial US user capability. • Launched with 5 system racks already installed inside of the module. • Control Moment Gyroscopes are activated with delivery of electronics in lab, providing electrically powered attitude control.
Mar 2000	5A.1	US Space Shuttle (STS-102)		• Logistics and Resupply; Lab Outfitting • Multi-Purpose Logistics Module (MPLM)carries equipment racks	• Provides logistics and resupply. • Carries equipment to assist in outfitting of the U.S. Laboratory module in Italian-built logistics module.
April 2000	6A	US Space Shuttle (STS-100)		• Leonardo MPLM (Lab outfitting) • Ultra High Frequency (UHF) antenna • Space Station Remote Manipulator	• Italian-built Leonardo Multi-Purpose Logistics Module (MPLM) carries 6 system racks and 2 storage racks to be installed in U.S. Lab. • UHF antenna provides space-to-space communications capability for US-based spacewalks. • Delivers Canadian SSRMS (station mechanical arm) needed to perform assembly operations on later flights.
July 2000	7A	US Space Shuttle (STS-104)		• Joint Airlock • High Pressure Gas Assembly	• Airlock provides station-based Extravehicular Activity (EVA) spacewalking capability for both US and Russian spacesuits. • High pressure gas assembly supports spacewalk operations and augments the Service Module gas resupply system.
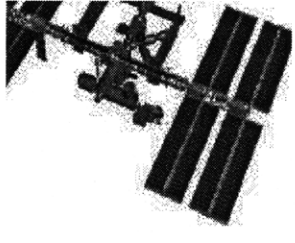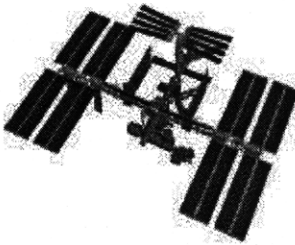
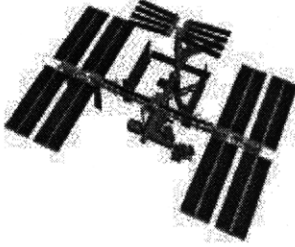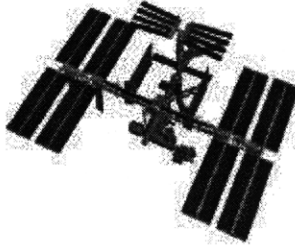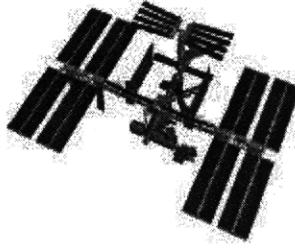| Date	Flight	Launch Vehicle	Configuration	Element(s)	Rationale
TBD *flight details still under review*	*7A.1*	*US Space Shuttle*		• *MPLM*	• *U.S. stowage racks and International Standard Payload Racks (ISPRs) carried in MPLM.*
TBD *flight details still under review*	*4R*	*Russian Soyuz Rocket*		• *Docking Compartment Module-1 (DCM-1)*	• *Provides additional egress, ingress location for Russian-based spacewalks and a Soyuz docking port.*
TBD *flight details still under review*	*UF-1*	*US Space Shuttle*		• *MPLM* • *PV Module batteries* • *Spares Pallet (spares warehouse)*	• *Provides for research work by delivering experiment racks for US Laboratory and two storage racks.* • *Spares Pallet provides an exterior "warehouse" for spare station parts. Attached to the exterior of the station airlock, it will house spare replacement equipment for station maintenance in a location convenient to spacewalking astronauts..*
TBD *flight details still under review*	*8A*	*US Space Shuttle*		• *Central truss segment (ITS S0)* • *Mobile Transporter (MT)*	• *Integrated Truss Structure S0 is center segment of the 300-foot station truss, attached to the U.S. Lab. By assembly complete, four more truss segments will attach to either side of the S0 truss.* • *Provided by Canada, the Mobile Transporter creates a movable base for the station's Canadian mechanical arm, allowing it to travel along the station truss after delivery of the Mobile Base System (MBS).*
TBD *flight details still under review*	*UF-2*	*US Space Shuttle*		• *MPLM with payload racks* • *Mobile Base System (MBS)*	• *The Multi-Purpose Logistics Module (MPLM) carries experiment racks and three stowage and resupply racks to the station.* • *The Mobile Base System is installed on the Mobile Transporter to complete the Canadian Mobile Servicing System (MSS). The mechanical arm will now have the capability to "inchworm" from the U.S. lab fixture to the MSS and travel along the truss to work sites.*
TBD *flight details still under review*	*9A*	*US Space Shuttle*		• *First starboard truss segment (ITS S1) with radiators* • *Crew and Equipment Translation Aid (CETA) Cart A*	• *Delivers first starboard truss segment (S1 truss) to be attached to central truss segment (S0 truss). Additional cooling radiators are delivered but will remain stowed until flight 12A.1.* • *Backup S-band communications capability is provided.* • *CETA cart can be used by spacewalkers to move along truss with equipment.*

Date	Flight	Launch Vehicle	Configuration	Element(s)	Rationale
TBD *flight detail sstill under review*	*9A.1*	*US Space Shuttle*		• *Russian-provided Science Power Platform (SPP) with four solar arrays*	• *Delivery of the Russian power and control mast with four solar arrays, called the Science Power Platform, will provide additional Russian electrical power.* • *Delivers European Robotic Arm (ERA), a second station mechanical arm that will be used to maintain the SPP.*
TBD *flight detail sstill under review*	*11A*	*US Space Shuttle*		• *First port truss segment (ITS P1)* • *Crew and Equipment Translation Aid (CETA) Cart B*	• *Delivers the first port truss segment (P1 truss) to be attached to central truss segment (S0 truss). Also includes additional cooling radiators that will remain stowed until flight 12A.1.* • *The Crew and Equipment Translation Aid Cart can be used by spacewalkers to move along the truss with equipment.*
TBD *flight detail sstill under review*	*3R*	*Russian Proton Rocket*		• *Universal Docking Module*	• *Provides docking locations for Russian Research Modules and a Docking Compartment (DC2) delivered on Flight 5R. The module also provides additional life support systems capabilities.*
TBD *flight detail sstill under review*	*12A*	*US Space Shuttle*		• *Second port truss segment (ITS P3/P4)* • *Solar array and batteries*	• *Delivers second port truss segment (P3/P4 truss) to attach to first port truss segment (P1 truss).* • *Central cooling radiators, delivered earlier on flights 9A and 11A, are deployed from first starboard (S1 truss) port (P1) truss segments.* • *Exterior attachments for Brazilian Unpressurized Logistics Carriers (ULCs) are delivered.*
TBD *flight detail sstill under review*	*5R*	*Russian Soyuz Rocket*		• *Docking Compartment 2 (DC2)*	• *Provides an improved Russian airlock.*
TBD *flight detail sstill under review*	*12A.1*	*US Space Shuttle*		• *Third port truss segment (ITS P5)* • *Multi-Purpose Logistics Module*	• *Delivers third port truss segment (P5 truss) to attach to second port truss segment (P3/P4 truss).*

Date	Flight	Launch Vehicle	Configuration	Element(s)	Rationale
TBD flight detail sstill under review	13A	US Space Shuttle		• Second starboard truss segment (ITS S3/S4) • Solar array set and batteries (Photovoltaic Module)	• The second starboard truss segment (S3/S4 truss) is attached along with a third set of solar arrays. • Four external attachment sites for truss-mounted exterior experiments and research are delivered.
TBD flight detail sstill under review	10A	US Space Shuttle		• Node 2	• The second of three station connecting modules, Node 2, attaches to end of U.S. Lab and provides attach locations for the Japanese laboratory, European laboratory, the Centrifuge Accomodation Module and later Multi-Purpose Logistics Modules • Primary docking location for the Shuttle will be a pressurized mating adapter attached to Node 2.
TBD flight detail sstill under review	1J/A	US Space Shuttle		• Japanese Experiment Module Experiment Logistics Module (JEM ELM PS) • Science Power Platform (SPP) solar arrays	• Japanese-developed pressurized logistics module is delivered carrying four systems racks, 1 stowage rack and 3 experiment racks to be used for Japanese laboratory (Japanese Experiment Module) to be delivered on flight 1J. • Two additional solar arrys for the Russian Science Power Platform (SPP) are delivered on the Brazilian Unpressurized Logistics Carrier (ULC) in the shuttle's payload bay.
TBD flight detail sstill under review	1J	US Space Shuttle		• Japanese Experiment Module (JEM) • Japanese Remote Manipulator System (JEM RMS)	• The primary Japanese contribution, the Japanese Experiment Module (JEM) laboratory, is delivered and begins use. • A Japanese robotic arm attached to the Japanese Experiment Module is delivered. The arm will be used to tend experiments on the laboratory's "back porch," an Exposed Facility (EF) to be delivered on flight 2 J/A.
TBD flight detail sstill under review	9R	Russian Proton Rocket		• Docking and Stowage Module (DSM)	• Mounted to the Control Module (FGB) nadir port. • Provides additional on-orbit stowage and Soyuz docking location.
TBD flight detail sstill under review	UF-3	US Space Shuttle		• Multi-Purpose Logistics Module (MPLM) • Express Pallet	• Provides for experiment delivery, resupply and changeout. • Multi-Purpose Logisitcs Module carries inside experiment equipment racks. • Express Pallet carries external experiment equipment.

Date	Flight	Launch Vehicle	Configuration	Element(s)	Rationale
TBD *flight detail sstill under review*	*UF-4*	*US Space Shuttle*		• *Express Pallet* • *Spacelab Pallet carrying "Canada Hand" (Special Purpose Dexterouos Manipulator)* • *Alpha Magnetic Spectrometer*	• *Canadian-developed "hand" for station mechanical arm provides more intricate robotic maintenance capability.* • *Provides for experiment resupply and cha* • *Express Pallet carries external experiment equipment.* • *Delivers Alpha Magnetic Spectrometer experiment to be attached to station truss site.*
TBD *flight detail sstill under review*	*2J/A*	*US Space Shuttle*		• *Japanese Experiment Module Exposed Facility (JEM EF)* • *Solar Array Batteries*	• *Delivers "back porch" (Exposed Facility) for Japanese laboratory (JEM) along with external experiments carried in a Japanese exterior logistics carrier.* • *Four additional battery sets are delivered to complete the complement of batteries for all U.S. solar array sets delivered thus far.*
TBD *flight detail sstill under review*	*14A*	*US Space Shuttle*		• *Cupola* • *Science Power Platform (SPP) Solar Arrays* • *Service Module Micrometeroid and Orbital Debris Shields (SMMOD)*	• *Cupola with eight windows provides station crew with direct viewing capability for some robotics operations, spacewalks and experiments.* • *Two additional Russian Science Power Platform (SPP) Solar Arrays complete the arrays on the SPP. SPP arrays and exterior debris shielding for Service Module (SMMOD) are carried on Brazilian-provided Unpressurized Logistics Carrier (ULC).*
TBD *flight detail sstill under review*	*8R*	*Russian Soyuz Rocket*		• *Research Module 1*	• *Delivers first of two Russian laboratories providing experiment and research facilities.*
TBD *flight detail sstill under review*	*UF-5*	*US Space Shuttle*		• *Multi-Purpose Logistics Module* • *Express Pallet*	• *Provides for experiment delivery, resupply and changeout.* • *Multi-Purpose Logisitcs Module carries inside experiment equipment racks.* • *Express Pallet carries external experiment equipment.*
TBD *flight detail sstill under review*	*20A*	*US Space Shuttle*		• *Node 3*	• *Delivers third node as conecting module for station (Node 3) to be attached underneath Unity node (Node 1).* • *Inside of Node 3 are 2 avionics racks and 2 life support system racks.* • *Node 3 provides attachment points for the U.S. Habitation Module, U.S. Crew Return Vehicle, pressurized mating adapter, and any future station additions.*

Date	Flight	Launch Vehicle	Configuration	Element(s)	Rationale
TBD *flight detail sstill under review*	*10R*	*Russian Soyuz Rocket*		• *Research Module 2*	• *Delivers a second Russian laboratory to house experiments and research facilities.*
TBD *flight detail sstill under review*	*17A*	*US Space Shuttle*		• *Multi-Purpose Logistics Module* • *Node 3, U.S. Lab racks*	• *Delivers racks for Node 3 that allow expansion of station crew from three members to up to six members.* • *Outfits Node 3 with racks carried in MPLM: 2 life support system racks; 2 flight crew equipment racks (waste collection system and galley) and 3 Crew Health Care System racks.* • *For U.S. Lab, delivers 1 systems rack, 1 stowage rack and experiment racks.*
TBD *flight detail sstill under review*	*1E*	*US Space Shuttle*		• *European Laboratory-Columbus Orbital Facility*	• *Delivers the European Space Agency's primary contribution to the station, the Columbus Orbital Facility laboratory, provides additional research capability.*
TBD *flight detail sstill under review*	*18A*	*US Space Shuttle*		• *U.S. Crew Return Vehicle (CRV)*	• *Crew Return Vehicle attached to the station provides additional 7-person crew return capability added to already existing 3-person Soyuz crew return capability*
TBD *flight detail sstill under review*	*19A*	*US Space Shuttle*		• *Multi-Purpose Logistics Module*	• *Delivers 4 crew quarters racks to be placed in Node 2 and provide for transition to 6-person crew* • *Delivers 6 U.S. stowage racks* • *Delivers third starboard truss segment (S5 truss)*
TBD *flight detail sstill under review*	*15A*	*US Space Shuttle*		• *Solar Arrays and Batteries (Photovoltaic Module S6)*	• *Fourth and final set of U.S. solar arrays delivered along with fourth starboard truss segment (S6).*

Date	Flight	Launch Vehicle	Configuration	Element(s)	Rationale
TBD *flight detail sstill under review*	*UF-6*	*US Space Shuttle*		• *Multi-Purpose Logistics Module* • *Batteries*	• *Provides for experiment delivery, resupply and changeout.* • *Delivers two solar array batteries to complete station battery outfitting.*
TBD *flight detail sstill under review*	*UF7*	*US Space Shuttle*		• *Centrifuge Accomodations Module (CAM)*	• *The Centrifuge Accommodations Module (CAM) completes the complement of station laboratory facilities providing a facility to control gravity for research activities. The CAM attaches to Node 2.*
TBD *flight detail sstill under review*	*16A*	*US Space Shuttle*		• *U.S. Habitation Module*	• *Delivers U.S. Habitation Module to enhance crew accomodations and provide for a station crew with as many as seven members.*

NOTES:

- **Additional Progress, Soyuz, possible H-II Transfer Vehicle and Automated Transfer Vehicle flights for crew transport, logistics and resupply are not listed.**

Appendix B

Summary of Data From EDLS Space Flight Experiment

B.1 Raw Data from NASA-4 Mission

Table B.1: Summary of NASA-4 Raw Data File Size

PCMCIA Card	Number of Data Files	Size of Data Files (MBytes)
1	12	246.773
2	1	246.799
3	2	246.748
4	3	246.784
5	3	79.431
6	1	246.770
7	15	246.770
8	2	246.770
9	2	246.770
10	1	246.770
Totals	42	2,300.344

B.2 Extracted Data from NASA-4 Mission

Table B.2: Summary of NASA-4 Analyzed Data File Size

PCMCIA Card	Number of Data Files	Total Duration (h)
1	28	0.830

Table B.2: Summary of NASA-4 Analyzed Data File Size

PCMCIA Card	Number of Data Files	Total Duration (h)
2	50	1.428
3	50	0.013
4	37	0.540
5	37	0.965
6	43	1.145
7	64	1.747
8	49	1.298
9	61	1.582
10	58	1.631
Totals	477	11.180

Appendix C

Power Spectral Density Calculations And Shaping Filters

C.1 Power Spectral Density Function

For stationary processes, the power spectral density of a signal is defined through the Wiener-Khinchine relation:

$$S_X(j\omega) = \mathcal{F}[R_X(\tau)] = \int_{-\infty}^{\infty} R_X(\tau)e^{-j\omega\tau}d\tau \qquad (C.1)$$

where $\mathcal{F}$ indicates the Fourier transform and ω is the angular frequency. S_X is called the power spectral density function or simply the spectral density function of the process. The adjectives *power* and *spectral* come from the relationship of S_X to the usual spectrum concept for a deterministic signal. However, some care is required in making this connection. If the process $X(t)$ is time stationary, it wanders on ad infinitum and is not absolutely integrable. Thus, the defining integral for the Fourier transform does not converge. When considering the Fourier transform of the signal, we are forced to consider a truncated version of it, say, $X_T(t)$, which is truncated to zero outside a span of time T. The Fourier transform of a sample realization of the truncated process will then exist.

Let $\mathcal{F}\{X_T(t)\}$ denote the Fourier transform of $X_T(t)$, where it is understood that for any given ensemble of samples of $X_T(t)$ there will be a corresponding ensemble of $\mathcal{F}\{X_T(t)\}$. That is, $\mathcal{F}\{X_T(t)\}$ has stochastic attributes just as does $X_T(t)$. If the following expectation is considered:

$$E\left[\frac{1}{T}|\mathcal{F}\{X_T(t)\}|^2\right] \qquad (C.2)$$

144

For any particular sample realization of $X_T(t)$, the quantity inside the brackets is known as the *periodogram* for that particular signal. It can easily be shown that averaging over an ensemble of periodograms for large T yields the power spectral density function. Thus, the power spectral density function for a given sample signal can be estimated directly from the periodogram of the signal. From equation C.2 it can be seen that the average periodogram[1] is proportional to the spectral density function[2]. Unfortunately, since we do not usually have the luxury of having a large ensemble of periodograms to average, there are pitfalls in this approach, just as there are in attempting to Fourier transform the experimentally determined autocorrelation function. Nonetheless, modern digital processing methods using fast Fourier transform (FFT) techniques have popularized the periodogram approach. This is the approach used in this thesis in order to calculate the 95% power spectral density figures for the results in chapter 4. Thus, it is important to discuss the limitations of this technique.

C.2 Limitations of the Fast Fourier Transform Technique

First and foremost, when attempting to estimate the power spectral density of a signal, there is the problem of truncation. When the time record being analyzed is finite in length, we usually assume that the signal will "jump" abruptly to zero outside the valid data interval. This causes frequency spreading and gives rise to high-frequency components that are not truly representative of the process under consideration, which is assumed to "ramble" on indefinitely in a continuous manner. An extreme case of this would occur if we were to chop up one long record into many very short records and then average the periodograms of the short records. The individual periodograms, with their predominance of high-frequency components due to the truncation would not be at all representative of the spectral

---

1. The square of the magnitude of the Fourier transform of $X_T(t)$
2. This is true only for large T.

content of the original signal; nor would their average. Thus, the first rule is that we must have a long time record relative to the typical time variations in the signal. This is true regardless of the method used in analyzing the data. There is, however, a statistical convergence problem that arises as the record length becomes large.

From Equation C.2 it can be seen that the expectation of the periodogram approaches the spectral density of the process for large T. This is certainly desirable, because we want the periodogram to be an unbiased estimate of the spectral density. It is also of interest to look at the behavior of the variance of the periodogram as T becomes large. Let us denote the periodogram of $X_T(\tau)$ as $M(\omega, T)$, that is:

$$M(\omega, T) = \frac{1}{T} |\mathcal{F}\{X_T(t)\}|^2 \tag{C.3}$$

Not that the periodogram is a function of the record length T as well as ω. The variance of $M(\omega, T)$ is:

$$\sigma_M^2 = E[M^2] - (E[M])^2 \tag{C.4}$$

where from the definition of the expectation we have:

$$E[M] = \int_{-\infty}^{\infty} R_X(\tau) e^{-j\omega\tau} d\tau \tag{C.5}$$

$$E[M^2] = 2(E[M])^2 + \frac{1}{T^2} \left| \int_0^T \int_0^T R_X(t-u) e^{-j\omega(t+u)} dt du \right|^2 \tag{C.6}$$

therefore we get:

$$\sigma_M^2 = (E[M])^2 + \frac{1}{T^2} \left| \int_0^T \int_0^T R_X(t-u) e^{-j\omega(t+u)} dt du \right|^2 \tag{C.7}$$

The second term of C.7 is non-negative, so it should be clear that

$$\sigma_M^2 \geq (E[M])^2 \tag{C.8}$$

But we know that $E[M]$ approaches the spectral function as $T \to \infty$. Thus the variance of the periodogram does not go to zero as $T \to \infty$. In other words, the periodogram does not

converge in the mean as $T \to \infty$ [3]. This is most disturbing, especially in view of the popularity of the periodogram method of spectral determination. Thus, increasing T will not help reduce the ripples in the individual periodogram. It simply makes M "jump" around faster with ω. This does help, though, with the subsequent averaging that must accompany the spectral analysis. Recall that it is the *average* periodogram that is the measure of the spectral density function. Averaging in both frequency and time is easily accomplished in analog spectrum analyzers by appropriate adjustment of the width of the scanning window and the sweep speed. In digital analyzers, similar averaging over a band of discrete frequencies can be implemented in software. Also, further averaging in time may be accomplished by averaging successive periodograms, before displaying the spectrum graphically. In either event, analog or digital, some form of averaging is essential when analyzing a noisy signal.

C.3 Implementation of the Fast Fourier Transform

Modern computer technology has made it possible to perform an efficient discrete version of the Fourier transform. Thus, nearly all spectral analysis is now done using the direct periodogram approach. Shannon's sampling theorem dictates the constraints on the choice of sampling rate[4] and the total amount of data analyzed in any one batch.

The discrete Fourier transform (DFT) is defined as:

$$G_n = \frac{1}{N} \sum_{k=0}^{N-1} g_k e^{-j\left(\frac{2\pi nk}{N}\right)} \qquad n = 0, 1, 2, ...N-1 \qquad (C.9)$$

where $g_0, g_1, g_2, ...g_{N-1}$ is the sequence of N discrete time samples of the continuous signal $g(t)$.

---

3. Except possibly at those exceptional points where the spectral function is zero.
4. The optimal rate is the Nyquist Rate 2W Hz, where W is the bandwidth of the signal.

Digital implementation of the discrete Fourier transform is not a trivial matter. High resolution and reliable results in the frequency domain are obtained by making N large. However, if one programs the transform literally as given by C.9, the number of multiplications required is of the order N^2. This can easily get out of hand, especially in "on-line" applications. Fortunately, fast efficient algorithms have been developed for which the number of required multiplications is of the order $N\log_2 N$ instead of N^2. This computational saving is spectacular for large N.

All of the fast discrete Fourier transform algorithms require that the number of samples be an integer power 2, and they all go under the generic name of fast Fourier transform. The fast Fourier transform is simply a computationally efficient means of implementing the discrete Fourier transform. Due to its efficiency, the fast Fourier transform is used almost universally in on-line spectral analysis. However, in off-line applications where speed is of little concern, the straightforward programming of the DFT, as given in C.9 is advantageous. For example, if only a limited amount of data is available and it is desirable to achieve as fine a resolution as possible in the frequency domain, the straightforward DFT is preferred because N is not restricted to integer powers of two, as it is with the FFT. As well, the DFT is easily generalized to the case where the time-domain samples are complex.